Strong-field and time-resolved photoemission from plasmonic nanoparticles

by

Erfan Saydanzad

B.S., University of Kurdistan, Iran, 2006

M.S., Graduate University of Advanced Technology, Iran, 2009

AN ABSTRACT OF A DISSERTATION

submitted in partial fulfillment of the
requirements for the degree

DOCTOR OF PHILOSOPHY

Department of Physics
College of Arts and Sciences

KANSAS STATE UNIVERSITY
Manhattan, Kansas

2022

Abstract

In this dissertation, numerical models have been developed to investigate strong-field photoemission and attosecond streaking spectroscopy from plasmonic nanoparticles. Attosecond streaking spectroscopy and strong-field photoemission are powerful methods for investigating the electronic dynamics in gaseous atoms, that are currently being transferred to the investigation of collective electronic (plasmonic) effects in solids and nanostructures.

First, a classical model is proposed to study plasmon excitations in metal nanoparticles using attosecond streaking spectroscopy. In this model, by sampling over classical photoelectron trajectories, we simulated streaked photoelectron energy spectra as a function of the time delay between ionizing isolated attosecond extreme ultraviolet pulses and assisting infrared or visible streaking laser pulses. Our theoretical model comprises a sequence of four steps: XUV excitation, electron transport in the nanoparticles, escape from the surface of the nanoparticles, and propagation to the photoelectron detector. Based on numerical applications to gold nanospheres, we investigated streaked photoemission spectra with regard to (i) the nanoparticle's dielectric response to the electric field of the streaking laser pulse, (ii) relative contributions of photoelectron release from different locations on and in the nanoparticle, (iii) contributions of photoemission from the Fermi level only versus emission from the entire occupied conduction band, and (iv) their fidelity in imaging the spatiotemporal distribution of the induced plasmonic field near the particle's surface.

Second, based on this model, we suggest a method for reconstructing induced plasmonic fields with nm spatial and sub-fs temporal resolution from streaked photoemission spectra. Applying this imaging scheme to gold nanospheres, we demonstrated the accurate spatiotemporal reconstruction of the plasmonic near-field distribution in comparison with the directly calculated plasmonic field.

Finally, strong-field photoemission from metal nanoparticles was modeled. The numerical model includes: (i) photoelectron emission on the nanoparticle surface by an intense infrared laser pulse, (ii) photoelectron propagation outside the nanosphere in the presence of the incident laser and induced plasmonic fields, and (iii) photoelectron rescattering and recombination to the nanoparticle. Based on simulated photoelectron-momentum distributions from gold nanospheres for two different intensities, and in comparison with velocity-map-image photoelectron spectra measured at the James R. Macdonald Laboratory, we scrutinize the effects of induced plasmonic fields, photoelectron correlations and electron-residual charge interactions, and photoelectron rescattering and recombination at the nanoparticle surface.

Strong-field and time-resolved photoemission from plasmonic nanoparticles

by

Erfan Saydanzad

B.S., University of Kurdistan, Iran, 2006

M.S., Graduate University of Advanced Technology, Iran, 2009

A DISSERTATION

submitted in partial fulfillment of the
requirements for the degree

DOCTOR OF PHILOSOPHY

Department of Physics
College of Arts and Sciences

KANSAS STATE UNIVERSITY
Manhattan, Kansas

2022

Approved by:

Major Professor
Uwe Thumm

Copyright

Abstract

In this dissertation, numerical models have been developed to investigate strong-field photoemission and attosecond streaking spectroscopy from plasmonic nanoparticles. Attosecond streaking spectroscopy and strong-field photoemission are powerful methods for investigating the electronic dynamics in gaseous atoms, that are currently being transferred to the investigation of collective electronic (plasmonic) effects in solids and nanostructures.

First, a classical model is proposed to study plasmon excitations in metal nanoparticles using attosecond streaking spectroscopy. In this model, by sampling over classical photoelectron trajectories, we simulated streaked photoelectron energy spectra as a function of the time delay between ionizing isolated attosecond extreme ultraviolet pulses and assisting infrared or visible streaking laser pulses. Our theoretical model comprises a sequence of four steps: XUV excitation, electron transport in the nanoparticles, escape from the surface of the nanoparticles, and propagation to the photoelectron detector. Based on numerical applications to gold nanospheres, we investigated streaked photoemission spectra with regard to (i) the nanoparticle's dielectric response to the electric field of the streaking laser pulse, (ii) relative contributions of photoelectron release from different locations on and in the nanoparticle, (iii) contributions of photoemission from the Fermi level only versus emission from the entire occupied conduction band, and (iv) their fidelity in imaging the spatiotemporal distribution of the induced plasmonic field near the particle's surface.

Second, based on this model, we suggest a method for reconstructing induced plasmonic fields with nm spatial and sub-fs temporal resolution from streaked photoemission spectra. Applying this imaging scheme to gold nanospheres, we demonstrated the accurate spatiotemporal reconstruction of the plasmonic near-field distribution in comparison with the directly calculated plasmonic field.

Finally, strong-field photoemission from metal nanoparticles was modeled. The numerical model includes: (i) photoelectron emission on the nanoparticle surface by an intense infrared laser pulse, (ii) photoelectron propagation outside the nanosphere in the presence of the incident laser and induced plasmonic fields, and (iii) photoelectron rescattering and recombination to the nanoparticle. Based on simulated photoelectron-momentum distributions from gold nanospheres for two different intensities, and in comparison with velocity-map-image photoelectron spectra measured at the James R. Macdonald Laboratory, we scrutinize the effects of induced plasmonic fields, photoelectron correlations and electron-residual charge interactions, and photoelectron rescattering and recombination at the nanoparticle surface.

Table of Contents

List of Figures

Acronyms

ADK	Ammosov-Delone-Krainov
CB	Conduction-band
COE	Center of energy
e-e	electron-electron
fs	Femtosecond
FWHIM	Full temporal width at half intensity maximum
IR	Infrared
LSP	Localized surface-charge plasmon
M^3C	Mean-field Monte-Carlo
NIR	Near infrared
NP	Nanoparticle
PDF	Probability density function
PE	Photoelectron
PEMD	Photoelectron momentum distribution
VMI	Velocity-map-imaging
XUV	Extreme ultraviolet

Acknowledgments

Pursuing a Ph.D. degree would not have been possible without the help and support of so many amazing people who have surrounded me. To them, I would like to express my sincere gratitude.

Firstly, my advisor Prof. Uwe Thumm for the continuous support of my Ph.D. study and related research, for his patience, motivation, and immense knowledge. His guidance helped me in all the time of research and writing of this thesis. I could not have imagined having a better advisor and mentor for my Ph.D. study.

To the committee members, Dr. Artem Rudenko, Dr. Christopher Sorensen, Dr. Christine Aikens, graduate program director Dr. Michael J. O'Shea, and the outside chairperson, Dr. Walter McNeil for their insightful discussion with my research, and their time and effort in reviewing my dissertation.

To my colleagues in Dr. Uwe Thumm's group, including Dr. Jianxiong Li, whom I had the pleasure to most closely work with, Hongyu Shi, Dr. Aihua Liu, Dr. Marcelo Ambrosio, Dr. Francisco Navarrete, Dr. Hung Hoang, Dr. Paul Abanador, and Alex Kramer. They are not only colleagues that helped me with my research, but also friends in life.

To Dr. Jeffrey Powell, a previous member of Dr. Rudenko's group, whom I had the pleasure to closely work with, in the experiment-theory collaboration, for the amazing experimental work and insightful discussion.

To my dear friend Reza Mazloom for his help and useful advice in the computational part of my research and my friend Aram Vajdi for his stimulating discussion with my research.

To Dr. Kevin Carnes for his time and effort to proofread and review my dissertation.

To the professors in Physics Department, whom I am most fortunate to learn from in their courses and discussions, especially Dr. Brett Esry, Dr. Brian Washburn, Dr. Jeremy Schmit, Dr. Chii-Dong Lin, Dr. Bharat Ratra, Dr. Gary Wysin, Dr. Glenn Horton-Smith, Dr. Matthew J. Berg, and Dr. Brett DePaola.

To the professors and staff whom I worked with as Teaching Assistant during the past years, Dr. Tim Bolton, Dr. Bret Flanders, Dr. Vinod Kumarappan, Dr. Bruce Law, Austin Roberts, and Peter Nelson.

To the support staff in Physics Department, both previous and present, especially Larry McFeeters and Vince Needham for maintaining the computing resources for our research needs, and Kim Coy, Kim Elliott, Kelsey Young, and Peggy Matthews for the help with office work. To all my colleagues and friends in Physics Department, for helping me with my research and course work, and being friends in life.

To my dear father Mohammad Jamil and mother Farasat, for loving, supporting, and raising me. To my dear brothers Arman and Mohammad, sister Helen, and aunt Kolsoom for their love and support.

Dedication

This dissertation is dedicated to my dear father Mohammad Jamil, who is no longer of this world, my beloved mother Farasat, sister Helen, and brothers Arman and Mohammad.

Chapter 1

Introduction

Exposed to intense laser light, atoms, molecules, solid surfaces, or nanostructures are excited or ionized. When the intensity of the incident laser pulse is not high enough to ionize the target, we can see a variety of excitations such as electron transitions to higher energy levels or collective electronic excitation such as the plasmon excitation in metal. When the intensity of the incident laser pulse is sufficiently high, multi-photon or tunnel ionization can occur. In this dissertation, we are investigating plasmon excitations in metal nanoparticles (NPs) using attosecond streaked photoelectron (PE) spectroscopy and strong-field photoemission of metal NPs using velocity-map-imaging (VMI).

1.1 Plasmon excitation

Metal NPs have been extensively investigated during the past two decades, owing to their remarkable optical properties [1, 2]. These are largely related to incident light in the infrared (IR) to the visible frequency range enforcing the collective motion of conduction electrons. This light-driven excitation of localized surface-charge plasmons (LSP), controls the NPs light absorption, reflection, and skin depths [3]. It also can exhibit nm-scale variations and exceed the incident-field intensity near nanostructured surfaces [4–9] and isolated NPs [10, 11] by orders of magnitude [12] at incident field frequencies near the NPs plasmon resonance [12,

13]. The LSP resonance frequency can be tuned from IR to visible frequencies by synthesizing metal NPs with specific shapes, sizes, compositions, and dielectric environments [2, 14, 15]. The tunable enhanced light absorption and scattering are key to powerful diagnostic methods, such as:

- Surface-enhanced Raman spectroscopy [16]
- Femtosecond scanning tunneling microscopy and spectroscopy [17]
- Time-resolved nanoplasmonic-field microscopy [4, 11, 13, 18]
- Biomedical and chemical sensing [19, 20]
- Bio-imaging, where plasmonic NPs are used as markers [21].

In addition, the controllable electro-optical properties of metal NPs are enabling promising applications, including:

- The *in vivo* optoporation of targeted retinal ganglion cells with functionalized Au NPs [22]
- Multichromatic switchable nano-pixels [23]
- Nanoplasmonically enhanced photocatalysis [24]
- Plasmon-enhanced light harvesting [25, 26]
- Tumor detection and treatment [27, 28]
- Ultrafast electro-optical switching [29]
- Thermo-plasmonics [30].

Progress in these promising applications will be facilitated by the accurate nm-sub-fs scale spatiotemporal characterization of transient nanoplasmonic fields, calling for the design of novel schemes for the reconstruction of plasmonic field distributions. We recently proposed classical [31] and quantum-mechanical [32] schemes for the spatiotemporal imaging of induced plasmonic-field distributions near the surface of Au, Ag, and Cu NPs, based on nm spatially resolved attosecond PE streaking spectroscopy [31].

1.2 Attosecond streaking spectroscopy

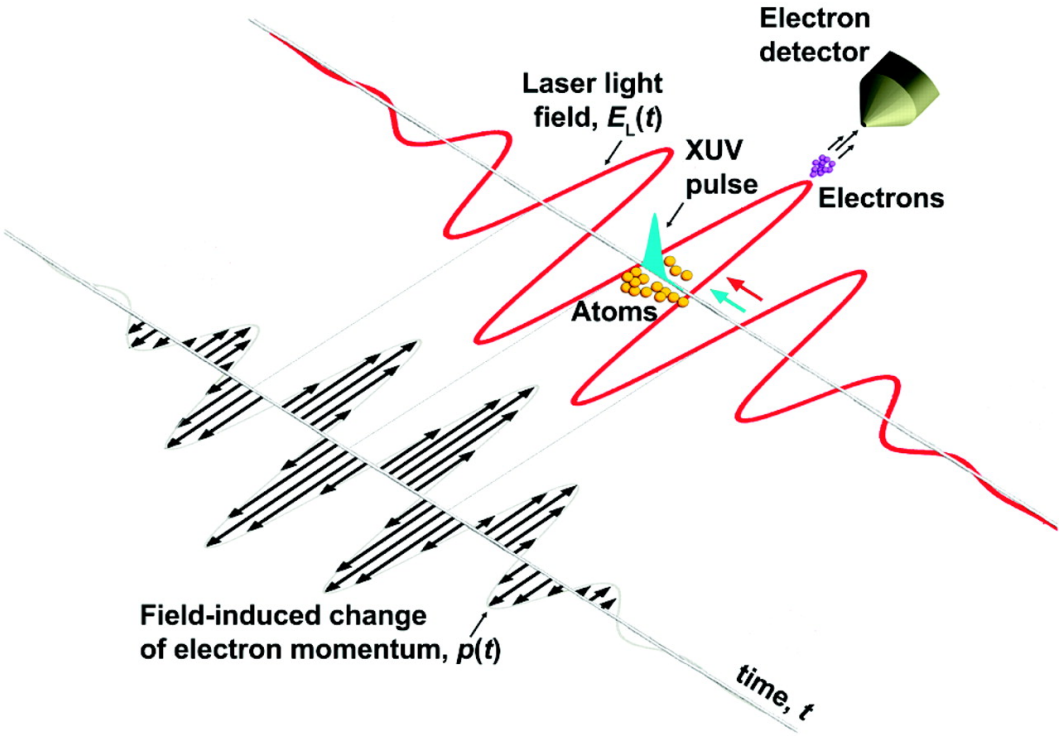

Figure 1.1: *Schematic of the attosecond streaking from atomic gas target. A few-cycle pulse of laser light, together with a synchronized sub-fs XUV burst, is focused into an atomic gas target. The XUV pulse releases electrons by photoionization. The light electric field $E_L(t)$ imparts a momentum change to the electrons (black arrows), which scales as the instantaneous value of the vector potential $A_L(t)$ at the instant of release of the probing electrons. The momentum change is measured by an electron detector, which collects the electrons ejected along the direction of the linearly polarized laser pulse (Figure from [33]).*

Starting with the new millennium, attosecond science has made rapid progress in developing pump-probe techniques for investigating the dynamics of electronic processes at the natural timescale of the electronic motion in matter, 1 as (1 attosecond = 10^{-18} seconds) [34]. Attosecond streaked photoemission spectroscopy, in particular, by illuminating a target with isolated attosecond extreme ultraviolet (XUV) pulses that are phase-coherently synchronized to a delayed strong IR (or visible) pulse, records photoemission yields as a function of the delay τ between the ionizing XUV and assisting streaking pulses, revealing temporal information through relative phase shifts of delay-dependent PE yields (so-called "streaking traces") from different initial electronic states of the target [35, 36]. After almost

two decades of proof-of-principle applications to relatively simple systems, such as atoms in the gas phase [33], this field of research is now further expanding to include time-resolved investigations of electronic excitation, electron transport, and collective electronic processes in solid matter [29, 36, 37]. In particular, the combination of attosecond ultrashort-pulse-laser technology with recent advances in nano-science and nano-technologies holds promise for the improved and detailed characterization, design, and fabrication of novel nanometer-scale structures that respond to irradiation with intense electromagnetic radiation in a controllable way, promoting, for example, new applications of ultrafast electro-optical information processing [29, 38]. In streaked PE spectra of NPs [11, 13, 18, 39] and nanotips [40, 41], the nanoplasmonic response to the streaking pulse leads to a characteristic amplitude increase and phase shift of the streaking traces, providing temporal information on the induced plasmon dynamics Fig. 1.2.

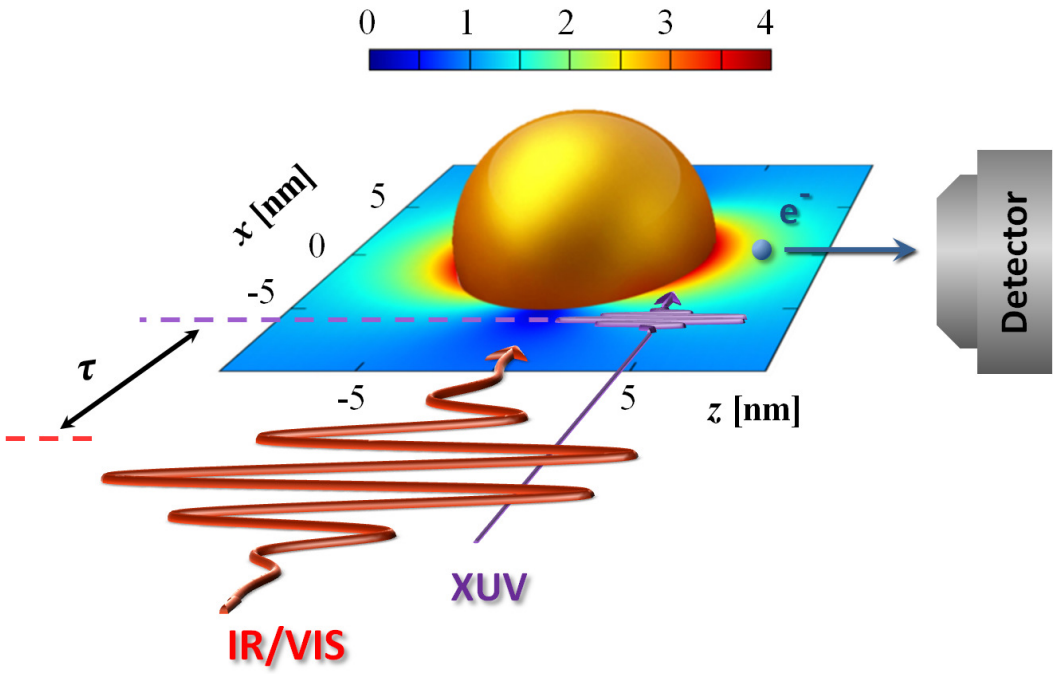

Figure 1.2: *Schematic of attosecond streaking from NPs. A single attosecond XUV pulse emits electrons into the field of a delayed IR streaking laser pulse. The linear color scale represents the local electric-field-strength enhancement in the $x-z$ plane. The size of the target and wavelength of laser pulses are not to scale*

1.3 Spatiotemporal imaging of plasmonic fields

The desire to understand, image, and ultimately control plasmonic excitation in solids motivates the continued improvement of imaging techniques towards the spatio-temporal resolution of plasmonic field distributions [4, 36]. A very promising way to realize the detailed mapping of induced plasmonic fields with atomic resolution in time and space is PE streaking spectroscopy [36]. Applied to solid targets, such high-resolution photoemission studies on extended targets address effects that are absent in isolated atoms in the gas phase. These additional phenomena include the propagation of photo-released electrons in the solid from their release point to the surface, subject to elastic and inelastic scattering [42, 43], the emitted PE's interaction with equilibrating residual surface-charge distributions [44], its interaction with the spatially inhomogeneous plasmonic field [10, 11, 36, 39, 45–47], and the finite skin depth [43] of the incident pulses of electromagnetic radiation. Motivated to study the control of plasmonic excitations, we have developed a quantum-mechanical model to image the plasmonic field with nm-spatial and sub-fs temporal resolution from metal NPs and nanoshells Fig. 1.3 that is optimized for ultrashort IR streaking pulses [32].

1.4 Strong-field ionization of atoms

At sufficiently high light intensities, multi-photon or tunnel ionization occurs [48, 49], and emitted PEs can gain a significant amount of energy while propagating in the oscillating laser electric field. For gaseous atomic targets, PEs that are directly emitted and do not return to the residual atom gain up to $2\,U_p(I_0)$ in kinetic energy in linearly polarized laser pulses, while PEs that are driven back to the residual ion by the laser electric field and rescatter elastically, accumulate up to $10\,U_p(I_0)$ [50–53]. The ponderomotive energy $U_p(I_0) = I_0/(4\omega^2)$ is the cycle-averaged quiver energy of a free electron in a laser field of frequency ω and intensity I_0.

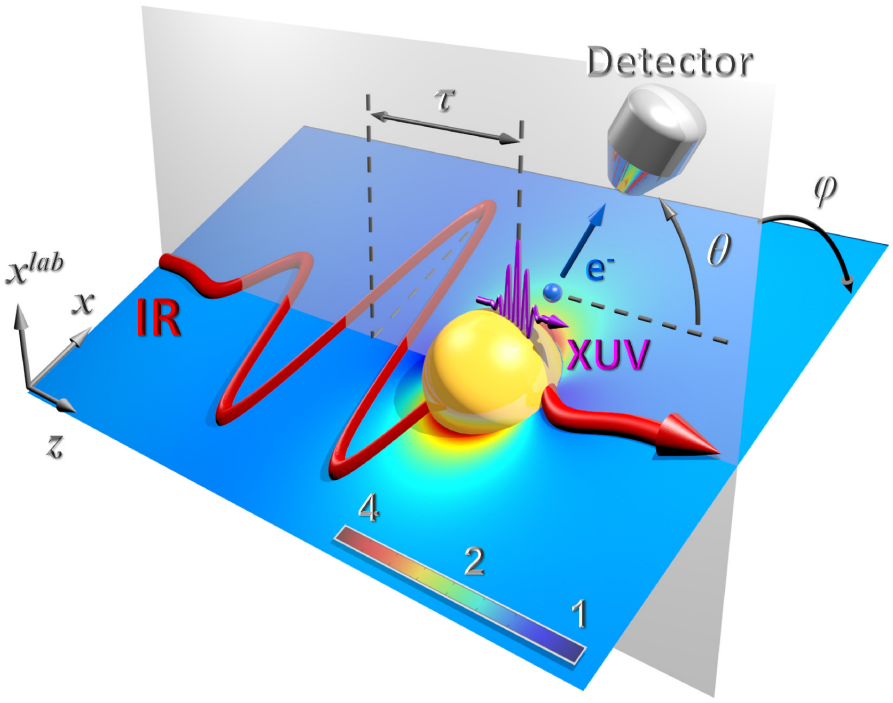

Figure 1.3: *Schematic of spatially-resolved attosecond nanoplasmonic imaging. An attosecond XUV pulse emits electrons into the field of a delayed IR streaking laser pulse, whose polarization direction can be rotated by a variable angle φ relative to the XUV-pulse polarization. The linear color scale represents the electric-field-strength enhancement for 50 nm radius Au nanospheres in 720 nm incident IR pulses. The size of the target and wavelength of laser pulses are not to scale.*

1.5 Strong-field ionization from dielectric nanoparticles

Strong-field PE emission and rescattering from solids [54–60] and isolated nanostructures, such as clusters [61–65], nanotips [17, 66, 67], and isolated dielectric NPs [10, 39, 68], was extensively studied throughout the past decade. Analogous to gaseous atoms, strong-field ionization leading to high PE energies from NPs can be thought of as occurring in distinct sequential steps [69]: electron emission from the NP surface, PE propagation in the continuum, and PE rescattering towards and interaction with the NP [65, 68]. In comparison with gaseous atomic targets, each of these steps is significantly more intricate for NPs, due to their more complex electronic and morphological structure and the emission of a larger number of PEs, emphasizing the effects of e-e interactions, residual charges, and PE

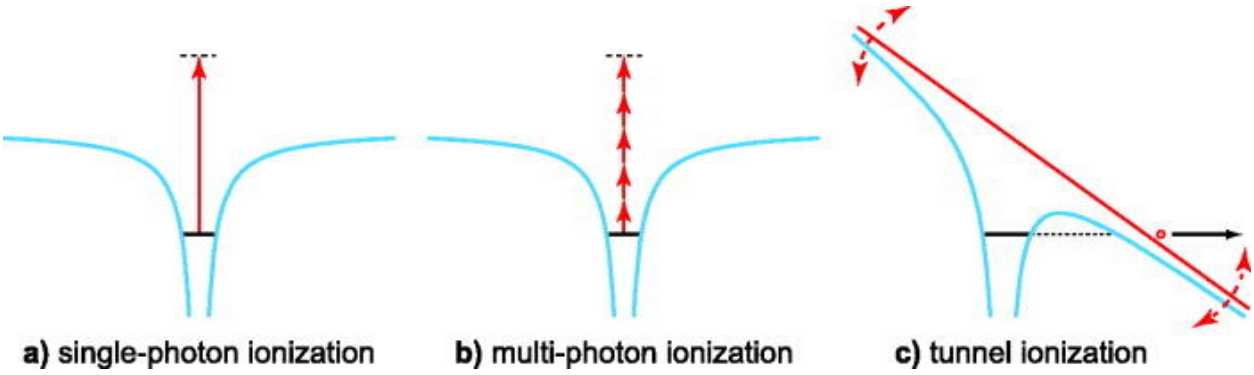

Figure 1.4: *Basic ionization processes in atoms. (a) In single-photon ionization, the atom is ionized through the absorption of a single energetic photon. (b) If the laser intensity is high enough, multiple photons can be absorbed simultaneously and lead to ionization even if the energy of the individual photons is not sufficient. (c) In tunnel ionization, the laser light in the dipole approximation can be considered a classical field that is strong enough to bend the Coulomb potential of the atom, such that a tunnel barrier is created and the electron may tunnel out(Figure from [49]).*

- nanoplasmonic-fields interactions.

To simulate the PEs dynamics during the multiple ionization of dielectric NPs, a quasi-classical mean-field Monte-Carlo (M^3C) model was developed employing classical Mie theory [70, 71]. This model was applied to investigate PE angular distributions and laser-carrier-envelope-phase-controlled PE rescattering from 50 - 550 nm SiO_2 nanospheres [72], controlled near-field-enhanced electron acceleration from dielectric nanospheres [10], attosecond streaking spectroscopy of electron scattering in dielectric NPs [68], and ultrafast metallization of isolated dielectric and semiconducting NPs [73]. In this numerical model, electrons are liberated via tunnel ionization from randomly chosen surface atoms, based on Ammosov-Delone-Krainov (ADK) atomic tunnel-ionization rates [74]. PEs are assumed to be launched at the classical tunnel exit with zero initial velocities. Their subsequent motion in the electric fields of the incident laser pulse and induced plasmonic response is propagated classically. Electronic correlation and PE - residual-charge interactions during the propagation are accounted for at the mean-field level. Experimentally, strong-field photoemission from isolated dielectric SiO_2 NPs by intense 4 fs 720 nm and 25 fs 780 nm linearly polarized laser pulses were recently measured for different NP sizes and laser intensities by respectively Süßmann *et al.* [72] and Powell *et al.* [75].

1.6 Dissertation overview

The main focus of this dissertation is the theoretical investigation of laser - metal NP interactions using attosecond streaking and VMI spectroscopy.

In Chapter 2, we have developed a classical Monte-Carlo trajectory model to simulate the single-XUV-photon emission of gold conduction electrons in the electric field of delayed ultrashort IR (or visible) pulses. This model includes four distinct steps: (a) excitation of the PE by the XUV pulse, (b) transport of the excited PE to the surface, (c) escape of the PE from the surface, and (d) propagation of the released electron to the detector in the presence of the incident and induced plasmonic fields. By carefully analyzing simulated streaked spectra, we reconstructed the temporal information of the plasmonic excitation in the metal NPs.

In Chapter 3, based on the theoretical model developed in Chapter 2, we propose a scheme for the reconstruction of induced plasmonic near-fields at isolated metal NP surfaces from streaked PE spectra. We demonstrate the reconstruction of the plasmonic near-field distribution with sub-femtosecond temporal and sub-nanometer spatial resolution in comparison with the directly calculated induced plasmonic field.

In Chapter 4, we modeled strong-field ionization from metal NPs. Our numerical model includes: PE emission on the NP surface by an intense infrared laser pulse. PE propagation outside the nanosphere in the presence of the incident laser and induced plasmonic fields. It accounts for electron-electron, electron-residual charge, and image charge interactions. PE rescattering and recombination to the NP. Based on simulated PE-momentum distributions for 5 to 70 nm diameter gold nanospheres for two different intensities, and in comparison with measured VMI PE spectra, we scrutinize the effects of induced plasmonic field, electron-electron and electron-residual charge interactions, and PE rescattering and recombination.

In Chapter 5, we present summary and outlook.

Atomic units are used throughout this dissertation unless otherwise indicated.

Chapter 2

Characterization of induced nanoplasmonic fields in time-resolved photoemission: a classical trajectory approach applied to gold nanospheres

2.1 Introduction

In this chapter, we investigate the strong transient polarization of sub-infrared (IR)-wavelength-size gold nanospheres by an intense IR or visible pulse (Fig. 2.1; in the following text we refer to "IR" as including the visible spectral range). For linearly polarized incident IR pulses, the induced polarization resulting from the coherent driven motion of a large number of gold conduction electrons oscillates with the IR laser carrier frequency and generates the surface-enhanced inhomogenous plasmonic field. The driving IR and induced field are shifted by a phase that depends on the detuning of the IR-laser frequency from the plasmon resonance frequency of the NPs.

We developed a classical trajectory model to probe the plasmonic response of NPs by single-XUV-photon emission of gold conduction electrons in the electric field of delayed

ultrashort IR (or visible) pulses. During this laser-assisted XUV photoemission process, the streaking pulse thus has two distinct functions, as it both stimulates and probes the dielectric plasmonic response of the nanospheres. PEs released by the XUV pulse propagate inside the NP and are subject to elastic and inelastic collisions with electrons and nuclei of the nanosphere. Upon reaching the surface, they may get emitted and experience the net electric field of the streaking pulse and induced plasmonic field before possibly moving a macroscopic distance to the time-of-flight detector that registers their momentum for a given delay between the streaking pulse and ionizing single attosecond XUV pulse.

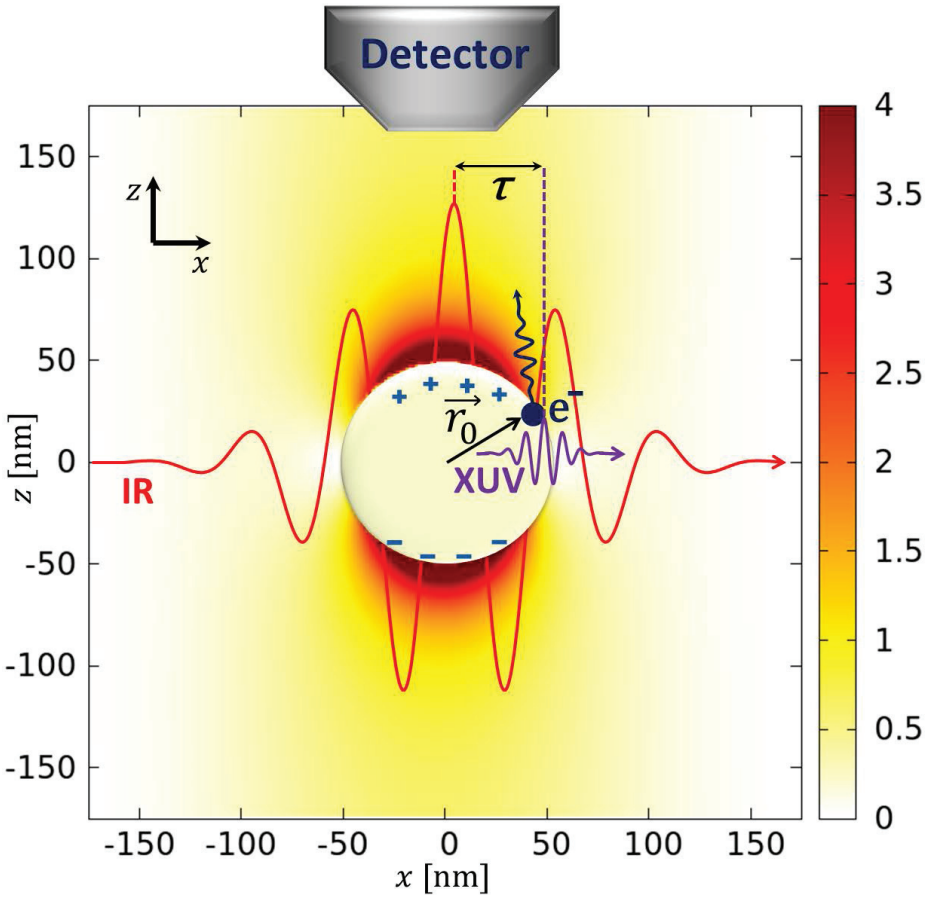

Figure 2.1: *Illustration of attosecond streaking spectroscopy of nanospheres. PEs are excited by an isolated XUV pulse at initial positions $\vec{r}_0$ with velocities $\vec{v}_0$. Upon leaving the nanosphere they experience the plasmonically enhanced field of the delayed IR streaking pulse. τ designates the time delay between the IR and XUV pulse. The size of the target and wavelength of laser pulses are not to scale.*

The described scenario is illustrated in Fig. 2.2 and can be thought of as a sequence of

four distinct steps:

1 Excitation of the PE by the XUV pulse at time t_e.

2 Transport of the excited PE to the surface during the time interval $t_s - t_e$.

3 Escape of the PE from the surface at time t_s.

4 Propagation of the released electron to the detector during the time interval $t_f - t_s$.

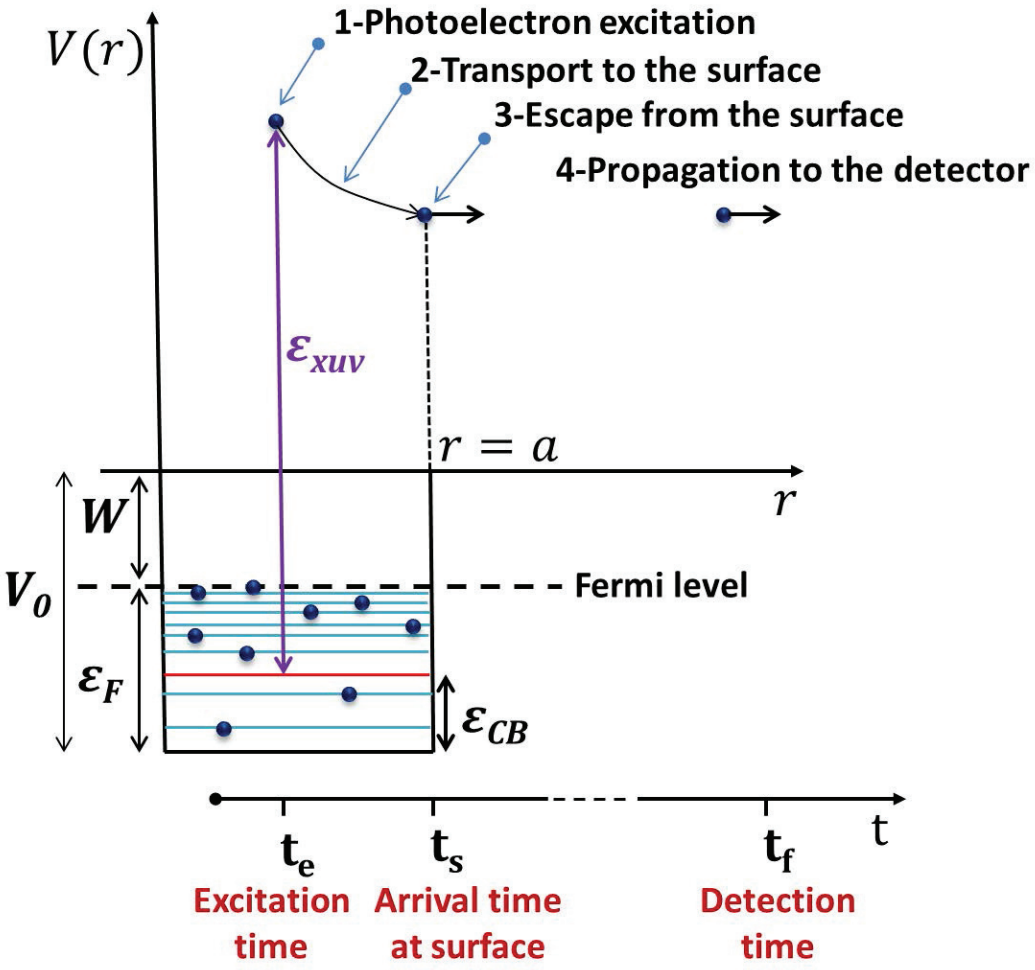

Figure 2.2: *Schematics of IR-streaked single-photon XUV photoemission from the occupied CB of a nanosphere.*

In our theoretical modeling of streaked photoemission from NPs we assume Gaussian XUV pulses with central energy $\varepsilon_{xuv}^{ctr} = 105$ eV and full temporal width at half intensity

maximum (FWHIM) $\Delta t_{xuv} = 287$ as, represented by the electric field

$$\vec{E}_{xuv}(\vec{r},t) = \vec{E}_{xuv,0} \exp\left(-2\ln 2 \frac{(t - k_{xuv}x/\varepsilon_{xuv}^{ctr})^2}{\Delta t_{xuv}^2}\right) \times \exp\left[-i(\varepsilon_{xuv}^{ctr} t - k_{xuv}x)\right], \tag{2.1}$$

with $k_{xuv} = \varepsilon_{xuv}/c$ and the speed of light in vacuum c. We further assume streaking pulses with Gaussian temporal profile,

$$\vec{E}_{inc}(\vec{r},t) = \vec{E}_{IR,0} \exp\left(-2\ln 2 \frac{(t + \tau - \frac{kx}{\omega})^2}{\Delta t_{IR}^2}\right) \times \exp(-i(\omega(t+\tau) - kx + \pi)), \tag{2.2}$$

pulse length (FWHIM) $\Delta t_{IR} = 2.472$ fs, $\lambda_{IR}^{ctr} = 2\pi/k = 2\pi c/\omega = 720$ and $\lambda_{IR}^{ctr} = 530$ nm central wavelength, and 10^{12} W/cm^2 peak intensity. The time delay τ between the XUV and the IR pulses we define to be positive if the IR pulses precede the XUV pulses. Both pulses are linearly polarized along the z axis and propagate along the positive x axis of our Cartesian coordinate system (Fig. 2.1). Based on the small cross section for XUV photoemission from gold NPs [76], we assume the NP to be transparent to the XUV pulses.

2.2 Theory

2.2.1 Induced plasmonic electric field

We model the CB of the nanosphere based on a spherical square-well potential with radius a and depth $V_0 = \varepsilon_F + W$, where we assume that the Fermi energy and the work function for gold NPs are equal to the Fermi energy ($\varepsilon_F = 5.53$ eV [77]) and the work function ($W = 5.1$ eV [78]) of the bulk gold (Fig. 2.2). Expressing the oscillating induced dipole

moment of the nanosphere,

$$\vec{P}(t) = (2\pi)^{-1/2} \int_{-\infty}^{\infty} d\omega e^{i\omega t} \vec{P}(\omega)$$
$$\vec{P}(\omega) = \epsilon_0 \epsilon_m \alpha(\omega) \vec{E}_{inc}(\vec{r}, \omega) \tag{2.3}$$

in terms of the complex polarizability $\alpha(\omega)$, the spectral components of the incident streaking pulse (2.2), $\tilde{\vec{E}}_{inc}(\vec{r}, \omega)$, and the relative permittivity of the surrounding medium (vacuum) ϵ_m (=1), the induced plasmonic field generated by $\vec{P}(t)$ is given by [79]

$$\vec{E}_{pl}(\vec{r}, t) = \frac{1}{\epsilon_m}[k^2(\hat{r} \times \vec{P}(t)) \times \hat{r}\frac{e^{ikr}}{r} + (3\hat{r}(\hat{r} \cdot \vec{P}(t)) - \vec{P}(t))(\frac{1}{r^3} - \frac{ik}{r^2})e^{ikr}], \tag{2.4}$$

where $\hat{r}$ is a unit vector in the direction of $\vec{r}$. The dipole approximation underlying this expression is justified by the NP radii in our numerical examples below not exceeding 50 nm and thus being significantly smaller than the wavelength of the streaking pulse [80].

In order to explain the colors of colloidal gold particles in solution, Mie in 1908 applied classical electrodynamics to the scattering and absorption of electromagnetic radiation by dielectric spheres [70]. Following Mie's approach, for radii $a < 0.1\lambda_{IR}^{ctr}$ the complex polarizability of the nanosphere can be written as [81]

$$\alpha(\omega) = \frac{9 - 0.9(\epsilon(\omega) + \epsilon_m)s^2 + O(s^4)}{3 + 9\epsilon_m/(\epsilon(\omega) - \epsilon_m) - (0.3\epsilon(\omega) + 3\epsilon_m)s^2 - i2\epsilon_m^{3/2}s^3 + O(s^4)} V, \tag{2.5}$$

in terms of expansions of the numerator and denominator in the dimensionless size parameter $s = 2\pi a/\lambda_{IR}^{ctr}$, the frequency-dependent dielectric function $\epsilon(\omega)$, and the volume of the nanosphere, $V = (4/3)\pi a^3$. While a square-well potential is obviously a crude representation of a nanosphere' s valence electronic structure, our sampling over all occupied conduction-band (CB) states and the XUV-pulse spectral profile (discussed below) tends to average over details in the target's band structure, which we thus assume to be of secondary relevance

to the description of currently observable streaked PE spectra. For the numerical example discussed below, the maximal value of s is $s_{max} = 0.57$, justifying our neglect of terms of the order s^4 and higher.

While $\alpha(\omega)$ is calculated for the specific (spherical) symmetry and depends on the size of our target, we represent the dielectric function in (2.5) within the Drude-Lorentz model [82, 83] for bulk gold in closed analytical form as

$$\epsilon(\omega) = \epsilon_\infty - \frac{\omega_{pl}^2}{\omega(\omega + i\gamma_{pl})} + \sum_{p=1}^{2} A_p \Omega_p \left(\frac{e^{i\phi_p}}{\Omega_p - \omega - i\Gamma_p} + \frac{e^{-i\phi_p}}{\Omega_p + \omega + i\Gamma_p} \right). \tag{2.6}$$

The first two terms constitute the standard Drude model [77, 84] with the high-frequency-limit dielectric function $\epsilon_\infty = 1.1431$, plasma frequency $\omega_{pl} = 1.3202 \times 10^{16}$ rad/s, and plasmon damping constant $\gamma_{pl} = 1.0805 \times 10^{14}$ rad/s. The remaining terms in (2.6) relate to interband transitions which are represented by Lorentz oscillators with oscillator strengths $\Omega_1 = 3.8711 \times 10^{15}$ rad/s and $\Omega_2 = 4.1684 \times 10^{15}$ rad/s, spectral widths $\Gamma_1 = 4.4642 \times 10^{14}$ rad/s and $\Gamma_2 = 2.3555 \times 10^{15}$ rad/s, amplitudes $A_1 = 0.26698$ and $A_2 = 3.0834$, and phases $\phi_1 = -1.2371$ and $\phi_2 = -1.0968$. The parameters Ω_p, Γ_p, A_p, and ϕ_p are obtained in Ref. [85] by fitting experimental optical data for bulk gold. Since in our numerical applications the streaking pulses are sufficiently long to have very small spectral widths, we can ignore the variation of $\epsilon(\omega)$ with ω and instead employ its value at the central frequency $2\pi c/\lambda_{IR}^{ctr}$ of the streaking pulse as a dielectric constant, where c designates the speed of light in vacuum.

The enhancement of the net electric field near the nanosphere surface varies with the degree of latitude and is largest at the poles, the poles $\vec{r}_p = (0, 0, \pm a)$ being defined with regard to the polarization direction of the IR pulses. Figure 2.3 shows the plasmonic-field enhancement

$$\eta_{pole}(\lambda_{IR}^{ctr}) = |\vec{E}_{inc} + \vec{E}_{pl}|/|\vec{E}_{inc}| \tag{2.7}$$

as a function of the streaking-pulse wavelength for nanospheres with radii between 5 and

50 nm. As expected from a simple box-quantization consideration, $\eta_{pole}(\lambda_{IR}^{ctr})$ sensitively depends on the NP size, and its maximum red-shifts as the particle size increases.

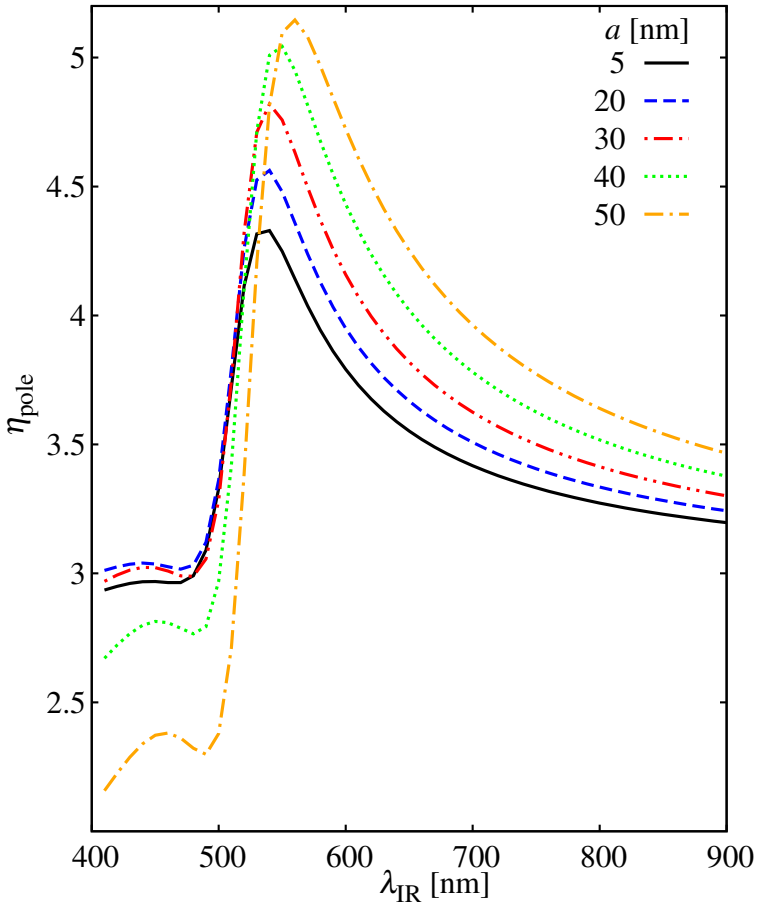

Figure 2.3: *Plasmonic-field enhancement at the poles of gold nanospheres of different radii a as a function of the wavelength* λ_{IR}^{ctr} *of the incident* 10^{12} W/cm^2 *peak intensity pulse.*

2.2.2 Trajectory calculation

Following the 4-step sequence of PE excitation, transport, escape, and propagation to the detector illustrated in Fig. 2.2, we numerically calculate PE trajectories for given initial positions $\vec{r}_0$ and initial velocities $\vec{v}_0$.

Excitation

We define our time scale by assuming the center of the XUV pulse to pass the $x = 0$ plane at time zero (Fig. 2.1) and refer to the "excitation time" $t_e = x_0/c$ as the instant when a conduction electron is excited and released by absorption of a single XUV photon at an excitation point $\vec{r}_0 = (x_0, y_0, z_0)$ inside the NP. This time is different for different excitation positions and equal to the propagation time of the XUV pulse between the reference plane at $x = 0$ and the excitation point (Fig. 2.4). The delayed excitation is specific to our classical modeling of the photoemission process. While it is negligible for photoemission from atoms, the travel time of XUV light across the largest nanospheres of 50 nm radius studied in our numerical examples below is 334 as. Accounting for delays between the XUV excitation of conduction electrons at different locations is therefore crucial for our calculation of attosecond time-resolved streaking spectra.

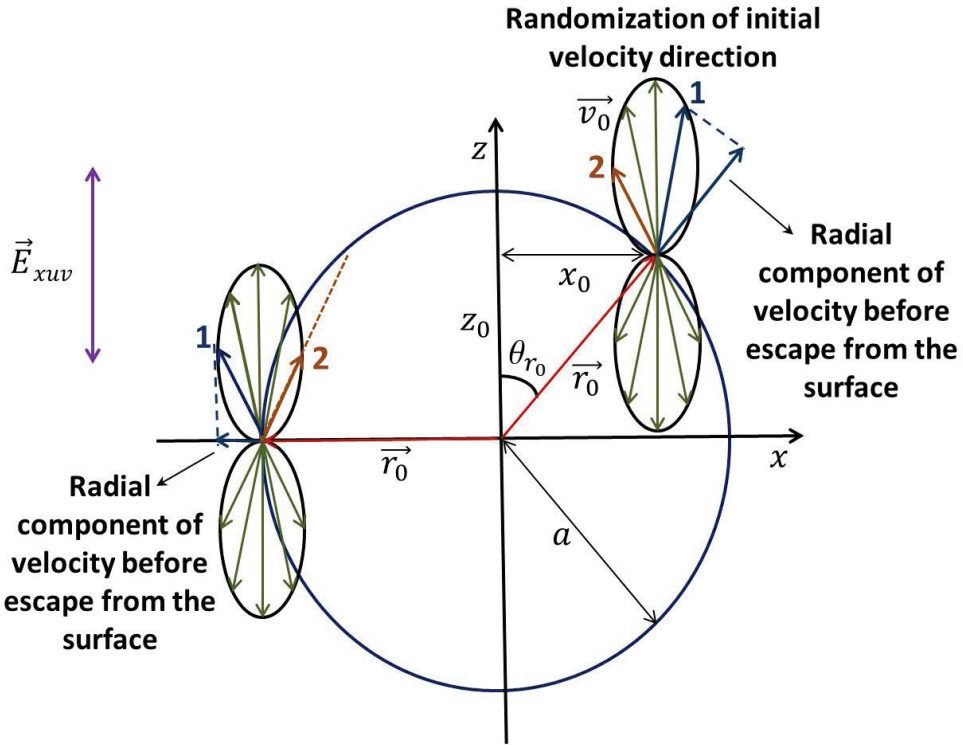

Figure 2.4: *Schematics for the excitation time calculation and illustration of the "surface effect" (blue vectors labeled with "1") and "transport effect" (brown vectors labeled with "2") for two different points on the surface of the nanosphere.*

Transport to the surface

After excitation, the PE propagates inside the NP towards the surface, changing its momentum and losing kinetic energy due to elastic and inelastic collisions. We will refer to this change of the PE's propagation direction and energy as "transport effect". We include this effect in both calculating individual electron trajectories and in the sampling over trajectories (cf., Sec. 2.2.3 below).

In the numerical examples discussed in Sec. 2.3 below, released PEs propagate inside the NP with kinetic energies between approximately 85 to 110 eV. In this energy range, the inelastic mean free path (IMFP) λ_i varies insignificantly by about 1% and will be considered as a constant value of 0.441 nm [86].

We model transport effects inside the NP on individual electron trajectories within the Drude model for metals [77] by introducing the frictional damping force

$$\vec{F}(\vec{v}) = -m^*\vec{v}/\tau_{relax} \tag{2.8}$$

in Newton's equation of motion

$$m^*\frac{d}{dt}\vec{v}(\vec{r},t) = \vec{F}(\vec{v}) \quad , \quad r < a, \tag{2.9}$$

where $m^* = 1.1$ is the effective electron mass [77]. The relaxation time of bulk gold conduction electrons is $\tau_{relax} = \lambda_i/v_F = 30$ fs, with respect to the Fermi velocity $v_F = 1.40 \times 10^8$ cm/s [77]. Since gold is a good conductor, the electric field inside the nanosphere is negligible and therefore absent in (2.9). For a given initial point $(\vec{r}_0, \vec{v}_0)$ in phase space, the position and velocity of the released electron inside the NP as a function of time then

immediately follow from (2.9) as

$$\vec{v}(t) = \vec{v}_0 \; e^{-\left(\frac{t-t_b}{\tau_{relax}}\right)}$$
$$\vec{r}(t) = \vec{r}_0 + \tau_{relax} \; \vec{v}_0 \left[1 - e^{-\left(\frac{t-t_b}{\tau_{relax}}\right)}\right]. \tag{2.10}$$

Escape from the surface

An additional energy loss occurs as the released PE leaves the NP due to the increase of potential energy at the particle's surface. For the spherical square-well potential in our model, energy conservation requires the radial and tangential velocity components of the electron just before reaching the surface at $r = a$ ($v_{sr}^{(-)}$ and $v_{st}^{(-)}$, respectively) and just outside the surface ($v_{sr}^{(+)}$ and $v_{st}^{(+)}$, respectively) to be related according to

$$v_{sr}^{(+)} = \sqrt{m^* v_{sr}^{(-)2} - 2V_0}$$
$$v_{st}^{(+)} = \sqrt{m^*} v_{st}^{(-)}. \tag{2.11}$$

The radial velocity $v_{sr}^{(-)}$ determines whether the electron is energetically able to leave the target and is thus of particular importance in our calculation of PE spectra. Taking into account that electrons are released with a nonuniform distribution of initial velocities $\vec{v}_0$, that follow an assumed dipole distribution around the polarization direction of the XUV pulse, explains that the radial velocity component $v_{sr}^{(-)}$ tends to decrease for initial positions near the surface with increasing degree of latitude θ_{r_0}. This favors electron emission at the poles ($\theta_{r_0} = 0°$ or $180°$) and suppresses emission at the equator ($\theta_{r_0} = 90°$). This effect is illustrated by the blue velocity vectors that are labeled with "1" in Fig. 2.4 and will be referred to as "surface effect". Surface effects are thus expected to strongly suppress emission near the equator.

Emission from the equator is also suppressed due to electron transport effects as illustrated by the brown velocity vectors labeled "2" in Fig. 2.4. Moving the release point $\vec{r}_0$

on the surface from the pole to the equator, the propensity for long pathlengths inside the particle increases, reducing the probability for electron emission and propagation toward the detector. In addition to surface effects, transport effects noticeably influence PE spectra. This is confirmed by our numerical applications and further discussed in Sec. 2.3 below.

Propagation to the detector

Assuming complete screening at the surface of the metallic nanosphere, escaping PEs are subjected to (i) the incident IR and induced plasmonic electric field upon reaching the surface and (ii) a reduction of their mass from the effective value m^* to the free electron mass $m = 1$. We calculate the final PE velocity $\vec{v}_f^{det}(\vec{r}_0, \vec{v}_0, \tau)$ by numerically solving the classical equation of motion

$$\frac{d}{dt}\vec{v}(\vec{r}, t) = -\vec{E}_{inc}(\vec{r}, t) - \vec{E}_{pl}(\vec{r}, t) \quad , \quad r > a, \tag{2.12}$$

using a 4^{th} order Runge-Kutta method for a given time delay τ, initial position $\vec{r}_0$, and initial momentum $\vec{v}_0$. Not all emitted electrons reach the detector. In the numerical examples discussed below we count PEs as detected if their final velocity direction lies within a cone about the positive z axis with an opening angle of $\theta_{acc} = 45°$.

2.2.3 Sampling trajectories

We include a large number of PE trajectories by Monte-Carlo sampling [87] over their initial phase-space points $(\vec{r}_0, \vec{v}_0)$. This sampling is carried out based on the probability density function (PDF) $\rho(\vec{r}_0, \vec{v}_0)$ that lends relative weights to the trajectories. Having described our calculation of individual trajectories in the previous subsection, we now detail our modeling of the PDF under the assumption that the initial PE position $\vec{r}_0$ and velocity $\vec{v}_0$ are independent, allowing the separation

$$\rho(\vec{r}_0, \vec{v}_0) = \rho_{pos}(\vec{r}_0)\rho_{vel}(\vec{v}_0). \tag{2.13}$$

Initial positions

For the purpose of modeling $\rho_{pos}(\vec{r}_0)$, we assume a constant electron density inside the nanosphere. Even though the charge redistribution on the NP surface by the streaking IR pulse creates a large plasmonic field, the number of electrons displaced by the action of the incident IR electromagnetic wave is negligible in comparison to the total number of free electrons in the CB. We can therefore safely suppose that the electron density remains uniformly distributed inside the nanosphere.

Consistent with our assumption made for the calculation of individual trajectories of the NP being transparent to the XUV pulse, we further assume that the XUV-photoemission rate is uniform inside the NP. This amounts to neglecting the macroscopic effect of the attenuation of the XUV pulse while (strictly speaking inconsistently) still allowing for XUV-triggered single-photon photoemission. Under these presuppositions, the PDF for initial positions is

$$\rho_{pos}(\vec{r}_0) = \frac{1}{V} \begin{cases} 1 & , \quad r_0 \leq a \\ 0 & , \quad r_0 > a \end{cases} . \tag{2.14}$$

Initial velocities

The velocity distribution resulting from the excitation of conduction electrons in the linearly polarized electric field of the XUV pulse is cylindrically symmetrical about the XUV polarization direction (z axis). Therefore, representing $\vec{v}_0$ in spherical coordinates, the PDF $\rho_{vel}(\vec{v}_0) = \rho_{vel}(v_0, \theta_{v_0})$ is independent of the azimuthal angle ϕ_{v_0}. Assuming that for the narrow range of PE kinetic energies of relevance in our numerical applications below the initial PE angular distribution does not depend on the electron speed v_0, we can separate v_0- and θ_{v_0}-dependent contributions to the velocity PDF, such that

$$\rho_{vel}(\vec{v}_0) = \frac{1}{2\pi v_0^2 \sin(\theta_{v_0})} \rho_v(v_0) \rho_\theta(\theta_{v_0}). \tag{2.15}$$

The angle-dependent factor $\rho_\theta(\theta_{v_0})$ reflects the angular distribution of PEs due to single-

photon emission. For the assumed dipolar distribution the normalized PDF in θ_{v_0} is

$$\rho_\theta(\theta_{v_0}) = \frac{4}{\pi}\cos^2(\theta_{v_0}), \tag{2.16}$$

which immediately follows by applying Fermi's golden rule to single-photon electron emission from initial zero-angular-momentum atomic states [76]. We note that, since the detector is placed along the positive z axis, PEs with final velocities along the negative z axis are not detected. Disregarding the very small chance of large-angle deflections of released PEs inside the NP and in the external IR electromagnetic field, we restrict θ_{v_0} to the interval $[0, \pi/2]$ and normalize $\rho_\theta(\theta_{v_0})$ over this interval.

We determine $\rho_v(v_0)$ within the free-electron-gas model for CB electrons [88] based on the electronic density of states

$$\rho_{CB}(\varepsilon_{CB}) = f_{FD}(\varepsilon_{CB})\frac{3}{2}\varepsilon_F^{-\frac{3}{2}}\sqrt{\varepsilon_{CB}}, \tag{2.17}$$

with the Fermi-Dirac distribution function

$$f_{FD}(\varepsilon_{CB}) = \frac{1}{\exp((\varepsilon_{CB}-\mu)/k_BT)+1} \tag{2.18}$$

and conduction-electron energy ε_{CB}. Neglecting the small change of the overall electron-kinetic-energy distribution at room temperature relative to $T = 0$ K, we assume $T = 0$ K, i.e.,

$$\rho_{CB}(\varepsilon_{CB}) = \begin{cases} \frac{3}{2}\varepsilon_F^{-\frac{3}{2}}\sqrt{\varepsilon_{CB}} & , \quad 0 \le \varepsilon_{CB} \le \varepsilon_F \\ 0 & , \quad \text{otherwise.} \end{cases} \tag{2.19}$$

The squared Fourier transformation of Eq. (2.1) results in the spectral profile of the XUV pulse, which, upon normalization over all XUV photon energies $\varepsilon_{xuv} > 0$, turns into the PDF

$$\rho_{xuv}(\varepsilon_{xuv}) = (\frac{2}{\pi\sigma_{xuv}^2})^{\frac{1}{2}}\exp(-\frac{(\varepsilon_{xuv}-\varepsilon_{xuv}^{ctr})^2}{2\sigma_{xuv}^2}), \tag{2.20}$$

with the standard deviation $\sigma_{xuv} = 1/\Delta t_{xuv} = 2.7$ eV corresponding to the XUV spectral width (FWHIM) of 6.35 eV.

Since $\rho_{CB}(\varepsilon_{CB})$ and $\rho_{xuv}(\varepsilon_{xuv})$ are independent distributions, their convolution results in the PDF for XUV-excited PEs

$$\rho_{CB,xuv}(\varepsilon^*_{CB}) = \int_0^\infty d\varepsilon_{CB}\ \rho_{CB}(\varepsilon_{CB})\ \rho_{xuv}(\varepsilon^*_{CB} - \varepsilon_{CB}), \tag{2.21}$$

where the energy of the excited CB PE is given by $\varepsilon^*_{CB} = \varepsilon_{CB} + \varepsilon_{xuv}$ (Fig. 2.2). The dispersion relation $v_0 = (2\varepsilon^*_{CB}/m^*)^{1/2}$ for excited CB electrons inside the NP now leads to the PDF for the magnitude of the PE velocity immediately after XUV excitation,

$$\begin{aligned}\rho_v(v_0) &= \int d\varepsilon^*_{CB}\rho_{CB,xuv}(\varepsilon^*_{CB})\ \delta\left(v_0 - \sqrt{2\varepsilon^*_{CB}/m^*}\right) \\ &= m^* v_0 \rho_{CB,xuv}(\frac{1}{2}m^* v_0^2).\end{aligned} \tag{2.22}$$

Monte-Carlo sampling

In section 2.2.2 we included transport effects in the calculation of individual PE trajectories in terms of the IMFP λ_i. This results in the deceleration of the released electron inside the NP [cf. Eq. (2.10)]. Since the deceleration and change of propagation direction inside the NP affects the electron-detection probability, the PDF needs to take into account the effective loss of PEs due to collisions. We incorporate the effects of the change in propagation direction and energy loss in terms of the relative probability of escape

$$\rho_l(l) = \frac{\exp(-l(\vec{r}_0, \vec{v}_0)/\lambda_i)}{\lambda_i(1 - \exp(-\frac{2a}{\lambda_i}))} \tag{2.23}$$

that depends on the distance $l(\vec{r}_0, \vec{v}_0)$ the PE covers inside the NP before reaching its surface and on λ_i. We thus count excited electrons that change their direction of propagation due to collisions as lost, i.e, as either being able to escape from the NP without reaching the detector or as not being able to escape. This implies that PEs which are released further

away from the surface tend to have a lower probability to be emitted from the nanosphere.

Combining the transport effects as described in Eq. (2.22) with Eqs. (2.13) and (2.14) leads to the effective phase-space PDF

$$\rho_{tot}(\vec{r}_0, \vec{v}_0) = \rho(\vec{r}_0, \vec{v}_0)\ \rho_l(l). \tag{2.24}$$

The distribution of observable final PE velocities $\vec{v}_f = (v_f, \theta_{v_f}, \phi_{v_f})$ is obtained from ρ_{tot} and the final asymptotic electron velocities $\vec{v}_f^{det}(\vec{r}_0, \vec{v}_0, \tau)$ as

$$\begin{aligned}&\rho_f(\vec{v}_f, \tau) = \\ &\int\int d\vec{r}_0\ d\vec{v}_0\ \rho_{tot}(\vec{r}_0, \vec{v}_0)\ \delta\left(\vec{v}_f - \vec{v}_f^{det}(\vec{r}_0, \vec{v}_0, \tau)\right).\end{aligned} \tag{2.25}$$

From this expression we obtain the streaked photoemission spectra, i.e., the PE yield

$$Y(K_f, \tau) = N v_f \int_{-\theta_{acc}/2}^{\theta_{acc}/2} \sin\theta_{v_f} d\theta_{v_f} \int_0^{2\pi} d\phi_{v_f} \rho_f(\vec{v}_f, \tau) \tag{2.26}$$

as a function of the final PE kinetic energy $K_f = \frac{1}{2}v_f^2$ and the delay τ. With the factor

$$N = [\max_{K_f,\tau} Y(K_f, \tau)]^{-1} \tag{2.27}$$

we normalize the streaked PE spectrum to its maximal yield.

2.3 Numerical results and discussion

In this section we are going to characterize the plasmonic field near the surface of the nanosphere by examining streaked PE *spectra* and streaking *curves*. We will represent streaked spectra as color-coded graphs of the normalized PE yield $Y(K_f, \tau)$ (2.26). We numerically evaluate Eq. (2.26) for fixed delays by binning final PE kinetic energies resulting from trajectory calculations, $K_f^{det} = \frac{1}{2}\vec{v}_f^{det}(\vec{r}_0, \vec{v}_0, \tau)^2$, in small equidistant kinetic energy

intervals of width $\Delta K_f = 0.6$ eV. For every spectrum we sample over 6,633,000 trajectories and compose the PE yield as a histogram based on the kinetic energy bins. All spectra are calculated for a detector acceptance angle of $\theta_{acc} = 45°$. In our numerical studies we found that typically about 50% of the included trajectories contribute to the detected electron yield. The large number of not "detected" trajectories is due to PEs failing to reach the acceptance cone of the detector.

We will refer to streaking *curves* as graphs of the PE kinetic energy $K_f^{det}(\vec{r}_0, \vec{v}_0, \tau) = \frac{1}{2}\vec{v}_f^{det}(\vec{r}_0, \vec{v}_0, \tau)^2$ resulting from a single initial point inside the NP $\vec{r}_0$ and from a given initial velocity $\vec{v}_0$ as a function of τ. Since streaked spectra can be understood as the superposition of streaking curves, we will discuss streaking curves with regard to the degree of spatial resolution at which streaking spectroscopy allows the imaging of plasmonic fields.

2.3.1 Emission-position dependence

Emission-depth dependence

Figure 2.5(a) shows streaking curves $K_f^{det}(\vec{r}_0, \vec{v}_0, \tau)$ for $a = 50$ nm gold nanospheres obtained from electron trajectories that start at the detector-facing pole $\vec{r}_p(0, 0, a)$ for five different radial distances r_0 between 45 and 50 nm. The electrons are assumed to be emitted from the Fermi level with emission direction $\theta_{v_0} = 0°$. The diagonal shift of the curves suggests that PEs reach the detector with an increasing energy loss and time delay when r_0 moves from the surface towards the center of the nanosphere. These are expected manifestations of the transport effect discussed in Sec. 2.2.2. PEs which are excited deeper inside the NP require more time to reach the surface, causing an increasing time delay in the streaking curves. The delay difference amounts to 0.85 fs between electrons that start at $r_0 = 50$ and 45 nm. In addition, the increasing pathlength inside the nanosphere increases the chance for PEs experiencing collisions during their transport to the surface, causing the likewise increasing kinetic energy loss. Relative to trajectories that start at the surface ($r_0 = 50$ nm), the energy loss depicted in the streaking curve amounts to 6 eV if the release point is shifted to $r_0 = 45$ nm.

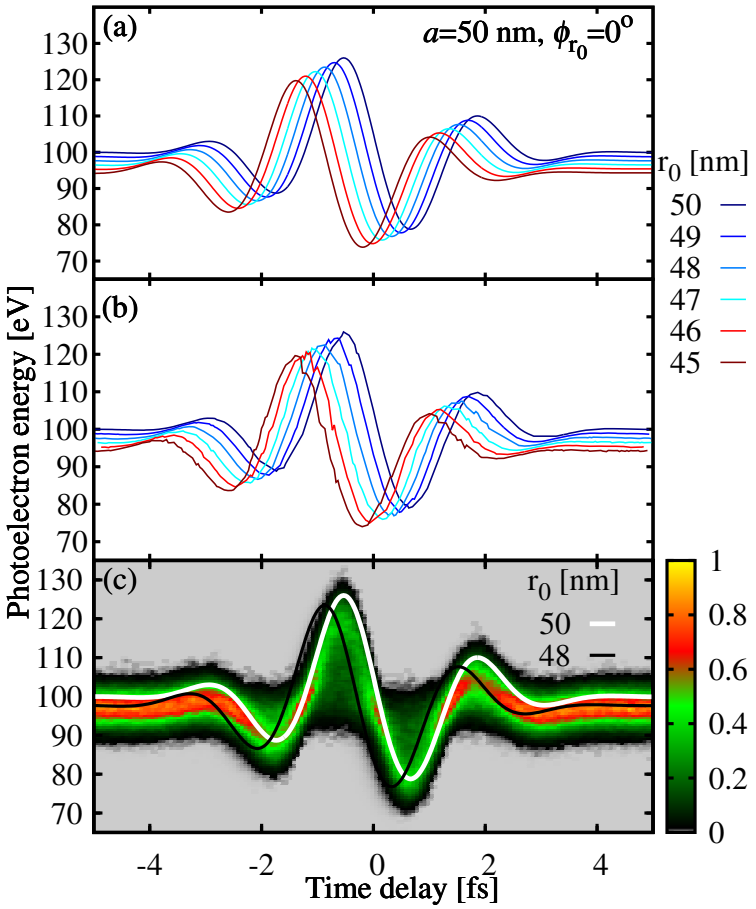

Figure 2.5: *Streaking curves and streaked spectrum from 50 nm Au nanospheres. (a) Streaking curves for PEs emitted from the Fermi level with emission direction $\theta_{v_0} = 0°$ from five release points $(r_0, \theta_{r_0} = 0°)$ located on an axis joining the detector-facing pole and center of the nanosphere. (b) Streaking curves for the same five points and emission from the Fermi level for randomized velocity directions θ_{v_0}. (c) Simulated streaked spectrum and two streaking curves from release points $(r_0 = 50, \theta_{r_0} = 0°)$ (white curve) and $(r_0 = 48, \theta_{r_0} = 0°)$ (black curve). The spectrum is calculated for emission from the entire occupied CB, while the two streaking curves are calculated for emission from the Fermi level only. The spectrum is normalized to its maximal yield. The assumed emission direction for the two streaking curves is $\theta_{v_0} = 0°$.*

The streaking curves in Fig. 2.5(b) are calculated for the same five release points and emission from the Fermi level only as in Fig. 2.5(a). However, the initial PE velocity directions are selected randomly for each delay τ and weighted with the dipole distribution (2.16). By randomizing the velocity directions, PEs acquire different path lengths inside the NP, resulting in different escape probabilities and energy losses that explain the appearance of small fluctuations in the streaking curves. As expected, these fluctuations become more

pronounced as the release point is shifted towards the nanosphere center. The fact that even after velocity-direction randomization we basically get the same streaking curves for each initial position indicates that every radial emission point uniquely translates into a corresponding streaking curve.

Figure 2.5(c) shows how two individual streaking curves for emission from the Fermi level and surface of 50 nm radius gold nanospheres with emission direction $\theta_{v_0} = 0°$ from initial points $(r_0 = 50, \theta_{r_0} = 0°)$ and $(r_0 = 48, \theta_{r_0} = 0°)$ contribute to the streaked spectrum. This graph illustrates that streaked spectra contain (radial) spatial information in addition to temporal information.

Emission-angle dependence

Figures 2.6(a) and 2.7(a) show streaking curves for four release points on the nanosphere surface $(r_0 = a)$ at different latitudes θ_{r_0} between the detector-facing pole and equator of the sphere for emission from the Fermi level with emission direction $\theta_{v_0} = 0°$. Figures 2.6 and 2.7 show results for radii of 50 and 5 nm, respectively. The striking decrease of the streaking oscillation amplitude for increasing θ_{r_0} is due to the inhomogeneous plasmonic field being the strongest at the pole and decreasing in strength towards the equator of the nanosphere. The absence of streaking curves for $\theta_{r_0} = 90°$ in Figs. 2.6(a) and 2.7(a) is due to the released PEs having insufficient kinetic energy to overcome the potential barrier at the nanosphere surface (surface effect) and transport effects.

The streaking curves in Figs. 2.6(b) and 2.7(b) are calculated for the same four points and for emission from the Fermi level as the curves in Figs. 2.6(a) and 2.7(a), respectively, but for randomized velocity directions. As in Fig. 2.5(b) above, the fluctuations in Figs. 2.6(b) and 2.7(b) are due to velocity randomization. As θ_{r_0} increases, moving from the pole towards the equator, the fluctuations increase due to the increasing transport path lengths $l(\vec{r}_0, \vec{v}_0)$ and energy loss that PEs experience before reaching the surface. The fact that velocity randomization does not change the overall shape of the streaking curves indicates that, for emission from the surface, every emission latitude is associated with a streaking curve.

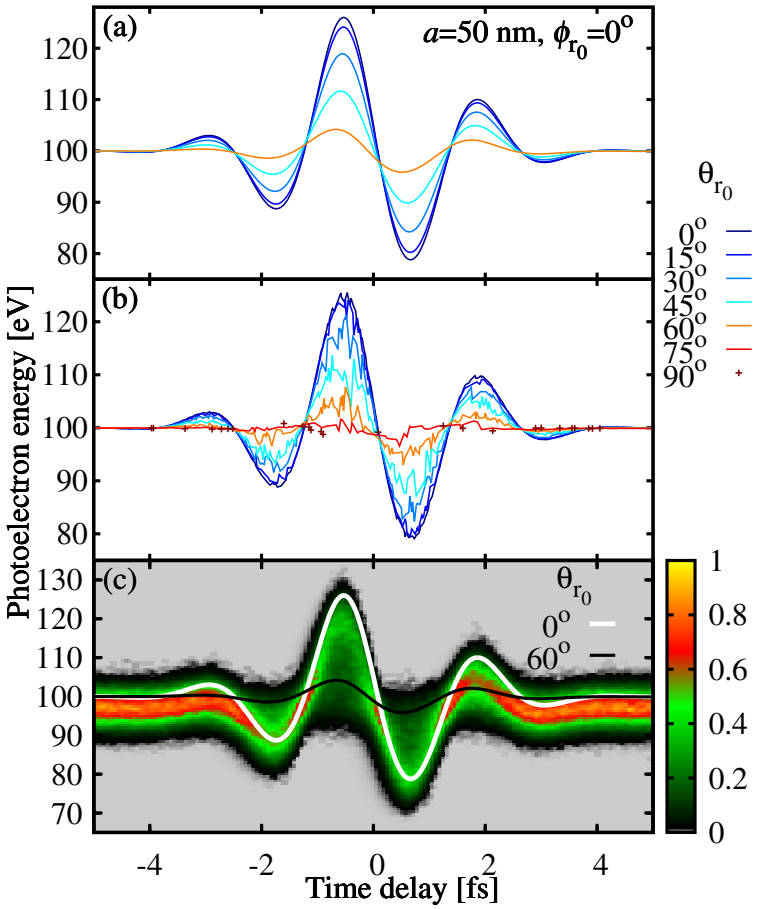

Figure 2.6: *Streaking curves and streaked spectra from* 50 *nm Au nanospheres. (a) Streaking curves for PEs emitted from the Fermi level with emission direction* $\theta_{v_0} = 0°$ *for four emission latitudes* θ_{r_0} *between the pole and equator on the nanosphere surface. (b) As (a) for randomized velocity directions* θ_{v_0}*. (c) Simulated streaked spectrum and two streaking curves from release points* $(r_0 = a, \theta_{r_0} = 0°)$ *(white curve) and* $(r_0 = a, \theta_{r_0} = 60°)$ *(black curve). The spectrum is calculated for emission from the entire occupied CB, while the two streaking curves are calculated for emission from the Fermi level only. The spectrum is normalized to its maximal yield. For the two streaking curves the assumed emission direction is* $\theta_{v_0} = 0°$*.*

Since larger nanospheres allow for longer propagation pathlengths inside the particle, the fluctuations for 50 nm radius spheres in Figs. 2.6(b) are more pronounced than for 5 nm radius spheres in 2.7(b).

Figures 2.6(c) and 2.7(c) show the contribution of two individual streaking curves to the streaked spectrum for 50 and 5 nm radii, respectively. These streaking curves are calculated for electrons emitted from the Fermi level at release points $(r_0 = a, \phi_{r_0} = 0°, \theta_{r_0} = 0°)$ and $(r_0 = a, \phi_{r_0} = 0°, \theta_{r_0} = 60°)$. They show that streaked spectra contain angular spatial

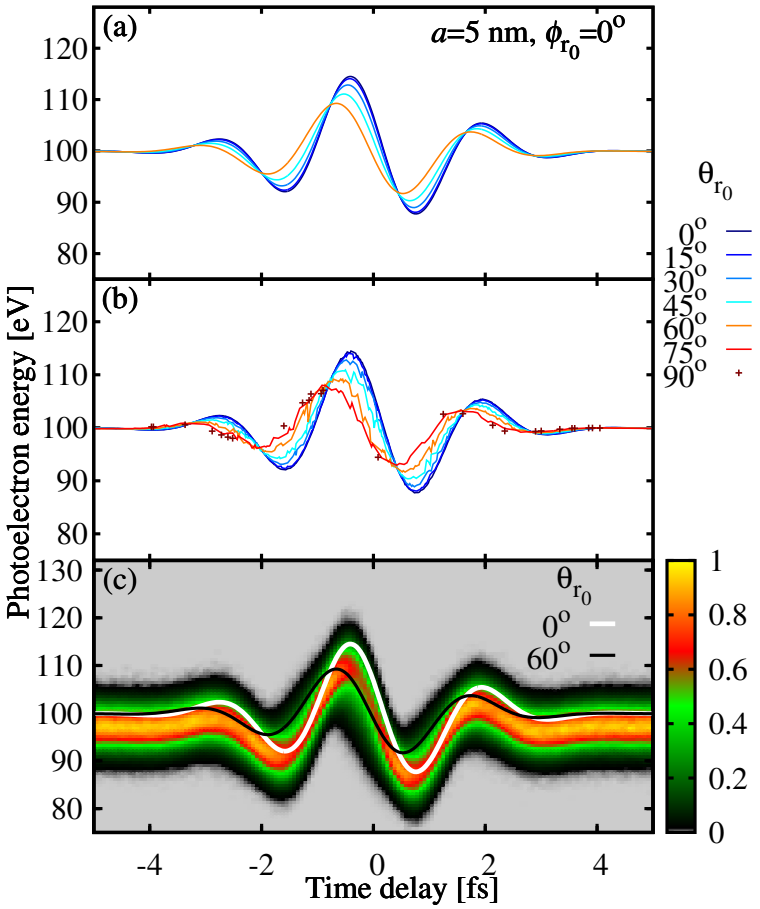

Figure 2.7: *As Fig. 2.6 for 5 nm Au nanospheres.*

information in addition to radial spatial and temporal information.

Our study of the emission-depth and emission-angle dependence suggests that each emission point $\vec{r}_0$ is mapped on a corresponding streaking curve which contributes to the streaked spectrum. Therefore, in addition to temporal characteristics we expect streaked PE spectra to allow the distinction of local emission characteristics and the plasmonic field distribution near the nanosphere surface with some degree of spatial resolution. If we consider streaked spectra as the sum of all streaking curves with a weight function that depends on the path-length $l(\vec{r}_0, \vec{v}_0)$, we can relate high electron yields to high densities of streaking curves. Delays at which streaking curves intersect thus tend to correspond to large PE yields. This is confirmed by comparing the streaking curves in Figs. 2.5, 2.6, and 2.7 with the respective spectra in Figs. 2.5(c), 2.6(c), and 2.7(c).

2.3.2 Conduction-band, surface, and transport effects

The spectra shown in Figs. 2.6(c) and 2.7(c) are obtained for "full" simulations, including electron emission from the entire occupied part of the CB, and after sampling over release points $(\vec{r}_0, \vec{v}_0))$ in the nanosphere $(r_0 \leq a)$. In this subsection, we will investigate the effects of restricting the release locations and initial energy of the PEs. Figure 2.8(a) is generated by sampling over the XUV spectral energy profile, assuming that all PEs are emitted from the Fermi level only and released from the surface $(r_0 = a)$ by the XUV pulse. Classical simulations with the same restrictions on the initial energy and release location of the active electron were performed earlier in Ref. [39] and are shown in Fig. 2.8(b) to be in good overall agreement with our result.

We extended the model suggested in Ref. [39] by (i) representing the CB as a spherical square well potential, thereby including the surface effect, (ii) sampling over the entire conduction bandwidth, and (iii) sampling not only over electron trajectories that initiate at the surface, but adding PEs released inside the NP, thus including transport effects. Each of these extensions has a noticeable impact on streaked spectra. The spectrum in Fig. 2.8(c) shows results of our full simulation, including all of the above extensions. We generated Fig. 2.8(d) under the same assumptions as Fig. 2.8(c), but without sampling over the conduction bandwidth, assuming emission from the Fermi level only.

The comparison of Figs. 2.8(c) and 2.8(d) reveals that the inclusion of initial states from the entire occupied CB shifts the center of energy (COE) of the streaking trace to lower energies, as expected with regard to energy conservation. This downward energy shift amounts to $\Delta_{COE} = 2.22$ eV. Within the free-electron-gas model Eq. (2.19) for the gold CB, Δ_{COE} is related to the average CB energy $< \varepsilon_{CB} >$ according to

$$\Delta_{COE} = \varepsilon_F - < \varepsilon_{CB} > = \frac{2}{5}\varepsilon_F. \tag{2.28}$$

This allows the retrieval of the Fermi energy from our simulated streaked spectra as $\varepsilon_F = \frac{5}{2}\Delta_{COE} = 5.50$ eV, in good agreement with the theoretical value, $\varepsilon_F = 5.53$ eV, of Ref. [77].

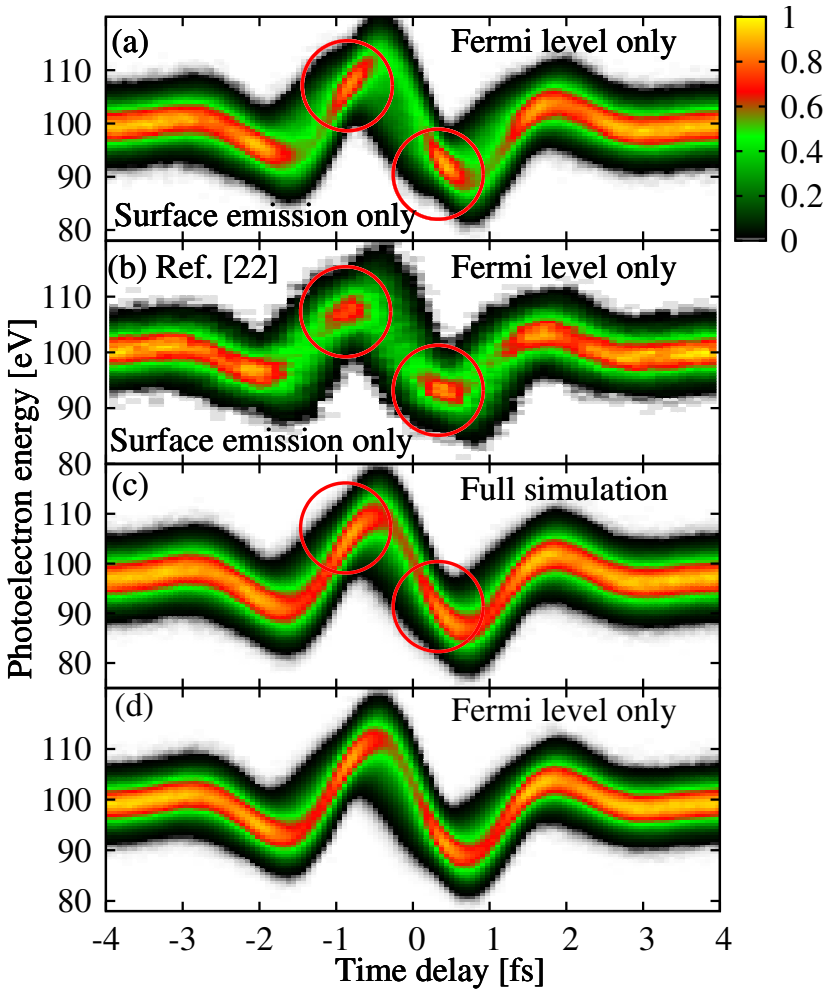

Figure 2.8: *Simulated streaked spectra for $a = 5$ nm radius Au nanospheres normalized individually to their maximal yields. (a) Restricted sampling over particle surface and Fermi level only. (b) Adapted from Ref. [39]. (c) Full simulation, including sampling over the occupied conduction band, the XUV-pulse spectral profile, and volume of the NP. (d) As (c) for emission from the Fermi level only (without sampling over the CB).*

The superimposed circles in Figs. 2.8(a), 2.8(b), and 2.8(c) highlight two delay ranges with high detected PE yields. These intervals coincide with particularly high densities and intersections of streaking curves in Figs. 2.7(a) and 2.7(b). The large contrast in electron yield seen in Figs. 2.8(a) and 2.8(b) is reduced in Figs. 2.8(c) and 2.8(d). This is due to the reduction of the detectable electron yield as a result of the surface and transport effects we discussed earlier.

Figure 2.9(a) shows COEs for emission from the surface and Fermi level only, for our full simulation and for emission from the Fermi level only. These COE curves correspond

to the spectra in Figs. 2.8(a), 2.8(c), and 2.8(d), respectively. The COE for emission from the Fermi level only has a larger oscillation amplitude than the COE for emission from the surface and Fermi level only. This is a result of the smaller yield of PEs that are released close to the equator and a consequence of the surface and transport effects.

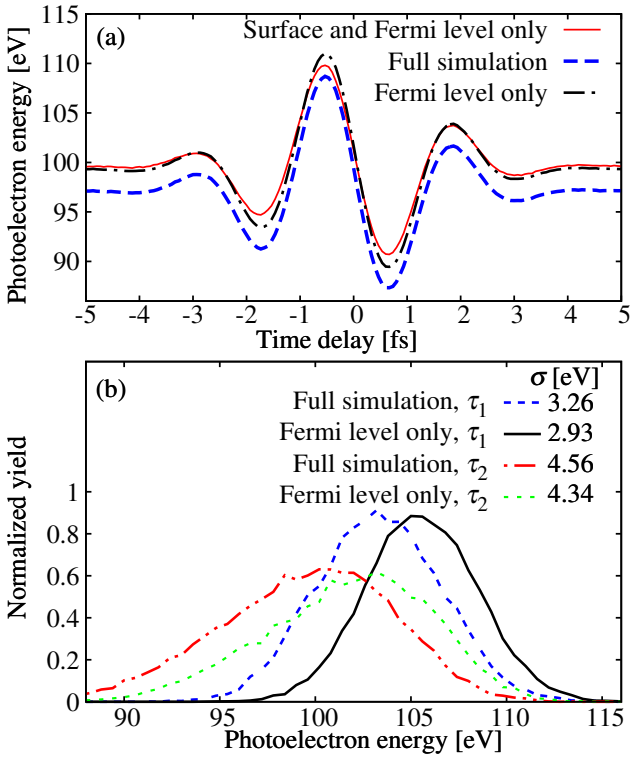

Figure 2.9: *(a) Centers of energy for the spectra in Figs. 2.8(a), 2.8(c), and 2.8(d). (b) Energy profiles of the spectra in Figs. 2.8(c) and 2.8(d) for time delays* $\tau_1 = -933$ *as and* $\tau_2 = 0$ *as and corresponding spectral widths (standard deviations)* σ*.*

Since both, PE current and induced plasmonic field are the strongest at the pole and decrease towards the equator, PEs, on average, acquire larger streaking energy shifts if more electrons are emitted near the pole than near the equator. This is the case when the restriction for emission from the surface only is lifted and emission from the volume is included. The streaking amplitude for emission from the Fermi level only is therefore larger than for emission from the surface only and Fermi level only, as the comparison of the black dash-dotted and solid red COE curves in Fig. 2.9(a) demonstrates. Going from surface to volume emission also induces a small shift of the COE towards lower energies, due to energy loss during electron transport to the surface. For emission from the Fermi level only, this

COE shift amounts to 0.3 eV. One might, in addition, expect a phase shift to be associated with the addition of volume emission. However, we do not observe a noticeable phase shift for the numerical examples discussed in this work. Larger phase shifts might occur in poor conductors with smaller relaxation times τ_{relax}.

In Fig. 2.9(b) we compare the spectral profiles of spectra for two different time delays. As indicated by the superimposed circles in Fig. 2.8 delays $\tau_1 = -933.3$ as and $\tau_2 = 0$ correspond to high and low photoemission yields, respectively. These profiles, and thus the corresponding temporal profiles of the PE wave packet, are different. Allowing for emission from the entire occupied CB (full simulation) leads to a slightly larger energetic width of the spectra. This is quantified in terms of their standard deviations σ in the legend of Fig. 2.9(b).

2.3.3 Plasmonic effects

The effects of the induced plasmonic fields on streaked electron emission are addressed in Fig. 2.10 for nanospheres with radii of 50 nm [left column] and 5 nm [right column] and for streaking-pulse wavelengths of 720 nm [Figs. 2.10(a)-2.10(d)] and 530 nm [Figs. 2.10(e)-2.10(h)]. Figures 2.10(c), 2.10(d), 2.10(g), and 2.10(h) show spectra that are calculated without including the plasmonic field $\vec{E}_{pl}$ given by Eq.(2.4). The comparison of streaked spectra from full simulations, including the plasmonic field in Figs. 2.10(a), 2.10(b), 2.10(e) and 2.10(f), with those that do not include $\vec{E}_{pl}$ for a given nanosphere radius and streaking wavelength reveals a significant increase of the streaking amplitudes due to the plasmonic-field enhancement of the streaking electric field. For both wavelengths the increase in streaking amplitude is larger for 50 nm radius spheres than for 5 nm radius spheres, as expected, since the plasmonic-field enhancement for 50 nm spheres is larger (cf. Fig. 2.3).

For gaseous atomic targets and for laser- and XUV-pulse parameters realized in typical streaking experiments, it is well known that the streaking amplitude is proportional to the wavelength and amplitude of the incident IR field [36]. However, this proportionality does not necessarily apply to nanospheres, as the comparison of Figs. 2.10(a) and 2.10(b) with Figs. 2.10(e) and 2.10(f), respectively, demonstrates. Instead, for both 50 and 5 nm radius

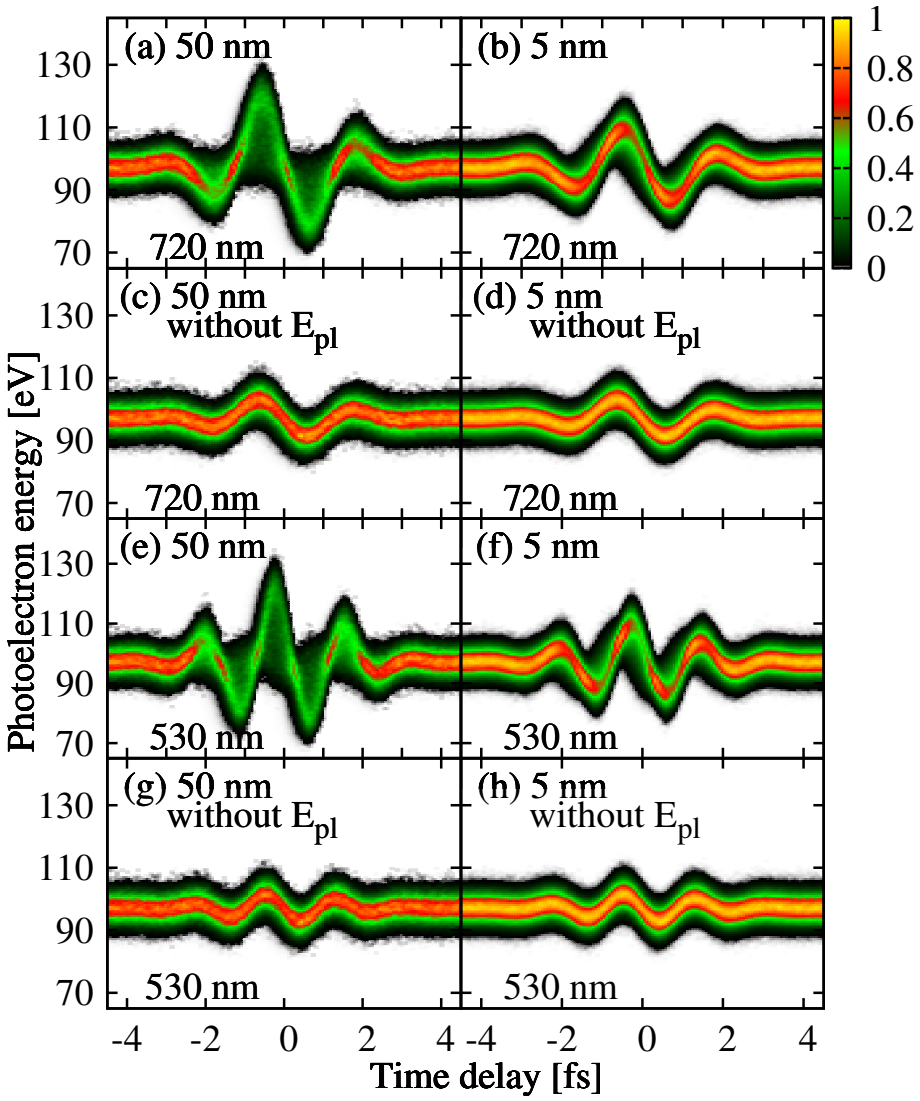

Figure 2.10: *Streaked spectra from Au nanospheres for streaking-pulse wavelengths of (a-d) 720 nm and (e-h) 530 nm, with radii of (a,c,e,g) 50 nm and (b,d,f,h) 5 nm. The spectra are normalized individually to their maximal yields. Results from full simulations that (a,b,e,f) include and (c,d,g,h) do not take into account the plasmonic field $\vec{E}_{pl}$ [Eq.(2.4)].*

nanospheres, the streaking amplitudes for 530 and 720 nm streaking pulses are approximately equal. The deviation from the expected proportionality observed for gaseous atomic targets is another manifestation of plasmonic-field enhancement and due to the streaking-wavelength dependence of the plasmonic field amplitude near the nanosphere surface. Maximal field enhancement occurs near the surface-plasmon-resonance wavelengths which are 560 and 530 nm for 50 and 5 nm Au nanospheres, respectively (Fig. 2.3). Therefore, the lack of a reduced

streaking amplitude at 530 nm streaking wavelength is due to the increased plasmonic-field enhancement at 530 nm. While the approximate cancelation of the expected wavelength dependence by the wavelength-dependent plasmonic-field enhancement is coincidental for the two streaking wavelengths we compared in Fig. 2.10, this comparison shows that, in general, the amplitude of streaked spectra from metallic NPs sensitively depends on their wavelength-dependent dielectric response.

Figure 2.11 shows the COEs corresponding to the spectra in Fig. 2.10. COEs including plasmonic-field enhancement are represented by solid black curves, the ones excluding field enhancement by dash-dotted red curves. In addition to the wavelength and size-dependent streaking amplitudes, the COEs reveal wavelength and size-dependent phase shifts that are induced by the plasmonic field. As shown in a previous quantum-mechanical calculation [11], the scrutiny of COE amplitudes and phase shifts allows the quantitative retrieval of the plasmonic-field enhancement with high accuracy. For a given wavelength, the spectra from the larger nanosphere have larger COE amplitudes. For a given radius, the COE amplitudes for 720 and 530 nm streaking wavelengths are almost equal, consistent with the discussion of Fig. 2.10 above.

2.3.4 Comparison with quantum-mechanical simulations

We have developed a single-active-electron quantum-mechanical model for calculating streaked XUV-photoemission spectra from Au nanospheres [11]. Our simulated spectra show strong amplitude enhancements and phase shifts of the PE streaking trace that match the field enhancement and phase shift of the plasmonically enhanced streaking field. Our quantum-mechanical numerical model thus confirms the possibility of imaging the plasmonic field distribution near nanostructures in streaked electron spectra predicted by our classical-mechanics simulations

For streaked photoemission to occur, the XUV pulse length is assumed to be short compared to the period of the streaking pulse. The streaking pulse intensity assumed in our numerical applications below is too small to ionize the NP, yet causes a measurable energy

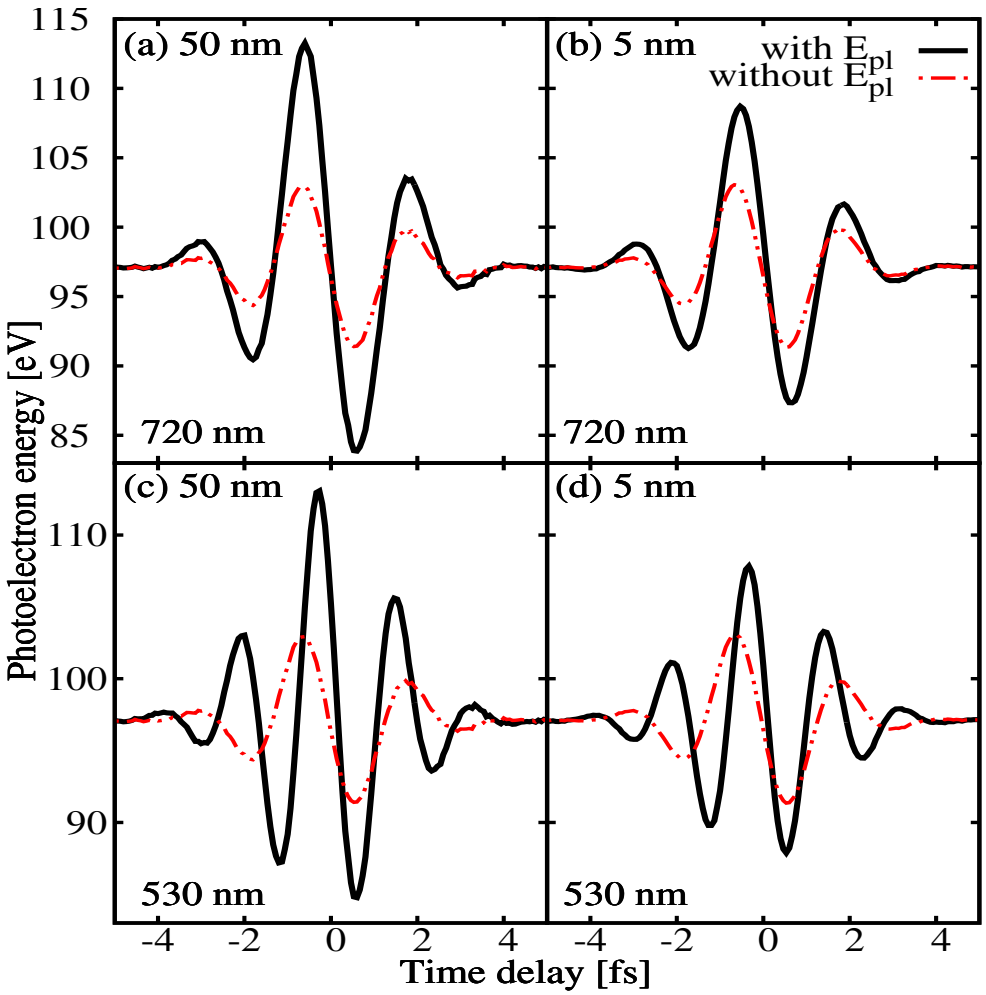

Figure 2.11: *Center-of-energy curves for streaking wavelengths of 720 and 530 nm and nanosphere radii of 50 and 5 nm for the streaked spectra in Fig. 2.10. Results including and excluding nanoplasmonic field enhancement are shown as solid black and dash-dotted red curves, respectively.*

shift of the PE's final energy $\varepsilon_f(\tau)$ as a function of the delay τ of the streaking relative to the XUV pulse. This shift is due to the acceleration of the PE in the total electric field $\vec{E}_{tot}$.

Refraction indices $n(\omega) \approx 1$ at XUV frequencies. The XUV-pulse vector potential (in Coulomb gauge) is given by $\vec{A}_{xuv}(t) = \int_t^\infty dt' \vec{E}_{xuv}(t')$. XUV pulse intensities in typical streaking experiments result in single-XUV photon photoionization [36]. To first order in E_{xuv}, the photoemission amplitude for this process in the velocity gauge as a function of the

final PE momentum $\mathbf{k}_f$ and time delay τ is [43]

$$T_i(\vec{k}_f,\tau) \sim \int dt \int d\vec{r}\; \Psi^{\tau *}_{\vec{k}_f}(\vec{r},t)\; \vec{A}_{xuv}(\vec{r},t)\cdot\vec{p}\;\Psi_i(\vec{r},t). \tag{2.29}$$

We model the initial CB state $\Psi_i(\vec{r},t)$ in (2.29) as a stationary state in a spherical square well of radius a. The depth of the spherical square-well potential is assumed to equal the sum of the work function W and Fermi energy ε_F of bulk Au. We represent the final state as the exponentially damped "Volkov" continuum wave function [89]

$$\Psi^{\tau}_{\vec{k}_f}(\vec{r},t) = \frac{1}{\sqrt{2\pi}} f[l(\vec{r});\lambda_i] e^{i\vec{k}_f\cdot\vec{r}} e^{i\phi^{\tau}_{\vec{k}_f}(\vec{r},t)} \tag{2.30}$$

with the position-dependent generalized Volkov phase $\phi^{\tau}_{\vec{k}_f}(\vec{r},t) = \int_t^{\infty} dt'\; \vec{p}^{\;2}(\vec{r},t')/2$. The damping function $f(l;\lambda) = exp[-l/(2\lambda)]$ describes the fact that PEs which are excited ("born") by the XUV pulse at positions $\vec{r}$ inside the nanosphere and subsequently elastically or inelastically scattered before leaving the NP surface are not registered by the time-of-flight detector. $f(l;\lambda) = exp[-l/(2\lambda)]$ depends on the energy-dependent inelastic mean free path λ_i and the path length $l(\vec{r})$ of PEs inside the nanosphere.

For 80 to 120 eV PEs considered in this work, the IMFP changes by about 2% [86] and is approximated by the constant value $\lambda_i \approx 4.4$ Å, such that only PEs released within approximately 1 nm beneath the surface contribute to the streaked spectra. This relaxes our above assumption of XUV-transparent NPs to a few atomic layers. $l(\vec{r})$ is calculated based on classical PE trajectories $\tilde{\vec{r}}(t')$ with initial positions $\tilde{\vec{r}}(t) = \vec{r}$ at time t and initial momenta

$$\vec{p}(\vec{r},t) = \vec{k}_f + \int_t^{\infty} dt' \vec{E}_{tot}[\tilde{\vec{r}}(t'),t']. \tag{2.31}$$

Assuming that PEs are detected in a very small solid angle around $\vec{k}_f$, the photoionization probability is obtained as a sum over occupied initial states with energies ε_i at and below the Fermi energy

$$P(\varepsilon_f,\tau) = \sum_{i\in occ} |T_i(\vec{k}_f,\tau)|^2. \tag{2.32}$$

We assume photoemission along the XUV polarization direction so that $\vec{k}_f = (0, 0, k_f)$.

Figures 2.12(a) and 2.12(b) show quantum-mechanically calculated streaked photoemission spectra for radius 5 nm gold nanospheres and the two streaking wavelengths from Ref. [11]. These two graphs are generated for the same streaking-field and XUV-pulse parameters as our corresponding classically calculated spectra in Figs. 2.10(b) and 2.10(f). The quantum-mechanical and classical spectra are in reasonable overall agreement, but differ with regard to the spectral distributions along the streaking traces. The quantum-mechanical results show slightly larger variations in the spectrally resolved electron yield as a function of the time delay. The smaller delay-dependent variance in electron yield (streaking amplitude) predicted in our classical simulation is consistent with our XUV-photon-energy-independent modeling of the PE release process, while the quantum-mechanical calculation in Ref. [11] is based on XUV-photon-energy-dependent photoemission amplitudes.

In order to allow for a quantitative comparison, we show in Figs. 2.12(c) and 2.12(d) the COEs for the spectra in Figs. 2.10(b), 2.10(f), 2.12(a), and 2.12(b). Their comparison reveals slightly larger streaking amplitudes for the quantum-mechanical calculation and a phase shift between the classically and quantum-mechanically computed streaking traces. The phase shift and the lower amplitude in the classical model are related to elastic and inelastic collisions of PEs during transport to the surface.

2.4 Conclusion

We developed a classical model to study attosecond streaking spectroscopy from metallic nanospheres [18], extending a previous classical model [39] by sampling over the entire CB and including transport and surface effects. Our numerical results show that these extensions noticeably impact streaking spectra. By varying the radius of the nanosphere, the wavelength of the streaking pulse, and adding or relaxing restrictions to emission from the Fermi level only and from the surface of the NP only, we scrutinized streaked photoemission spectra. In particular, we addressed (i) the influence of the NP's dielectric response on streaked photoemission and (ii) the fidelity with which streaked spectra allow the imag-

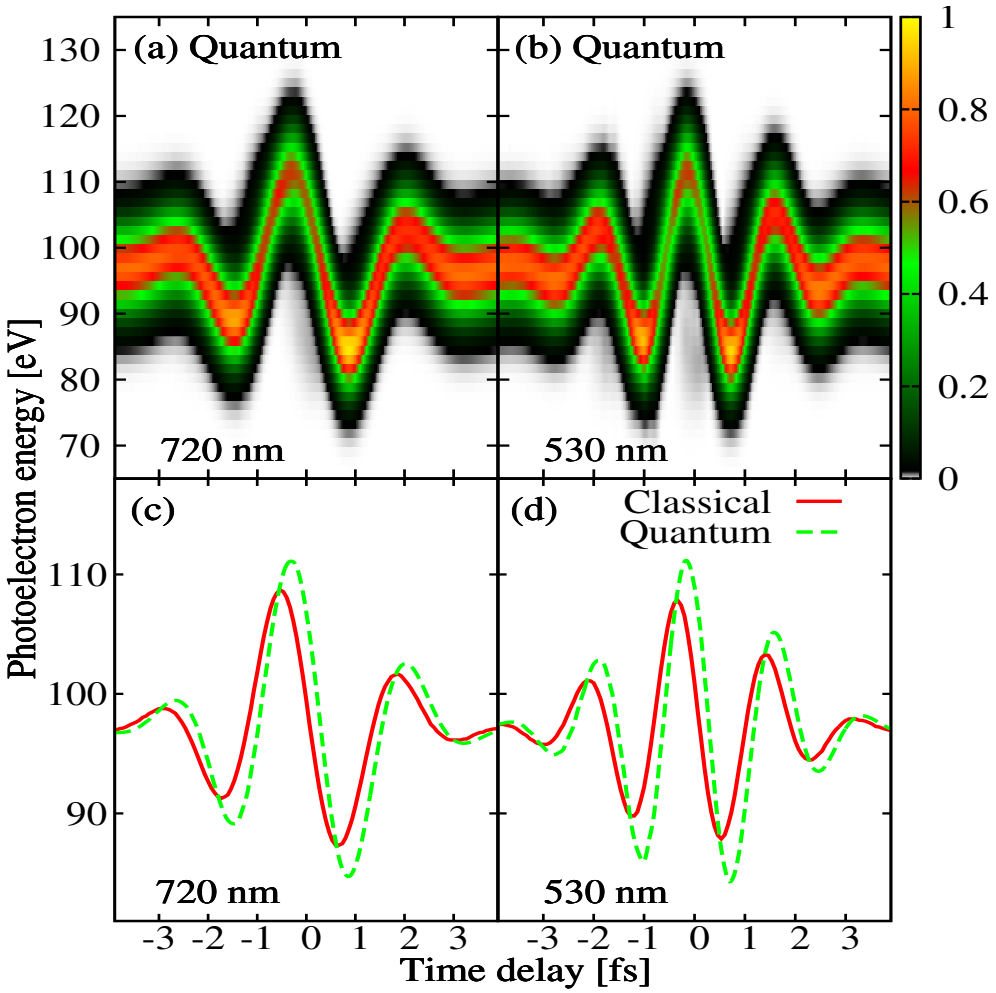

Figure 2.12: *(a,b) Simulated streaked spectra from 5 nm Au nanospheres individually normalized to their maximal yields for streaking-pulse wavelengths of (a) 720 nm and (b) 530 nm according to the quantum-mechanical model of Ref. [11]. (c d) Corresponding centers of energy for the classically simulated spectra in Figs. 2.10(b) and 2.10(f) (solid red line) and the spectra in (a) and (b) (green dashed line).*

ing of the temporal and spatial distribution of the NP's induced plasmonic near-field. The developed classical model is basic and versatile. It can be transferred to different geometries, such as surfaces [90, 91], nanowires [92], nanotips [40], and metal and semiconductor nanostructures [10, 93].

Chapter 3

Spatiotemporal imaging of plasmonic fields near nanoparticles below the diffraction limit

3.1 Introduction

This chapter is an extension of our previous studies on photoemission from plasmonic targets in Chapter 2, in which we investigated the retrieval of the temporal structure of plasmonic near fields from streaked photoemission spectra with sub-fs resolution in time. In this chapter, both the numerical modeling of streaked spectra and the reconstruction of plasmonic near-fields from simulated spectra are based on the classical representation of the PE dynamics. We (i) numerically investigate a novel imaging scheme that adds nm spatial resolution of the plasmonic near field, by means of a suggested modification of the default experimental set up for recording streaked PE spectra [36], and (ii) give a detailed mathematical description of the underlying spatiotemporal reconstruction algorithm. The suggested plasmonic field-retrieval algorithm is applicable for sufficiently long streaking pulses, complementing recently suggested quantum-mechanical field-retrieval scheme that was optimized for ultrashort IR streaking pulses [32].

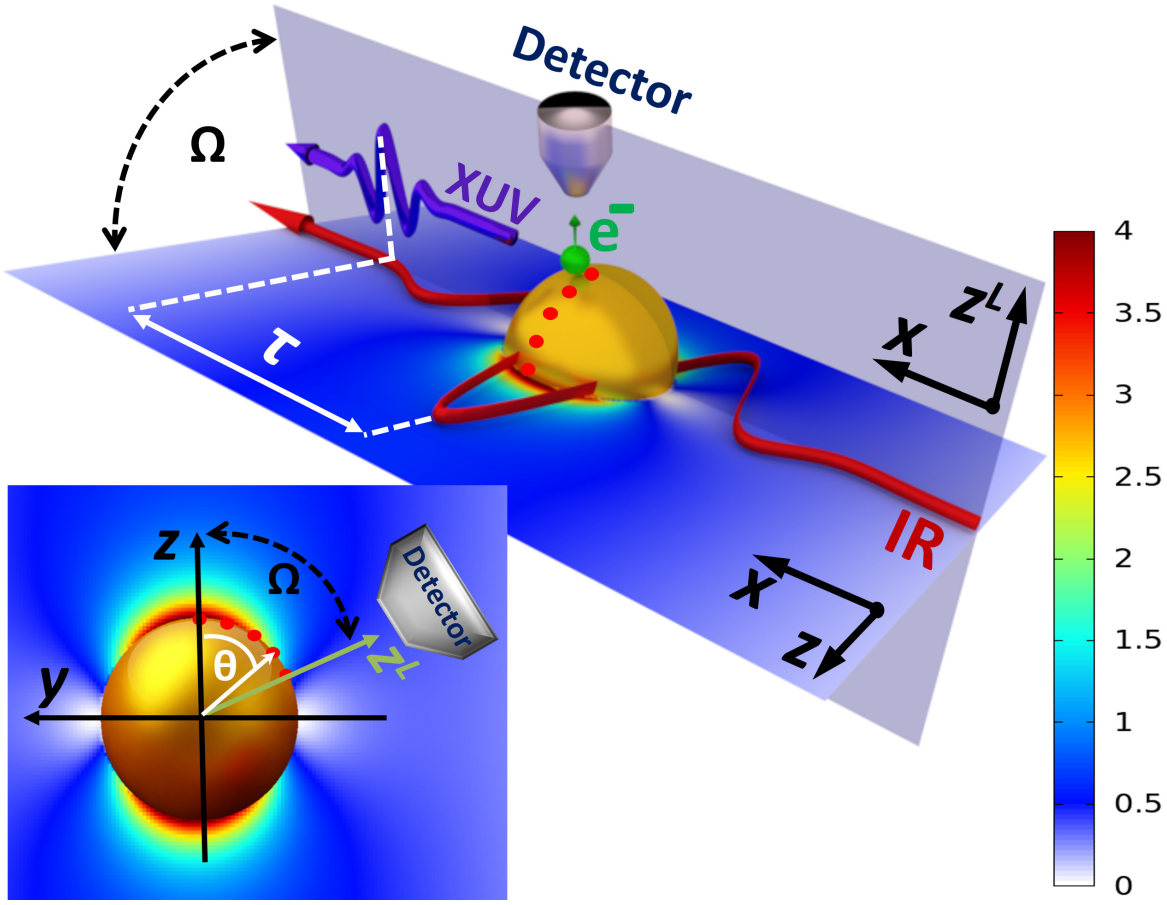

Figure 3.1: *Spatiotemporal nanoplasmonic field imaging near isolated metallic nanospheres employing streaked photoemission spectroscopy. Electrons released by isolated XUV pulses are streaked by delayed nanoplasmonically enhanced visible or IR pulses upon leaving the particles' surface. τ designates the time delay between the phase-coherent streaking and XUV pulses, Ω the variable angle between the XUV and IR electric-field linear polarization directions. Red dots indicate points on the "$x = 0$* longitude*". The size of the target and wavelength of laser pulses are not to scale.*

The proposed scheme for retrieving the plasmonically enhanced streaking electric-field distribution near metal nanospheres with high spatiotemporal resolution consists of recording streaked spectra for variable relative linear polarization directions Ω of the attosecond XUV and streaking pulse (Fig. 3.1). We assume both pulses to propagate along the x-axis of the lab frame (x, y^L, z^L), which is centered in the nanosphere of radius a. The XUV pulse is polarized along the z^L-axis and the streaking pulse along the z-axis of the rotated (x, y, z) reference frame. A stream of isolated spherical gold NPs is injected by an aerodynamic lens focusing [68, 72, 94] into the laser-interaction region. The laser parameters assumed

in our numerical examples correspond to typical parameters used in streaked photoemission experiments with gaseous and solid targets [10, 35, 36, 40, 68, 94]. We can safely neglect the thermal melting of the NPs due to the applied external laser pulses. Melting eventually occurs, however, on a picosecond time scale and therefore long after the few femtoseconds an emitted PE needs to traverse and "probe" the plasmonic near field. Recent experiments measured streaked PE spectra from tapered Au nanowires with 0.1 TW/cm^2 NIR pulses [40] and estimated the damage threshold for Au nanowires at 10 TW/cm^2 for 32 fs pulses and 5 TW/cm^2 for 108 fs pulses [95].

We will show how the variation of Ω allows the reconstruction of the total electric field distribution (sum of induced plasmonic and incident streaking field) (i) along the "$x = 0$ *longitude*" with rotated-frame coordinates $(a, \phi = -\pi/2, \theta = \Omega)$ (indicated as red dots in Fig. 3.1)) and (ii), as a result, over the entire NP surface. Unless stated otherwise, we use atomic units ($\hbar = e = m_e = 1$). To conveniently keep track of relative phases, we employ complex-valued electric fields, their real parts representing physical fields.

3.2 Spatiotemporal attosecond streaking

We assume Gaussian XUV pulses with central energy $\varepsilon_{xuv}^{ctr} = 105$ eV and full temporal width at half intensity maximum (FWHIM) $\Delta t_{xuv} = 287$ as, given by the electric field

$$\vec{E}_{xuv}(\vec{r}, t) = E_{xuv,0} \exp\left[-2 \ln 2 \frac{(t - x/c)^2}{\Delta t_{xuv}^2}\right] \times \exp\left[-i\varepsilon_{xuv}^{ctr}(t - x/c)\right] \hat{e}_{z^L}, \tag{3.1}$$

and streaking pulses with a Gaussian temporal profile

$$\vec{E}_{inc}(\vec{r}, t) = -E_{IR,0} \exp\left[-2 \ln 2 \frac{(t + \tau - x/c)^2}{\Delta t_{IR}^2}\right] \times \exp\left[-i\omega(t + \tau - x/c)\right] \hat{e}_z \tag{3.2}$$

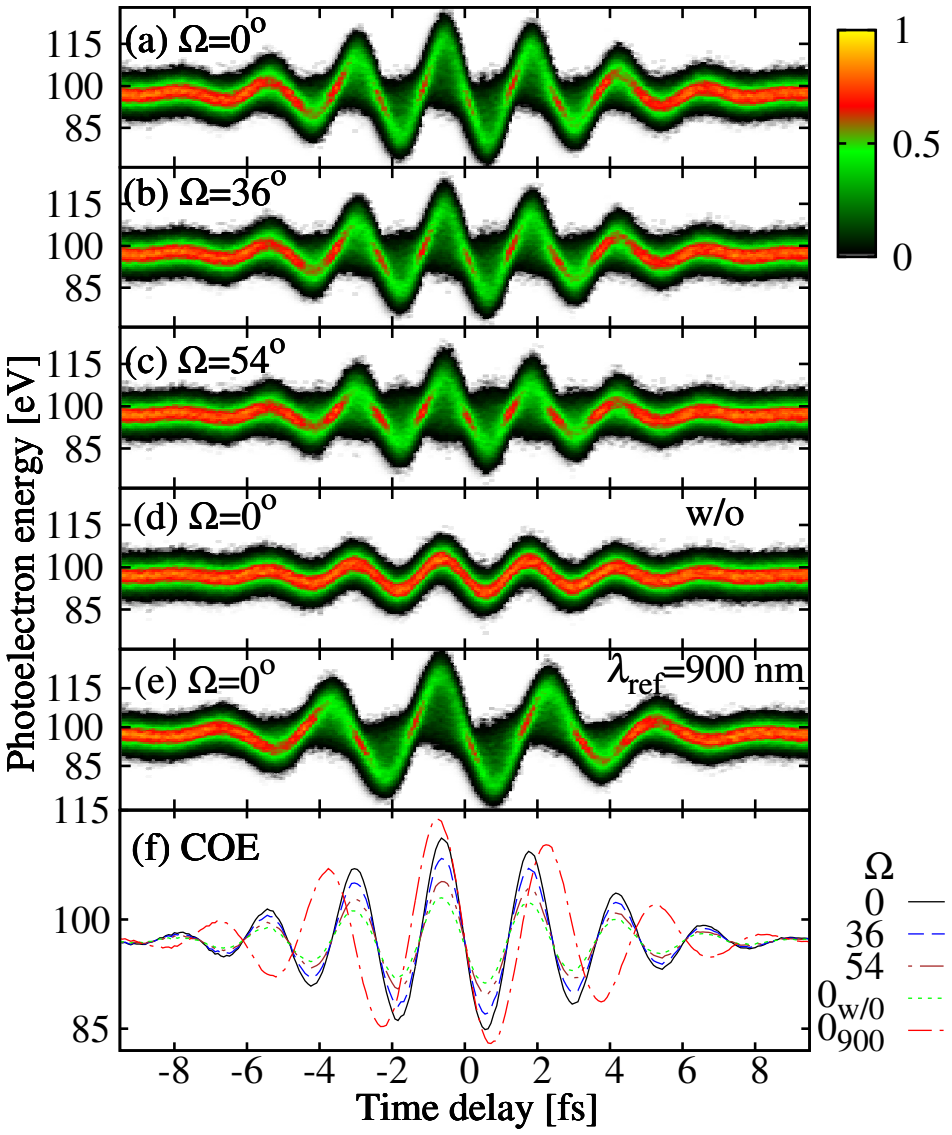

Figure 3.2: *Streaked spectra from 25 nm radius Au nanospheres for different polarization directions* Ω *and* $\lambda = 720$ *nm (a-c) with and (d) without including* $\vec{E}_{pl}$*. (e) Streaked reference spectrum for* $\Omega = 0$ *and* $\lambda = 900$ *nm including* $\vec{E}_{pl}$*. (f) Corresponding centers of energy.*

of pulse length (FWHIM) $\Delta t_{IR} = 5.9$ fs, $\lambda = 2\pi/k = 2\pi c/\omega$ central wavelength, and 10^{12} W/cm^2 peak intensity. c designates the speed of light in vacuum, and the coordinate unit vectors are related as $\hat{e}_z = \sin\Omega\ \hat{e}_{y^L} + \cos\Omega\ \hat{e}_{z^L}$. The time delay τ between the XUV and the streaking pulses is defined to be positive if the streaking pulse precedes the XUV pulse.

The inhomogeneous induced plasmonic field near the surface of sub-streaking-pulse-

wavelength-sized nanospheres is given in the dipole approximation by [79]

$$\vec{E}_{pl}(\vec{r},t) = p(t)\frac{e^{ikr}}{r^3}\left[3(1-ikr)-k^2r^2\right]\sin\theta\cos\theta\ \hat{e}_\rho \\ + p(t)\frac{e^{ikr}}{r^3}\left[k^2r^2\sin^2\theta+(1-ikr)(3\cos^2\theta-1)\right]\ \hat{e}_z, \tag{3.3}$$

where $\hat{e}_\rho$ and $\hat{e}_z$ are unit vectors in cylindrical coordinates. We used the expression for the oscillating induced dipole moment $p(t)$ calculated within Mie theory [70] as given in Ref. [81], such that (3.3) is valid for size parameters $2\pi a/\lambda <\approx 0.6$ (see Chapter 2). The strength of the total electric field near the nanosphere, $\vec{E}_{tot} = \vec{E}_{inc} + \vec{E}_{pl}$, on the nanosphere surface at time $t = 0$ is

$$E_{tot}(a,\phi,\theta,\tau) = \eta_\lambda(a,\theta)E_{inc}(a,\phi,\theta,t=0) \\ \times\exp\left\{-i\left[\sigma_\lambda(a,\theta)+\pi\right]\right\}. \tag{3.4}$$

While E_{tot} does not have cylindrical symmetry, due to the dependence of $x = x_s = a\sin\theta\cos\phi$ in E_{inc} on ϕ, the plasmonic-field enhancement $\eta_\lambda(a,\theta)$ and phase shift $\sigma_\lambda(a,\theta)$ are cylindrically symmetrical [cf., Eq. (3.3)]. According to Eq. (3.4), retrieval of $E_{tot}(a,\phi,\theta,\tau)$ along the $x = 0$ *longitude* therefore allows the reconstruction of the electric-field distribution on the entire NP surface. In the slowly-varying-amplitude approximation, the vector potential of the incident and total electric field follow from (3.2) and (3.4) as

$$A_{inc}(a,\phi,\theta,\tau) \simeq \frac{-i}{\omega}E_{inc}(a,\phi,\theta,t=0) \tag{3.5}$$

and

$$A_{tot}(a,\phi,\theta,\tau) = \eta_\lambda(a,\theta)A_{inc}(a,\phi,\theta,\tau) \\ \times\exp\left[i\sigma_\lambda(a,\theta)\right]. \tag{3.6}$$

We calculated streaked spectra within a classical trajectory model, modeling photoemis-

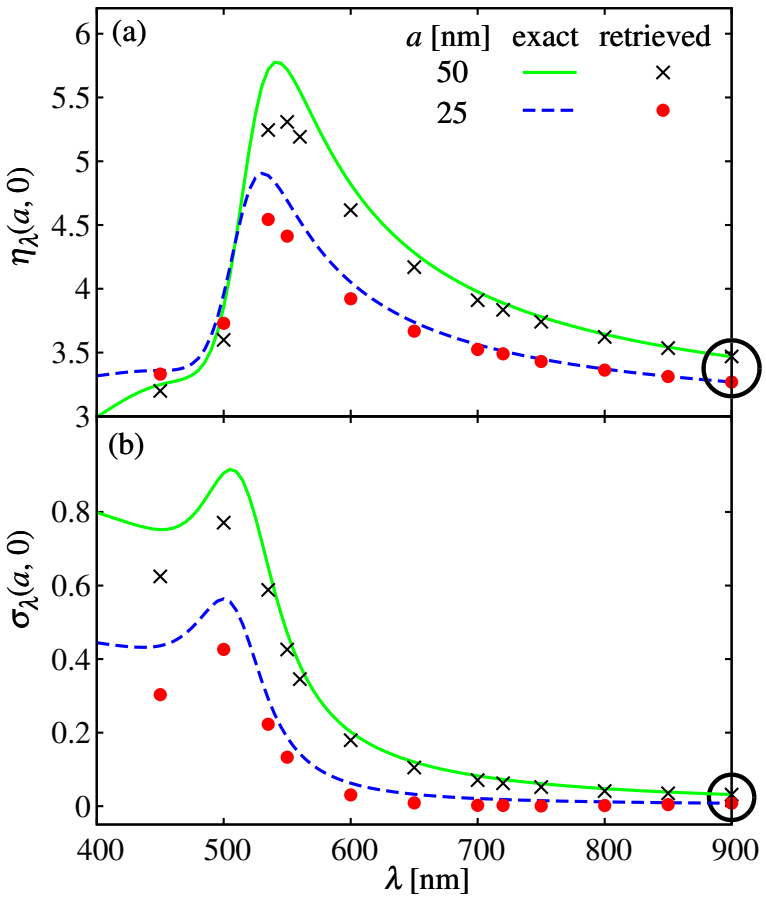

Figure 3.3: *Plasmonic (a) field enhancements and (b) phase shifts at the pole ($\theta = 0$) of gold nanospheres with radii of 25 and 50 nm as a function of the incident streaking-field wavelength λ. The peak intensity of the streaking field is 10^{12} W/cm^2. Exact results (solid and dashed lines) are calculated based on classical electrodynamics according to Eqs. (3.3) and (3.4). Symbols show values retrieved from simulated streaked PE spectra. Values at the reference wavelength of* 900 *nm used for the plasmonic-field retrieval are circled.*

sion in four distinct steps: (i) electronic excitation by the XUV pulse followed by electron (ii) transport to the surface, (iii) escape from the surface, and (iv) propagation outside the nanosphere under the influence of $\vec{E}_{tot}$. The spectra were assembled based on a phenomenological probability distribution over at least six million phase-space points that serve as initial values for Monte-Carlo sampled trajectories. A detailed description of this approach is given in Chapter 2. We numerically simulated streaked spectra for a streaking wavelength of $\lambda = 720$ nm and 10 relative polarizations $0 \leq \Omega \leq \pi/2$. Figures 3.2(a)-3.2(c) show spectra for $\Omega = 0, 36$ and 54° from 25 nm radius nanospheres. A spectrum for $\lambda = 720$ *nm* without

including the plasmonic field is given in Fig. 3.2(d) for $\Omega = 0$. The spectrum for $\lambda = 900$ nm and $\Omega = 0$ is taken as the reference for the plasmonic field retrieval [Fig. 3.2(e)]. The COE of the spectra in Figs. 3.2(a)-3.2(e) are the first moments of the energy distributions in the energy interval [70, 130] eV [Fig. 3.2(f)]. Fitting these numerically calculated COEs to the function

$$\begin{aligned}\varepsilon_\lambda^j(a,\phi,\Omega,\tau) = \varepsilon_0 + C_\lambda^j(a,\Omega)\exp\left[-2\ln 2\frac{(\tau - x_s/c)^2}{\Delta t_{IR}^2}\right] \\ \times \exp\left\{-i\left[\omega(\tau - x_s/c) + \beta_\lambda^j(a,\Omega)\right]\right\}\end{aligned} \tag{3.7}$$

yields the peak COE amplitude $C_\lambda^j(a,\Omega)$ and COE phase shift $\beta_\lambda^j(a,\Omega)$. The COEs oscillate about the unstreaked central photon energy $\varepsilon_0 = \varepsilon_{xuv}^{ctr} - W - 2\varepsilon_f/5$, where $W = 5.1$ eV is the work function [77] and $\varepsilon_f = 5.5$ eV the Fermi energy for bulk gold [77]. The superscript $j = w, w/o$ indicates calculations with/without $\vec{E}_{pl}$.

The simulation of streaked photoemission from atoms in strong-field approximation results in streaking amplitudes $\varepsilon_\lambda^j(a,\phi,\Omega,\tau) - \varepsilon_0$ proportional to $A_{inc}(a,\phi,0,\tau)$ [36]. Guided by this well-know proportionality, we base the plasmonic field reconstruction on the heuristic expression

$$\begin{aligned}\frac{A_{tot}(a,\phi,\Omega,\tau)}{A_{inc}(a,\phi,0,\tau)} = &\frac{\varepsilon_\lambda^w(a,\phi,\Omega,\tau) - \varepsilon_0}{\varepsilon_\lambda^{w/o}(a,\phi,0,\tau) - \varepsilon_0} \\ &\times \alpha(a)\exp\left[i\psi(a)\right],\end{aligned} \tag{3.8}$$

introducing the factor $\alpha(a)$ to correct the attenuation of the plasmonic COE amplitude enhancement $C_\lambda^w(a,\Omega)/C_\lambda^{w/o}(a,0)$ relative to the plasmonic electric field enhancement. This COE enhancement correction accounts for (i) the streaking trace including contributions from PEs emitted over the *entire* surface, thus including regions where the vector potential is significantly different from $A_{tot}(a,\phi,\Omega,\tau)/A_{inc}(a,\phi,0,\tau)$, and (ii) the propagation of PEs in the inhomogeneous plasmonic field resulting in their exposure to an effective electric field that is weaker than the electric field at the surface. Similarly, we allow for a cumulative phase

shift $\psi(a)$ in order to represent (i) the spectral averaging inherent in the calculation of COEs, (ii) scattering of PEs during their transport to the surface (step two in our photoemission model in Chapter 2), (iii) electron escape from the surface (step three), and (iv) subsequent PE propagation in the inhomogeneous plasmonic field (step four). Dividing (3.6) by (3.5) and (3.7) with $j = w$ by (3.7) with $j = w/o$ we obtain

$$\begin{aligned} \eta_\lambda(a,\Omega) &= \frac{C_\lambda^w(a,\Omega)}{C_\lambda^{w/o}(a,0)}\alpha(a) \\ \sigma_\lambda(a,\Omega) &= \beta_\lambda^{w/o}(a,0) - \beta_\lambda^w(a,\Omega) + \psi(a). \end{aligned} \tag{3.9}$$

Justified by our numerical results shown below, we neglect the dependence of $\alpha(a)$ and $\psi(a)$ on the streaking wavelength and Ω. Therefore, comparison with a reference streaking spectrum taken for a streaking wavelength where the plasmonic response is either weak or can be neglected, e.g. $\lambda_{ref} = 900$ nm with polarization direction $\Omega = 0$ [cf., Figs. 3.3 and 3.2(e)], allows us to eliminate the factors $\alpha(a)$ and $\psi(a)$ in (3.9). In this chapter, we assume $\lambda_{ref} = 900$ nm and $\Omega = 0$ for the reference spectrum. The plasmonic-field enhancement and phase shift for the wavelength λ of interest can now be retrieved from streaked spectra as expressed in

$$\begin{aligned} \eta_\lambda(a,\Omega) &\simeq \overbrace{\eta_{\lambda_{ref}}(a,0)}^{a:\ ED-theory} \times \overbrace{\left[\frac{C_{\lambda_{ref}}^{w/o}(a,0)}{C_\lambda^{w/o}(a,0)}\right]}^{b:\ Simulation} \times \overbrace{\left[\frac{C_\lambda^w(a,\Omega)}{C_{\lambda_{ref}}^w(a,0)}\right]}^{c:\ Experiment} \\ \sigma_\lambda(a,\Omega) &\simeq \overbrace{\sigma_{\lambda_{ref}}(a,0)}^{a:\ ED-theory} + \overbrace{\left[\beta_\lambda^{w/o}(a,0) - \beta_{\lambda_{ref}}^{w/o}(a,0)\right]}^{b:\ Simulation} \\ &\quad + \overbrace{\left[\beta_{\lambda_{ref}}^w(a,0) - \beta_\lambda^w(a,\Omega)\right]}^{c:\ Experiment}. \end{aligned} \tag{3.10}$$

The retrieval process thus has three three distinct parts as indicated in the annotations of the above equation:

a: The plasmonic enhancement and phase shift at the reference wavelength are calculated

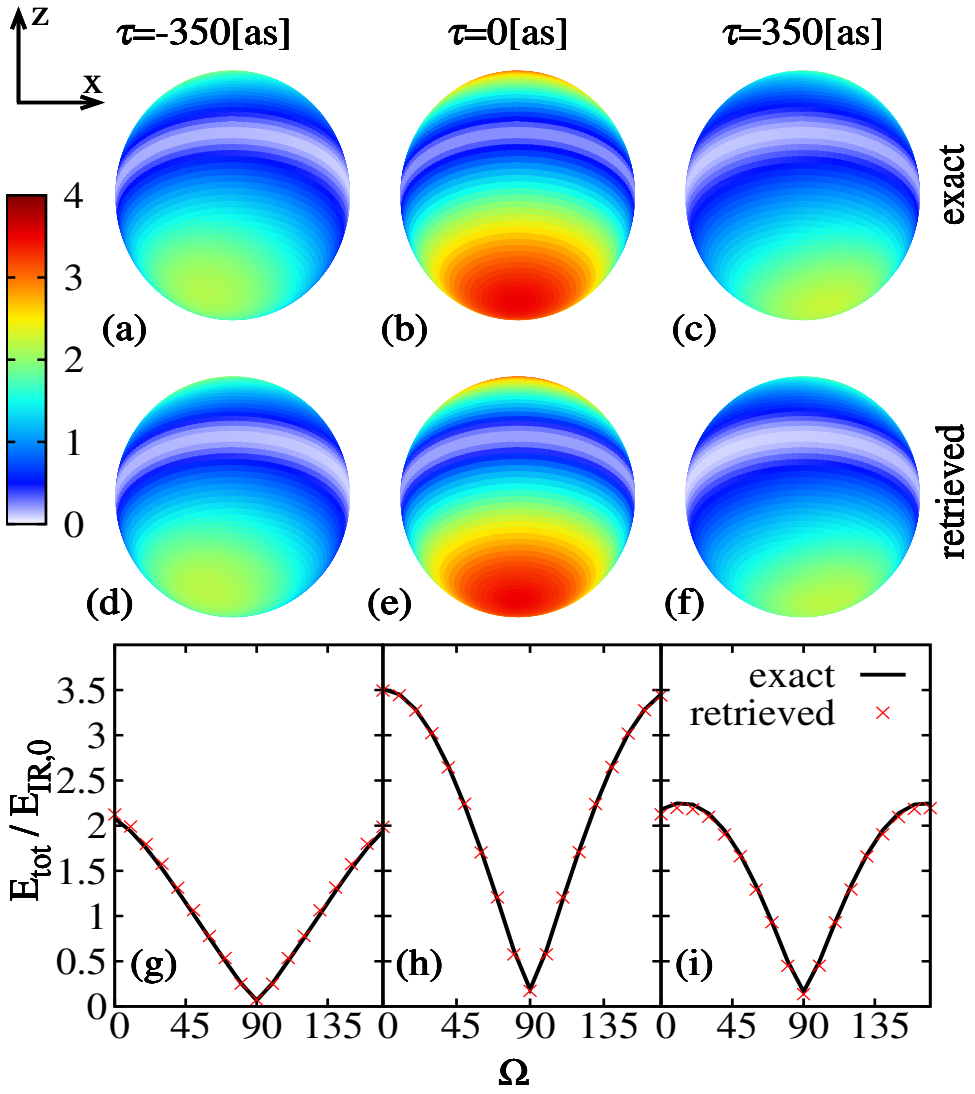

Figure 3.4: *Results for 25 nm Au nanospheres for three XUV-IR pulse delays τ. (a-c) Calculated exact and (d-f) retrieved total electric fields at the surface, normalized to the IR-laser-pulse amplitude $E_{IR,0}$.(g-i) Exact and retrieved total electric field versus the polar angle $\theta = \Omega$ along the* x=0 longitude *($\phi = 0$).*

within classical electrodynamics (ED) [18, 70]. $\sigma_{\lambda_{ref}}(a, 0)$ may be negligible (cf. Fig. 3.3).

b: Not accessible experimentally, the COEs amplitude $C^{w/o}_{\lambda_{ref}}(a, 0)$ and $C^{w/o}_{\lambda}(a, 0)$ and COEs phase shifts $\beta^{w/o}_{\lambda}(a, 0)$ and $\beta^{w/o}_{\lambda_{ref}}(a, 0)$ neglecting the plasmonic response are derived from simulated spectra. Our numerical results show that these functions are size-independent for radii $a \in [5, 50]$ nm and only depend on the incident streaking-pulse wavelengths. To facilitate the field reconstruction at different streaking wavelength, we therefore provide

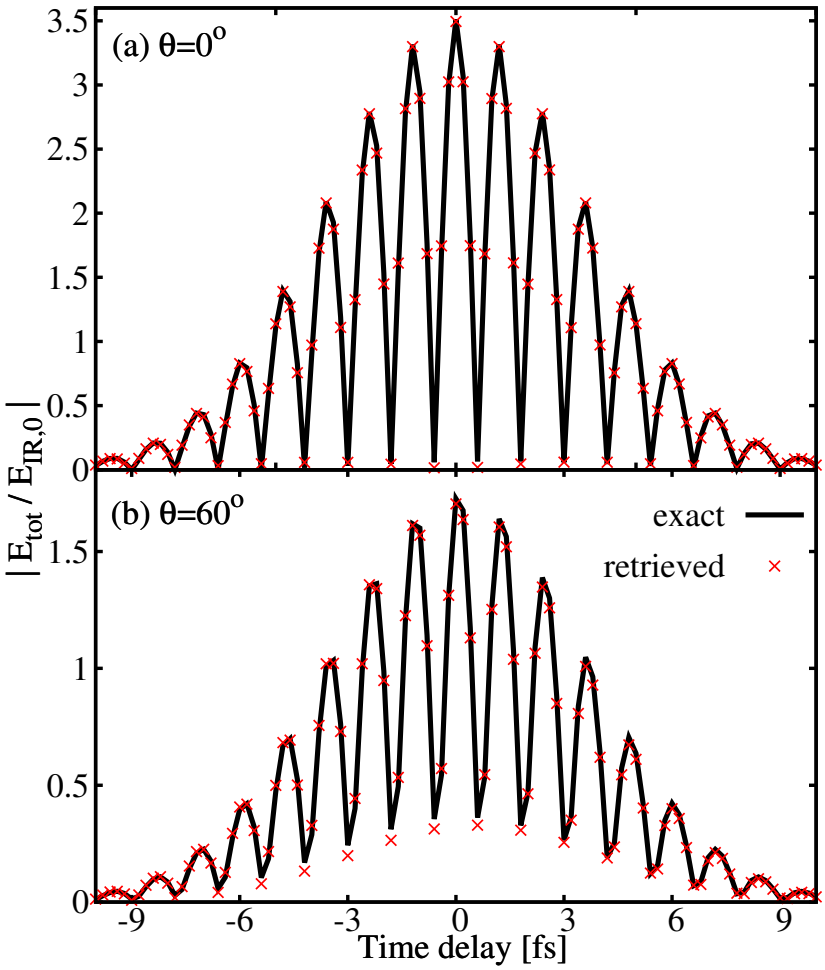

Figure 3.5: *Exact and retrieved total electric near field, normalized to the IR-laser-pulse amplitude $E_{IR,0}$, versus the XUV-IR pulse delays τ for 25 nm Au nanospheres for two different polar angles.*

linear fits, valid for the range $\lambda \in [400,\ 900]$ nm, of the response-free COEs and phase shifts, $C_\lambda^{w/o}(a,0) = \mu_1 + \mu_2\ \lambda$ and $\beta_\lambda^{w/o}(a,0) = \pi/2 + \kappa/\lambda$, with adjusted parameters $\mu_1 = -0.316, \mu_2 = 8.60 \times 10^{-3}$ nm^{-1}, and $\kappa = 87.82$ nm.

c: These factors include COEs and phase shifts deduced from measured spectra at the streaking wavelengths λ and λ_{ref}. $C_\lambda^w(a,\Omega)$, and the phase shifts $\beta_\lambda^w(a,\Omega)$ are measured for several polarization directions Ω.

3.3 Spatiotemporally-resolved surface-electric-field distributions

Figure 3.3 shows retrieved plasmonic-field enhancements $\eta_\lambda(a,0)$ and phase shifts $\sigma_\lambda(a,0)$ for 25 and 50 nm radius nanospheres for 400 nm $< \lambda <$900 nm in fair agreement with our classical ED calculations. Upon retrieving $\eta_\lambda(a,\theta=\Omega)$ and $\sigma_\lambda(a,\theta=\Omega)$ for 11 equally-spaced relative polarizations $\Omega = 0, 9°, 18°, ..., 90°$ from simulated spectra for 25 nm nanospheres and 720 nm streaking wavelength, we reconstructed the total electric fields at different delays at the NP surface according to Eq. (3.4) with nm spatial resolution. The retrieved and exact fields agree (Fig. 3.4).

The spatial resolution of the reconstructed plasmonic near field depends on the number of polarization directions Ω for which spectra are recorded. Based on $N_\Omega = 11$ equally spaced angles $0 \leq \Omega \leq 90°$, the present application of our imaging scheme results in a spatial resolution of the retrieved field of $(1/(N_\Omega - 1) * (\pi/2) * a \approx 4$ nm. The best achievable spatial resolution is limited since streaking traces produced by PEs originating from very nearby points on the surface cannot be distinguished. Figure 3.5 shows excellent agreement between the exact and retrieved total electric fields as functions of the time delay τ for $\phi = 0°$ and two polar emission angles, $\theta = \Omega = 0°, 60°$.

3.4 Conclusion

We propose a practicable (with current technology) spectroscopic scheme based on attosecond streaking spectroscopy which, by scanning the relative linear polarization direction of the XUV and streaking pulse, allows the imaging of plasmonic electric-field distributions on the surface of spherical NPs with nm spatial and sub-fs temporal resolution. The implementation of this method requires the extension of conventional streaking measurements from NPs by allowing for the controlled rotation of the relative linear polarization direction between the XUV and the IR pulses. The suggested imaging scheme has the potential to be generalized to non-spherical NPs by enabling the rotation of the electron detector or by

adding multiple detectors at different directions. For full spatial resolution of the electric near-field distribution, the extension to non-spherical particles may require alignment of the NPs. Further improvements of the suggested imaging scheme may result in a powerful method for the scrutiny of nanoscopic plasmonically enhanced electric-field distributions and electronic dynamics on functional NPs and nanostructured surfaces.

Chapter 4

Strong-field ionization of plasmonic nanoparticles

4.1 Introduction

In the present chapter, we extend the three-step-model for atomic strong-field ionization to metal NPs (Fig. 4.1). We numerically model the release of PEs from the NP surface by intense short laser pulses based on Fowler-Nordheim tunneling rates [96] and subsequently sample over classical PE trajectories. We include and numerically evaluate for 5, 30 and 70 nm diameter gold nanospheres the effects of electronic repulsion, PE attraction by residual positive charges on the NP, multiple PE recollisions with the NP surface, PE recombination with the NP, and nanoplasmonic enhancement of the incident-laser-pulse electric field. We note that due to the strong plasmon response and a large number of free electrons, strong-field PE emission from metal NP requires different model assumptions than strong-field emission from dielectric (insulator) targets. Our approach thus differs from the M^3C model [72] with regard to the description of the NPs' nanoplasmonic response and our implementation of adjusted Fowler-Nordheim tunneling rates [97]. Based on the simulated strong-field-driven PE current density and PE-emission- and recombination-induced dipole moments, we account for electronic excitations in the NP in terms of the electron temperature within

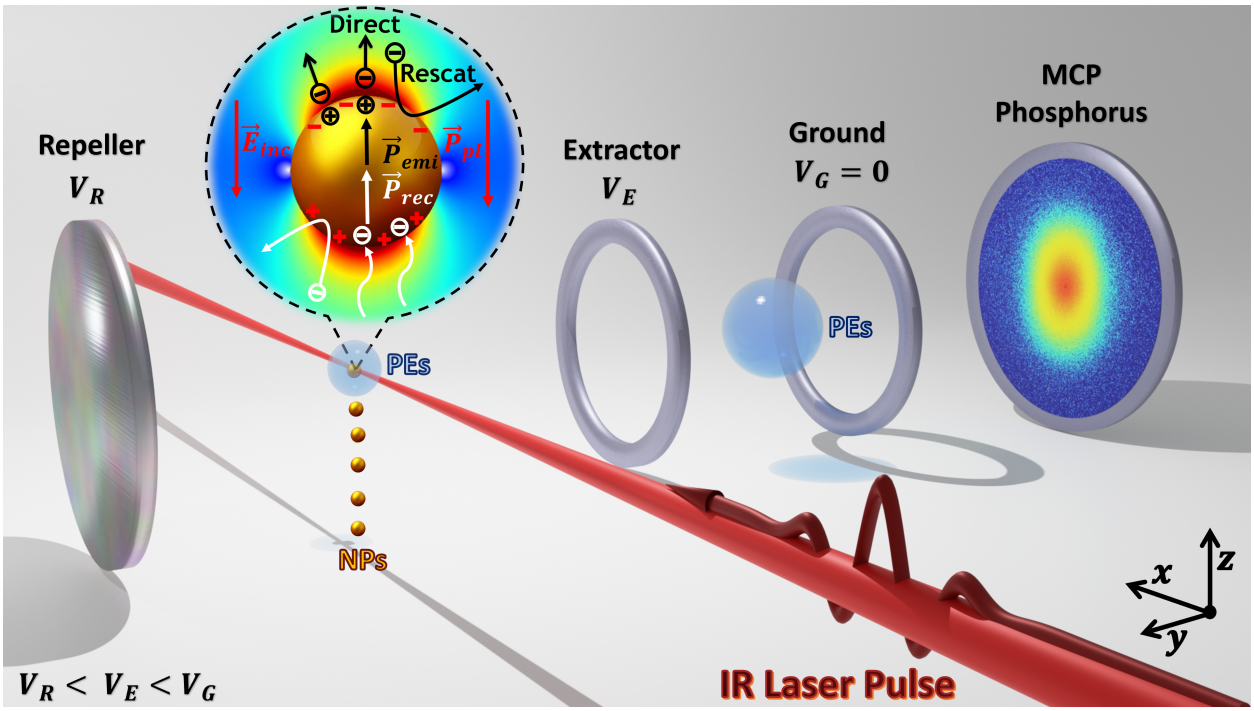

Figure 4.1: *(Color online) Schematic of the velocity-map-imaging (VMI) assembly. The incident IR laser pulse is linearly polarized in the z-direction, propagates in the x-direction, and intersects a beam of metal NPs. V_R, V_E, and V_G are the respective voltages on the PE repeller, extractor, and ground plates, needed to guide PEs to the micro-channel-plate (MCP) with a phosphor screen behind it. . The inset shows processes and fields that occur during the laser-NP interaction, including direct photoemission (Direct), PE rescattering (Rescat) and recombination (rec), the incident laser electric field $\vec{E}_{inc}$, the induced plasmonic polarization $\vec{P}_{pl}$, and the emission ($\vec{P}_{emi}$) and recombination ($\vec{P}_{rec}$) dipoles with their corresponding charge distributions.*

a two-temperature model [98]. We allow for multiple electron-electron interactions while classically propagating a large number of PE trajectories, rather than resorting to a mean-field description.

We organised this chapter as follows. We continue with a description of our numerical model in Sec. 4.2, in which we proceed by explaining our modeling of the (A) nanoplasmonic field induced by the incident laser pulse (Sec. 4.2.1), (B) effect of emitted and recombined PEs on the NPs' evolving dipole moment (Sec. 4.2.2), (C) strong-field ionization and laser-driven current of released PEs (Sec. 4.2.3), and (D) Monte Carlo sampling of PE trajectories (Sec. 4.2.4). In Sec. 4.3 we discuss our numerical results for the strong-field ionization of gold nanospheres, distinguishing the influences of the transient laser-induced plasmonic

field, residual charges, e-e interactions, and PE rescattering and recombination in simulated PEMDs (Sec. 4.3.1). Section 4.3.2 covers different aspects of the photoemission dynamics, such as the accumulation of residual charges, the evolution of the number of propagated and recombined PEs, and the changing ratio of direct versus rescattered PE trajectories. In Secs. 4.3.3 and 4.3.4 we discuss the effects of NP size and laser intensity on photoelectron momentum distributions (PEMDs) and cutoff energies, before representing our conclusions in Sec. 4.4.

4.2 Theory

We investigate PE emission from metallic NPs by IR laser pulses with a Gaussian temporal profile. We assume the laser pulse propagates along the x axis and its electric field is linearly polarized along the z axis,

$$\begin{aligned}\vec{E}_{inc}(\vec{r},t) = \sqrt{I_0}\exp\left[-2\ln 2\frac{(t-x/c)^2}{\tau^2}\right] \\ \times\exp\left[-i\omega(t-x/c)+i\varphi\right]\ \hat{e}_z,\end{aligned} \tag{4.1}$$

where τ is the pulse length at FWHIM, ω the pulse's central frequency, I_0 the peak laser intensity, φ the carrier-envelope phase, and c the speed of light in vacuum (Fig. 4.1). The laser pulse intersects a stream of isolated single NPs that are injected by aerodynamic lens focusing [68, 72, 94, 99]. During the laser-NP interaction, LSPs are excited and induce an inhomogeneous plasmonic field near the NP surface. At the same time, and most significantly at the LSP resonance frequency [100, 101], non-equilibrium high-energy electrons are excited in the metal NP due to strong light absorption, resulting in the population of excited electronic states above the Fermi level (Fig. 4.2). Sufficiently high laser intensities generate multiply ionized NPs [72, 75]. As shown in the sketch of the experimental setup in Fig. 4.1, a fraction of the emitted PEs is guided to the detector and allows the recording of their projected momentum distributions as VMI maps.

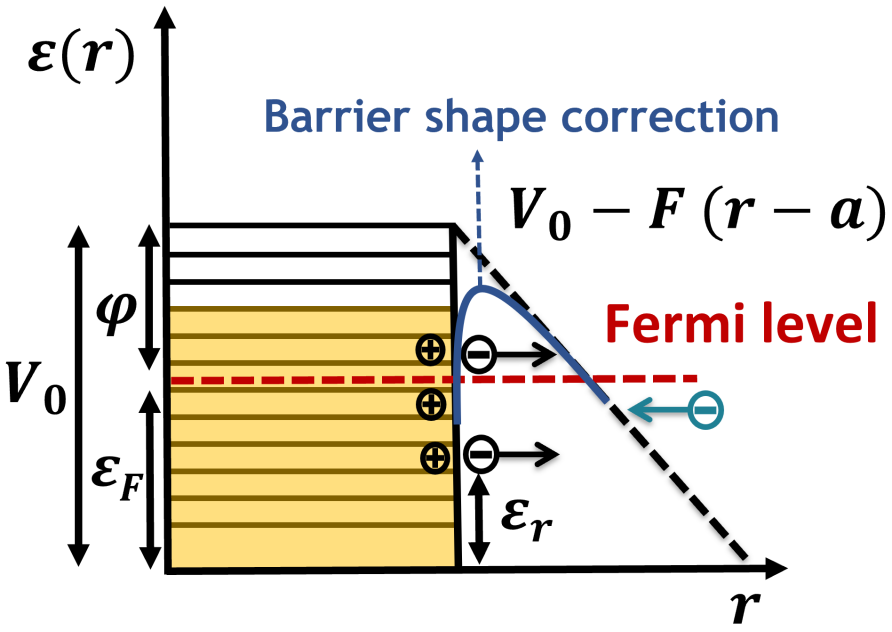

Figure 4.2: *Schematic of the local occupancy of CB states within a small surface element of the metal NP. Emitted and rescattered PEs are indicated by short black and blue horizontal arrows, respectively, together with their corresponding positive residual charges in the NP. A triangular potential barrier is created by the total local electric field $\vec{F}$ on the NP surface under the assumption of a rectangular potential well. This assumption is improved upon by the barrier-shape correction (solid blue line).*

4.2.1 Induced plasmonic field

The incident laser pulse induces a transient dipole in the NP. In the electric dipole approximation, the corresponding plasmonic induced dipole moment $\vec{P}_{pl}(t) = \epsilon_0 \alpha_{Mie}(\omega)\vec{E}_{inc}(\vec{r},t)$ generates the induced plasmonic electric field [79]

$$\begin{aligned}\vec{E}_{pl}(\vec{r},t) = \frac{e^{ikr}}{r}\Big\{k^2\left[\hat{e}_r \times \vec{P}_{pl}(t)\right]\times\hat{e}_r \\ + \left[3\hat{e}_r\left[\hat{e}_r\cdot\vec{P}_{pl}(t)\right] - \vec{P}_{pl}(t)\right](\frac{1}{r^2}-\frac{ik}{r})\Big\},\end{aligned} \tag{4.2}$$

where $k = 2\pi/\lambda = \omega/c$ is the central wave number of the incident pulse. $\alpha_{Mie}(\omega)$ is the complex NP polarizability. We calculate $\alpha_{Mie}(\omega)$ within Mie theory [70], closely following Ref. [81], which restricts the applicability of Eq. (4.2) to size parameters $S = ka \lessapprox 0.6$ for nanospheres of radius a [18]. Since $\vec{E}_{inc}(\vec{r},t)$ and $\vec{P}_{pl}(t)$ are aligned along the $\hat{e}_z$ direction,

Eq. (4.2) can be rewritten as

$$\begin{aligned}\vec{E}_{pl}(\vec{r},t) = P_{pl}(t)\frac{e^{ikr}}{r^3}\left\{\left[3(1-ikr)-k^2r^2\right]\sin\theta\cos\theta\ \hat{e}_\rho\right.\\ \left.+\left[k^2r^2\sin^2\theta+(1-ikr)(3\cos^2\theta-1)\right]\ \hat{e}_z\right\},\end{aligned} \tag{4.3}$$

where θ is the polar angle and $\hat{e}_\rho$ and $\hat{e}_z$ are the usual unit vectors in cylindrical coordinates.

4.2.2 Generalized plasmon dipole moment

Since strong-field ionization of metal NPs by intense fields can lead to a large number of emitted and recombining PEs, the distribution of localized surface charges continuously varies while the NP is exposed to the laser pulse and changes the effective dipole moment of the NP. We account for this change by modifying $\vec{P}_{pl}(t)$ for spherical NPs of radius a. During each laser half cycle the incident laser light augments the density of conduction electrons and holes on opposing hemispheres. The net effect of this periodic charge separation is quantified by the induced dipole moment $\vec{P}_{pl}(t)$ and the local charge density at any position $\vec{r}_s = (a,\theta,\phi)$ on the NP's surface,

$$\sigma_{pl} = \epsilon_0\left[\vec{E}_{inc}(\vec{r}_s,t)+\vec{E}_{pl}(\vec{r}_s,t)\right]\cdot\hat{e}_r \tag{4.4}$$

$$\approx 3\epsilon_0 P_{pl}(t)\cos\theta/a^3, \tag{4.5}$$

where the second, approximate, equation follows from Eqs. (4.1) and (4.3) for size parameters $S << 1$. Thus, σ_{pl} is approximately proportional to $\cos\theta$.

In addition to the directly laser-driven induced plasmonic charge redistribution σ_{pl}, PE emission and rescattering (discussed in detail in Secs. 4.2.3 and 4.2.4 below) modify the surface-charge density of the NPs, decreasing σ_{pl} by

$$\sigma_{emi} = -\frac{n_{emi}(t_{cyc},t)}{2\pi a^2}\cos\theta \tag{4.6}$$

$$\sigma_{rec} = -\frac{n_{rec}(t_{cyc},t)}{2\pi a^2}\cos\theta, \tag{4.7}$$

respectively. The accumulated number of emitted PEs is

$$n_{emi}(t_{cyc}, t) = \left[\int_{t_{cyc}}^{t} dn_{emi} \right], \tag{4.8}$$

where the outer brackets denote rounding to the nearest integer value. The incremental change in the number of emitted electrons, $dn_{emi}(t)$, is given by Eq. (4.11) below. t_{cyc} denotes the initial time of the considered half cycle, starting at $\vec{E}_{inc}(t_{cyc}) = 0$. Similarly, $n_{rec}(t_{cyc}, t)$ is the number of recombined PEs on the positive side of the NP during the same time interval. We assume recombination on the negative side of the NP dipole to be ignorable, since our numerical applications indicate large negative residual charge distributions, leading to dominant rescattering from the NP (Secs. 4.2.4 and 4.3 below). We calculate $n_{rec}(t_{cyc}, t)$ in each half cycle numerically by tracking all PE trajectories.

The electron density decreases on the negative side and the hole density on the positive side of the NP dipole due to intra-cycle PE emission and recombination, respectively. Integration over the corresponding hemispheres of the NP surface results in the time-dependent polarizations

$$\begin{aligned} \vec{P}_{emi}(t) &= \int ds\, \vec{r}_s \sigma_{emi} \\ \vec{P}_{rec}(t) &= \int ds\, \vec{r}_s \sigma_{rec}. \end{aligned} \tag{4.9}$$

These are antiparallel to $\vec{P}_{pl}(t)$ and thus reduce the plasmonic field $\vec{E}_{pl}(\vec{r}, t)$, as illustrated in the inset in Fig. (4.1). Assuming the PE emission- and recombination-induced surface-charge densities instantaneously redistribute, following the $\cos\theta$ proportionality of σ_{pl}, and calculating $\vec{P}_{emi}(t)$ and $\vec{P}_{rec}(t)$ for spherical geometry, we introduce the generalized induced dipole moment

$$\begin{aligned} \vec{P}_G(t) &= \vec{P}_{pl}(t) + \vec{P}_{emi}(t) + \vec{P}_{rec}(t) \\ &= \vec{P}_{pl}(t) - \frac{2}{3} a \left[n_{emi}(t_{cyc}, t) + n_{rec}(t_{cyc}, t) \right] \frac{\vec{E}_{inc}(t)}{E_{inc}(t)}, \end{aligned} \tag{4.10}$$

thereby adding the effects of intra-cycle PE emission and recombination. The above equation

shows that intra-cycle PE emission and recombination reduce the plasmonic field strength, especially for larger NPs. Therefore, any physical process that increases the number of emitted or recombined PEs tends to weaken the effective nanoplasmonic field related to the (generalized) dipole moment $\vec{P}_G(t)$, depending on the characteristics of both, the incident laser-pulse (wavelength, peak intensity, pulse-amplitude and polarization profile) and NP properties (composition, shape, and size). For example, for incident laser-pulse frequencies close to the LSP resonance, we expect the nanoplasmonic field enhancement to increase n_{emi} and n_{rec} and to decrease $\vec{P}_G(t)$.

4.2.3 Strong-field ionization

We describe strong-field ionization from metal NPs within a semi-classical approach including: (1) PE emission based on quantum-mechanical tunneling, (2) PE propagation to the detector by sampling over classical trajectories, and (3) PE rescattering and recombination at the NP surface.

Photoelectron emission

The number of PEs emitted at time t during a small time interval dt,

$$dn_{emi}(t) = \left[dt \int_0^{2\pi} d\phi \int_0^{\pi} d\theta \; a^2 \sin\theta \; J_r(\vec{r}_s, t) \right], \tag{4.11}$$

is given by the radial PE current density at time t at the position $\vec{r}_s = (a, \theta, \phi)$ [96],

$$\begin{aligned} J_r(\vec{r}_s, t) &= \int_{-\infty}^{\infty} d\vec{p} \; g(\vec{p}) \; f_{FD}(\vec{p}) \; W(p_r, F) \; p_r \\ &= \frac{k_B T_e}{2\pi^2} \int_0^{V_0} d\varepsilon_r \; W(\varepsilon_r, F) \ln\left[1 + exp(\frac{\varepsilon_F - \varepsilon_r}{k_B T_e}) \right], \end{aligned} \tag{4.12}$$

in terms of the number of states per unit momentum volume within the Sommerfeld theory of metals $g(\vec{p}) = (4\pi^3)^{-1}$ [77], the Fermi-Dirac distribution function $f_{FD}(\vec{p}) = [\exp((\varepsilon - \varepsilon_F)/k_B T_e) + 1]^{-1}$, and the tunneling ionization rate $W(\varepsilon_r, F)$. $\varepsilon = \varepsilon_r + \varepsilon_{\tan}$ is the conduction-

electron energy, ε_F the Fermi energy, k_B the Boltzmann constant, and T_e the absolute electron temperature. $\varepsilon_r = p_r^2/2$ and $\varepsilon_{\tan}$ are the electron kinetic energies in the radial and tangential directions with respect to the NP surface, respectively. $F = |\vec{F}(\vec{r}_s, t)|$ designates the magnitude of the total electric field at the NP surface,

$$\vec{F}(\vec{r}_s, t) = \vec{E}_{inc}(\vec{r}_s, t) + \vec{E}_{pl}(\vec{r}_s, t) + \vec{F}_{res}(\vec{r}_s, t). \tag{4.13}$$

The number of residual charges at time t is equal to the number of propagated PEs, which is the difference of all emitted PEs $n_{emi}(t_0, t)$ [calculated from Eq. (4.11)] and all recombined PEs $n_{rec}(t_0, t)$ [calculated numerically by tracking all trajectories]. The initial time t_0 is chosen before the onset of the laser pulse. Assuming uniform redistribution of all residual positive charges on the NP surface after each half cycle, the electric field generated by the residual charges at any point $\vec{r}_s = (a, \theta, \phi)$ on the surface of the spherical NP is equal to

$$\vec{F}_{res}(\vec{r}_s, t) = \frac{[n_{emi}(t_0, t) - n_{rec}(t_0, t)]\vec{r}_s}{|\vec{r}_s|^3}. \tag{4.14}$$

Based on Eqs. (4.8) and (4.9), we self-consistently calculate $\vec{F}_{res}(\vec{r}_s, t)$ and $\vec{F}(\vec{r}_s, t)$.

We model tunneling ionization by adapting the PE-emission rate first derived for static electric fields and a triangular potential barrier by Fowler and Nordheim [96] and later modified by Murphy and Good [102],

$$\begin{aligned} W(\varepsilon_r, F_r^+) \cong\, & 4\frac{\sqrt{\varepsilon_r\,(V_0 - \varepsilon_r)}}{V_0} \\ & \times exp\left[-\frac{4\sqrt{2}}{3F_r^+}\nu(f)\,(V_0 - \varepsilon_r)^{\frac{3}{2}}\right], \end{aligned} \tag{4.15}$$

allowing for a parametric dependence on time of the outward pointing radial field component $F_r^+ = \Theta[\vec{F}(\vec{r}_s, t) \cdot \hat{e}_r]\vec{F}(\vec{r}_s, t) \cdot \hat{e}_r$, where Θ designates the Heaviside step function. φ is the work function and $V_0 = \varepsilon_F + \varphi$ the electronic potential at the bottom of the CB relative to the continuum threshold. The numerically calculated barrier-shape-correction factor $\nu(f)$ accounts for the lowering of the surface-potential barrier due to the attractive PE self-image

interaction and significantly increases the PE emission rate [102]. An analytical approximation, valid for sufficiently small scaled electric field strengths $f = F_r^+/(V_0 - \varepsilon_r)^2$, was derived by Forbes [103] as $\nu(f) \approx 1 - f + \frac{1}{6} f \ln(f)$. This approximation is exact for $f = 0, 1$ and has an absolute error below 0.0025 for $0 < f < 1$ [97].

Electron temperature

Before being exposed to the laser pulse, the electron temperature T_e and lattice temperature T_l of the NP are in equilibrium and typically between 100 and 300 K. Effects of these initial temperatures on PE emission from metal NPs are ignorable within the accuracy of current strong-field experiments, due to strong electronic heating by the laser pulse and short laser-pulse duration on the time scale of lattice heating. To account for electronic heating by the incident laser pulse, we calculate T_e in Eq. (4.12) by adapting the two-temperature model originally proposed by Anisimov *et al.* [98]. According to this model, T_e, T_l, and the energy $Q \simeq \sigma_{abs} I_{inc}(t)/V$ absorbed per unit time and volume by a NP of volume $V = (4/3)\pi a^3$ [104] are related by the coupled diffusion equations [105]

$$\begin{aligned} C_e \frac{\partial T_e}{\partial t} &= \nabla \cdot (K_e \nabla T_e) - G\,(T_e - T_l) + Q \\ C_l \frac{\partial T_l}{\partial t} &= \nabla \cdot (K_l \nabla T_l) + G\,(T_e - T_l)\,. \end{aligned} \tag{4.16}$$

$\sigma_{abs} = kIm\,[\alpha_{Mie}(\omega)]$ is the absorption cross sections [106] and $I_{inc}(t)$ the instantaneous incident laser intensity. $C_e = \gamma T_e$, C_l, K_e, K_l, and G are the heat capacities of electrons and lattice, thermal conductivities of electrons and lattice, and electron-phonon coupling constant, respectively. We refer to the electronic heat capacity of an ideal Fermi gas that increases linearly in T_e with proportionality factor γ (heat-capacity constant) [77].

For laser-pulse lengths τ much shorter than typical electron-gas equilibration times (which are of the order of picoseconds [107]), we may neglect electron-lattice couplings. For ultrashort laser pulses, energy transfer from the electron gas to the NP lattice is thus irrelevant during the laser-NP interaction and T_e strongly increases due to laser heating, while the lattice temperature remains constant. In addition, with regard to the small NP size, we

assume the electron thermal conduction term $\nabla \cdot (K_e \nabla T_e)$ can be neglected in Eqs. (4.16), such that T_e is spatially homogeneous. Under these assumptions Eqs. (4.16) simplify to

$$\begin{aligned} \gamma T_e \frac{dT_e}{dt} &= \frac{\sigma_{abs} I_{inc}(t)}{(4/3)\pi a^3} \\ T_e(t_0) &= T_l \end{aligned} \tag{4.17}$$

and can be solved numerically to yield $T_e(t)$. Knowing $T_e(t)$, we solve Eqs. (4.10), (4.11), and (4.12) numerically to find the number of emitted PEs and generalized induced dipole moment $P_G(t)$ at any time.

4.2.4 Sampling over photoelectron trajectories

Based on the radial current density of electrons released at the NP surface by tunneling ionization (4.12), we sample over classical PE trajectories, including the effects of PE repulsion, PE - residual-charge interactions, as well as e-e interactions, rescattering, and recombination.

Photoelectron trajectories

Starting at initial phase-space points $\{(\vec{r}_{i,0}, \vec{v}_{i,0})\}$, we propagate Newton's equations of motion for $n_{pro}(t) = n_{emi}(t_0, t) - n_{rec}(t_0, t)$ PEs. We thus track the correlated PE motion outside the NP (for $r \geq a$) by numerically solving $6\, n_{pro}(t)$ coupled ordinary differential equations

$$\begin{aligned} \frac{d\vec{v}_i}{dt} &= -\vec{F}(\vec{r}_i, t) + \vec{F}_{e-e}(\vec{r}_i, \vec{r}_j) \\ \frac{d\vec{r}_i}{dt} &= \vec{v}_i, \end{aligned} \tag{4.18}$$

where $i = 1 \ldots n_{pro}(t)$. Coulomb interactions between PEs are given by the electric fields

$$\vec{F}_{e-e}(\vec{r}_i, \vec{r}_j) = \frac{1}{2} \sum_{j \neq i}^{n_{pro}(t)} \frac{\vec{r}_i - \vec{r}_j}{|\vec{r}_i - \vec{r}_j|^3}. \tag{4.19}$$

The classical equations of motion (4.18) require the self-consistent determination of $n_{pro}(t)$ (cf. Sec. 4.2.3 above). Due to ongoing PE emission and recombination, the number of propagated PEs $n_{pro}(t)$ changes during the PE propagation. We account for this change by subdividing the propagation time into small time intervals dt, updating $n_{pro}(t)$ at the end of each time interval. We start each emitted electron at the point $(\vec{r}_{i,0}, \vec{v}_{i,0} = 0)$ in phase space and end the time propagation when the PE velocities $\{\vec{v}_i\}$ no longer change within predetermined small limits. Typical propagation times in our numerical applications are of the order of 1 ps.

Photoelectron rescattering and recombination

During the laser-NP interaction, emitted PEs can be driven back to collide with the NP by the laser pulse. Depending on the direction of the total electric field $\vec{F}(\vec{r}_s, t)$ at the surface, we distinguish two cases: (i) PEs that are driven by $\vec{F}(\vec{r}_s, t)$ to the NP surface on the positive hemisphere of the induced dipolar NP charge distribution we assume to either rescatter, if their energies ε (relative to the valence-band bottom) exceed the surface-potential step V_0, or to recombine into bound CB states, if $\varepsilon < V_0$. In contrast, we assume that (ii) PEs that are driven to the NP surface on the negative hemisphere always rescatter.

In our numerical applications in Sec. 4.3 we distinguish and compare specular and diffusive PE rescattering at the NP surface. In either case we conserve the PE kinetic energy. For diffusive rescattering we uniformly randomize the polar and azimuthal scattering angles relative to the surface normal at the impact site $\vec{r}_s$ on the NP surface, thereby modeling rescattering in all accessible directions with equal probability. Our numerical results predict that a considerable number of PEs cannot escape against the attractive Coulomb force of the residual charges. These PEs may undergo several rescattering cycles and are assumed to recombine with the NP (cf., Sec. 4.3.2).

Monte Carlo sampling

We include PE trajectories by Monte Carlo sampling over their initial phase-space points $\{(\vec{r}_{i,0}, \vec{v}_{i,0})\}$ in each time interval $[t, t+dt]$. This sampling is carried out based on the separable model-probability-density function (PDF) $\rho(\vec{r}_{i,0}, \vec{v}_{i,0}, t) = \rho_{pos}(\vec{r}_{i,0}, t)\rho_{vel}(\vec{v}_{i,0}, t)$ that lends relative weights to the trajectories. Assuming zero initial velocities $\vec{v}_{i,0}$ for all PEs at the tunnel exit and in spherical coordinates, the phase-space PDF reduces to the velocity-independent function $\rho_{pos}(\vec{r}_{i,0}, t) = \rho_{pos}(a, \phi_{i,0}, \theta_{i,0}, t)$. We introduce $\rho_{pos}(a, \phi_{i,0}, \theta_{i,0}, t)$ phenomenologically as being proportional to the radial probability current $J_r(\vec{r}_s, t)$ (4.12),

$$\rho_{pos}(a, \phi_{i,0}, \theta_{i,0}, t) \propto J_r(a, \phi_{i,0}, \theta_{i,0}, t), \tag{4.20}$$

where $J_r(a, \phi_{i,0}, \theta_{i,0})$ is approximately proportional to the plasmonically enhanced laser intensity $[(\vec{E}_{inc}(a, \phi_{i,0}, \theta_{i,0}, t) + \vec{E}_{pl}(a, \phi_{i,0}, \theta_{i,0}, t)) \cdot \hat{e}_r]^2$ on the NP surface [96].

For a conducting sphere, tunneling ionization is solely driven by the radial component of the electric field at the surface, $[\vec{E}_{inc}(a, \phi_{i,0}, \theta_{i,0}, t) + \vec{E}_{pl}(a, \phi_{i,0}, \theta_{i,0}, t)] \cdot \hat{e}_r$, which is approximately proportional to $\cos\theta_{i,0}$ for small size parameters S (cf., Sec. 4.2.1). We are thus led to sample over the initial polar angle of the PE with the PDF

$$\rho_{pos}(\vec{r}_{i,0}) \approx \frac{4}{\pi} cos^2\theta_{i,0}, \tag{4.21}$$

over the intervals $[0 : \pi/2]$ or $[\pi/2 : \pi]$, depending on the direction of the electric field in the relevant laser half cycle, and pick the azimuthal PE start angle $\phi_{i,0}$ randomly and uniformly in the interval $[0 : 2\pi]$ [87].

In a typical experimental setup, gaseous targets are exposed to a spatially varying laser intensity. To account for the spatial intensity profile of the laser pulse, we focal-volume average over the laser beam, randomly choosing r' and z' from the Gaussian intensity profile,

$$I_0(r', z') = I_0 \left(\frac{w_0}{w(z')}\right)^2 exp\left(\frac{-2r'^2}{w(z')^2}\right), \tag{4.22}$$

where r' is the radial distance from the central symmetry axis of the laser beam, z' the axial distance from the beam's focus, w_0 the waist radius, and $w(z') = w_0\sqrt{1+(z'/z_R)^2}$, with the Rayleigh range $z_R = \pi w_0^2/\lambda$. In our numerical applications for a given nominal peak intensity I_0, we find converged PEMD by adding the PE yields from up to 5000 randomly sampled peak laser intensities $I_0(r', z')$. The number of intensities required for convergence depends on the NP size and is larger for smaller NPs.

4.3 Numerical results: photoelectron momentum distributions

4.3.1 Influence of the nanoplasmonic field, rescattering, PE residual-charge interactions, and e-e interactions

PEMDs are sensitive to all PE interactions included in our simulation with regard to both strong-field-induced electron emission at the NP surface by tunneling and subsequent PE propagation. The tunneling release of PEs strongly depends on the radial component of the total electric field $\vec{F}$ (4.13). Stronger incident and plasmonic fields increase the number of propagating PEs and PE yield, while PE recombination and the accumulation of positive residual charges on the NP decrease the yield. PE self-image-charge interactions increase the PE-emission rate by lowering the potential barrier (cf., Sec. 4.2.3). In order to track the effects of different electronic interactions on the propagation and rescattering of released PEs, we leave the modeling of the tunneling release of electrons at the NP surface unchanged (for identical laser-pulse parameters), assuming for all calculated VMI maps identical tunnel-ionization rates (4.15). The comparison of simulations in which we selectively include and exclude specific PE interactions during the PE propagation and rescattering only, allows us to quantify their specific effects on PEMDs.

Figure 4.3 shows simulated PE VMI maps for gold nanospheres with 30 nm diameter for the experimental setup depicted in Fig. 4.1. The VMI maps are projections of the PEMD

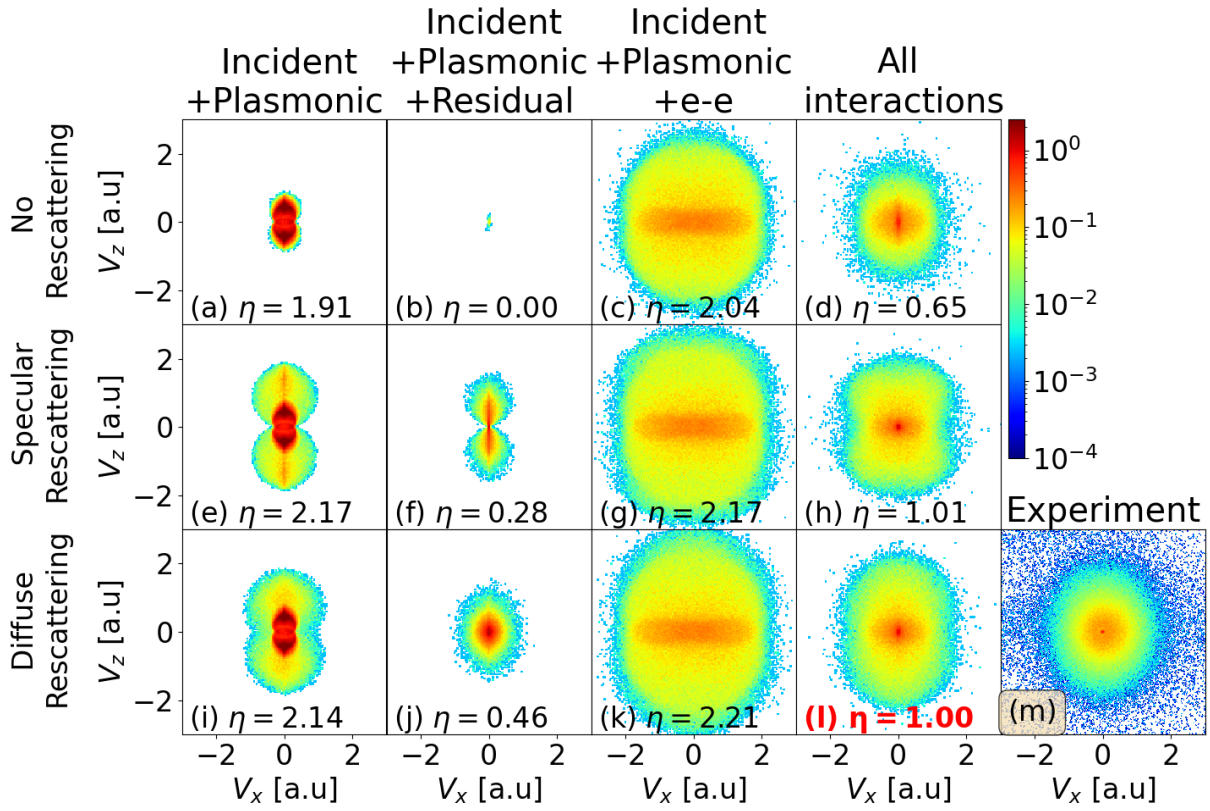

Figure 4.3: *PE VMI maps simulated for* 30 *nm diameter gold nanospheres excluding PE rescattering (first row) and including either specular (second row) or diffuse PE rescattering (third row) for incident* 780 *nm laser pulses with a pulse length of* 25 *fs (FWHIM) and* 8.0×10^{12} *W/cm*^{2} *peak intensity. Columns one through three show simulations where only selected PE interactions are included. In column one only the incident laser and plasmon fields ($\vec{E}_{inc}$ and $\vec{E}_{pl}$) are included. Column two adds PE interactions with residual positive charges ($\vec{F}_{res}$). The VMI maps in column three include $\vec{E}_{inc}$, $\vec{E}_{pl}$, and repulsive PE Coulomb interactions ($\vec{F}_{e-e}$). Simulations including all PE interaction are shown in column four. η gives integrated PE yields normalized to the integrated yield from the VMI map in graph (l). The last figure in the third row (m) shows the corresponding experimental VMI map for* 30 *nm diameter gold nanospheres for the same laser characteristics parameters as the simulation ones.*

on the x-z plane of the MCP detector and show the projected PE yields as functions of the PE asymptotic velocities, v_x and v_z, along the laser propagation and laser polarization directions. The incident Gaussian laser pulses have a pulse length of $\tau = 25$ fs FWHIM (10 cycles), central frequency $\omega = 384.4$ THz (corresponding to the wavelength $\lambda = 780$ nm), and peak intensity of $I_0 = 8.0 \times 10^{12}$ W/cm^2. We represent the electronic structure of the NPs in terms of the surface-potential step $V_0 = \varepsilon_F + \varphi$ with the work function $\varphi = 5.1$ eV

and Fermi energy $\varepsilon_F = 8.0$ eV for bulk gold [78], initial electron and lattice temperatures $T_e(t_0) = 300$ K, and heat-capacity constant $\gamma = 66J/(m^3K^2)$ [77].

The first, second, and third row in Fig. 4.3 include simulation results obtained under the assumption of no PE reflection at the NP surface, specular reflection, and diffuse reflection, respectively, as described in Sec. 4.2.4. For the simulations without rescattering, PEs that are driven back to the NP surface are assumed to recombine. The first column in this figure shows simulated VMI maps for which the effects of the electric fields of residual charges ($\vec{F}_{res}$) and PE-PE Coulomb interactions ($\vec{F}_{e-e}$) are neglected during the PE propagation. In the second column $\vec{F}_{e-e}$ is switched off, while $\vec{F}_{res}$ is disregarded in the third column. In column four all PE interactions are included. To allow for a qualitative and quantitative comparison, we normalized the yields in all graphs to the largest yield in Fig. 4.3(l) and display the normalized integrated yield factor η in each graph. We calculate this factor as the v_x- and v_z-integrated yields from the VMI maps in Figs. 4.3(a) - 4.3(k) divided by the integrated yield of Fig. 4.3(l). We choose Fig. 4.3(l) as a reference since it displays our most realistic and accurate simulation results. The comparison of the VMI maps in Fig. 4.3 allows us to assess the influence of the following PE interactions on VMI maps:

Rescattering

The VMI maps in the first row of Fig. 4.3, calculated without allowing for PE rescattering, overemphasize PE recombination. The corresponding enhanced accumulation of positive residual charges on the NP decreases PE yield. Indeed, the PE yields in the first row are consistently smaller than for simulations that allow for PE rescattering (second and third row). The reduction of the PE yield is most pronounced in the second column and easily recognized by much smaller relative yields η in Fig. 4.3(b). It remains relevant for simulations that include all PE interactions, shown in column four, where the suppression of rescattering and ensuing enhanced recombination reduces the relative yield to 65% in row one. While still clearly noticeable, this reduction in PE yield upon disabling rescattering is less visible in simulations that exclude residual-charge interactions in column three. In this case, PE

rescattering still occurs for the simulation in rows two and three, but is much less likely, due to the absence of attractive PE - residual-charge interactions. At the same time, the added PE Coulomb repulsion strongly inflates the yields in all rows of column three.

Plasmonic-field interactions

The simulated VMI maps in the first column of Fig. 4.3 are calculated under the assumption that released electrons solely interact with the incident laser and induced plasmonic field while propagating to the detector. These PE distributions are aligned with the laser-polarization direction and have a dipole-like appearance, owing to the dipole character transferred from the induced plasmonic field and tunneling ionization.

Since Fig. 4.3(a) excludes rescattering, its comparison with Figs. 4.3(e) and 4.3(i) reveals that directly emitted PEs dominate the low-energy part of the photoemission spectra. Rescattered electrons, in contrast, can gain additional energy from the laser and induced plasmonic fields and establish the higher-energy part of the PE spectrum. Rescattering boosting PE energies is a well-understood phenomenon in strong-field ionization. For gaseous atomic targets, elastically rescattered PEs reach kinetic energies up to $10\,U_p(I_0)$ [50–53] and significantly larger energies for dielectric NPs (SiO_2) [10, 72, 75]. By comparing the yield factors η in the first column, we find that approximately 89% of the detected PEs are directly emitted, while 11% have rescattered at the NP surface at least once.

Residual-charge interactions

The second column of Fig. 4.3 displays the effects of PE residual-charge interactions on VMI maps. These simulation results are obtained by solving Newton's equations (4.18) for the propagation of released electrons under the influence of the electric fields of the incident laser, $\vec{E}_{inc}$ (4.1), induced plasmonic dipole, $\vec{E}_{pl}$ (4.3), and residual charges $\vec{F}_{res}$ (4.14). e-e interaction $\vec{F}_{e-e}$ (4.19) is neglected.

The long-range Coulomb attraction of accumulating positive residual charges decelerates both direct and rescattered PEs. It increases the number of PEs that recombine with or

rescatter off the NP. Therefore, residual charge interactions tend to decrease the net PE yield and cutoff energy. This is clearly demonstrated by comparing the VMI maps and relative PE yields η in the second column against the results shown in the first column. This comparison also reveals that the strong PE - residual-charge attraction practically eliminates direct PE emission [Fig. 4.3(b)]. Without being rescattered, directly emitted PEs cannot accumulate enough energy in the laser and plasmonic fields to overcome the residual-charge attraction.

Allowing for specular PE reflection in Fig. 4.3(f) and diffuse rescattering in Fig. 4.3(j), some of the rescattered PEs gain enough energy from the laser pulse to beat the residual-charge attraction and escape to the PE detector. While $\vec{F}_{res}$ preserves the dipolar PE distribution for specular rescattering in Fig. 4.3(f), the dipole-like character of the VMI map disappears for diffuse rescattering in Fig. 4.3(j). The significantly larger total yield η for diffuse rescattering, as compared to specular rescattering, is consistent with PEs that are rescattered to smaller angles than the incident angle (relative to the surface normal at the turning point of the scattered trajectory on the NP) being more likely to escape. Note that this effect is absent if residual-charge interactions are neglected [cf., Figs. 4.3(e) and 4.3(i)], consistent with $\vec{F}_{res}$ promoting rescattering.

Electron-electron coulomb interactions

In the third column of Fig. 4.3, we investigate the effects of e-e interaction on VMI maps. This column shows results obtained by solving Newton's equations (4.18) for the motion of released electrons under the influence of the electric fields of the incident laser, $\vec{E}_{inc}$ (4.1), induced plasmonic dipole, $\vec{E}_{pl}$ (4.3), and PE repulsion $\vec{F}_{e-e}$ (4.19). In this column, the electric field of the residual charges $\vec{F}_{res}$ (4.14) is neglected.

The addition of $\vec{F}_{e-e}$ introduces Coulomb energy into the system of released electrons, accelerating a large fraction of PEs to significantly higher final (detectable) kinetic energies. Correspondingly $\vec{F}_{e-e}$ decreases the number of rescattering and recombination events (compare column three with columns one and two of Fig. 4.3). This results in distinctly larger PE cutoff energies as compared to VMI maps calculated without including e-e interactions

in columns one and two of Fig. 4.3. The larger cutoff energy is solely related to strong e-e interactions and not to rescattering, since adding $\vec{F}_{e-e}$ almost eliminates the effect of PE rescattering. This is seen in the lack of contrast between the VMI maps and PE detection yields η in column three. In opposition to the results excluding $\vec{F}_{e-e}$ in columns one and two, disallowing rescattering in Fig. 4.3(c) reduces the integrated yield η by only 5% and 7%, as compared to specular and diffuse rescattering in Fig. 4.3(g) and 4.3(k), respectively. Thus, in comparison with the VMI maps in column two, the inclusion of e-e interactions in column three strongly enhances direct emission (to, respectively, 95% with respect to specular rescattering and 93% with respect to diffuse rescattering) to the detriment of PE rescattering. The slightly larger yield for diffuse, as compared to specular rescattering, is consistent with smaller scattering angles (relative to the local surface normal) making PE recombination less likely. The large increase of the PE cutoff energy in Fig. 4.3(c) in comparison with Fig. 4.3(a) indicates that PE Coulomb repulsion dominates PE interactions with the incident laser and induced plasmonic fields in shaping the VMI maps.

Apart from the increased cutoff energy, the Coulomb repulsion between PEs changes the shape of the elongated and dipole-like PEMDs shown without including $\vec{F}_{e-e}$ in column one and two of Fig. 4.3. $\vec{F}_{e-e}$ renders the highest-energy part of the PE spectrum approximately isotropic, regardless of rescattering and recombination events, and leads to dominantly transverse PE emission. The enhanced transverse PE emission is visible as a horizontal structure confined by transverse PE velocities $|v_x| < 2$ a.u. and longitudinal velocities $|v_z|$ below approximately 0.5 a.u.. We interpret this structure as due to the absence of the attractive residual-charge interactions and dominant direct emission in the simulated VMI maps shown in the third column of Fig. 4.3. This horizontal structure is consistent with the rapid release of electrons near the poles of the NP (along the laser polarization direction), where strong-field tunneling ionization most likely occurs. During each laser half cycle this forms an initially spatially compact ensemble of electrons in the x-y plane near a NP pole with a narrow extension along the laser polarization direction (z axis) that is spread laterally by dominant PE-PE Coulomb repulsion.

All interactions effect

Simulated VMI maps and relative PE yields η including all PE interactions, i.e., $\vec{E}_{inc}$ (4.1), $\vec{E}_{pl}$ (4.3), $\vec{F}_{e-e}$ (4.19), and $\vec{F}_{res}$ (4.14), are shown in the fourth column of Fig. 4.3. As expected, and easily seen in comparison with the VMI maps in the third column, inclusion of the attractive residual-charge interactions decreases the PE cutoff energy and weakens the transverse emission at lower PE energies. The comparison of the VMI maps in columns one and four of Fig. 4.3 reveals that the combined effect of $\vec{F}_{e-e}$ and $\vec{F}_{res}$ considerably increases the final energy of directly emitted electrons, while decreasing the direct-emission yield from about 88% to less than 65%. This can be understood in terms of directly emitted electrons, on average, moving slower and closer to the NP than rescattered PEs, making directly emitted electrons more likely to recombine and more susceptible to energy gain due to e-e interactions. Due to strong e-e interactions, direct photoemission from metal NPs can reach cutoff energies exceeding 100 $U_p(I_0)$, which is about 75% the cutoff energy of rescattered PEs [cf., Fig. 4.3(d) and Fig. 4.3(l)].

Fig. 4.3(m) shows the experimental VMI map for 30 nm diameter gold nanospheres. By considering the yield, cutoff energy, and the isotropic shape of PEMDs, Fig. 4.3(l) is our best simulation result which matches very well with the experiment. We can exclude Fig. 4.3(h) (the one with specular rescattering) because it preserves the dipole-like shape distribution and Fig. 4.3(d) (the one with no PE rescattering) because of smaller cutoff energy and PE yield.

To summarize the influence of different PE interactions, we first note that the linearly polarized incident laser and induced plasmonic electric field imprint their dipole character on the PEMDs in the absence of e-e interactions and diffuse rescattering. The inclusion of e-e interactions and diffuse rescattering removes the dipolar character of the VMI maps and results in more isotropic PEMDs. For metal NPs, attractive residual-charge interactions are thus much less influential than e-e interactions in shaping PEMDs and determining PE cutoff energies. In addition, we note that e-e interactions significantly contribute to the high-energy part of the PE spectra, even for direct emission, resulting in cutoff energies way

above the conventional $2\,U_P(I_0)$ limit for the atomic targets [51]. The increase of the PE cutoff energies due to rescattering, and as compared to direct emission, is less pronounced for metal NPs than for gaseous atomic targets.

4.3.2 Photoemission dynamics

The VMI maps in Fig. 4.3 are the end results of the intertwined evolution of electron emission, recombination, and competing electronic and laser-electron interactions. To examine the dynamics of these interactions, we show in Fig. 4.4 the incremental change per laser half cycle j of the numbers of emitted, n_{emi}, and recombined, n_{rec}, PEs as a function of time [cf., Eq. (4.8) and subsequent text]. These numbers are extracted in half-laser-cycle intervals during the laser-NP interaction from simulations for the same combinations of PE interactions distinguished in the four columns of Fig. 4.3. Electron numbers shown in Figs. 4.4(a) and 4.5(a) are calculated without allowing for PE rescattering (corresponding to the first row of VMI maps in Fig. 4.3) and including diffuse rescattering (corresponding to the third row in Fig. 4.3). Corresponding electron-number evolutions for simulations including specular rescattering are in close agreement with the results in Figs. 4.4(b) and 4.5(b) and are not displayed. According to Eq. (4.8) the incremental changes of these PE numbers during a given half cycle j are

$$\Delta n^{\kappa}_{emi,j} = n^{\kappa}_{emi}(t_{cyc,j}, t_{cyc,j-1}) \tag{4.23}$$

$$\Delta n^{\kappa}_{rec,j} = n^{\kappa}_{rec}(t_{cyc,j}, t_{cyc,j-1}),\ \kappa = pl, res, e-e. \tag{4.24}$$

The superscripts refer to calculations in which only PE interactions with the laser and induced plasmonic electric fields are included [$\kappa = pl$, corresponding to the VMI maps in the first column in Fig. 4.3] and to simulations that add either PE - residual-charge interactions [$\kappa = res$, corresponding to the second column in Fig. 4.3] or PE Coulomb repulsion [$\kappa = e{-}e$, corresponding to the third column Fig. 4.3]. Full simulations including all PE interactions are given the superscript $\kappa = all$ and correspond to the fourth column of Fig. 4.3. All

electron numbers are shown as colored markers that are connected by solid and dotted lines to guide the eye. The numbers of propagated PEs for the same set of simulations as in Fig. 4.4 are shown in Fig. 4.5.

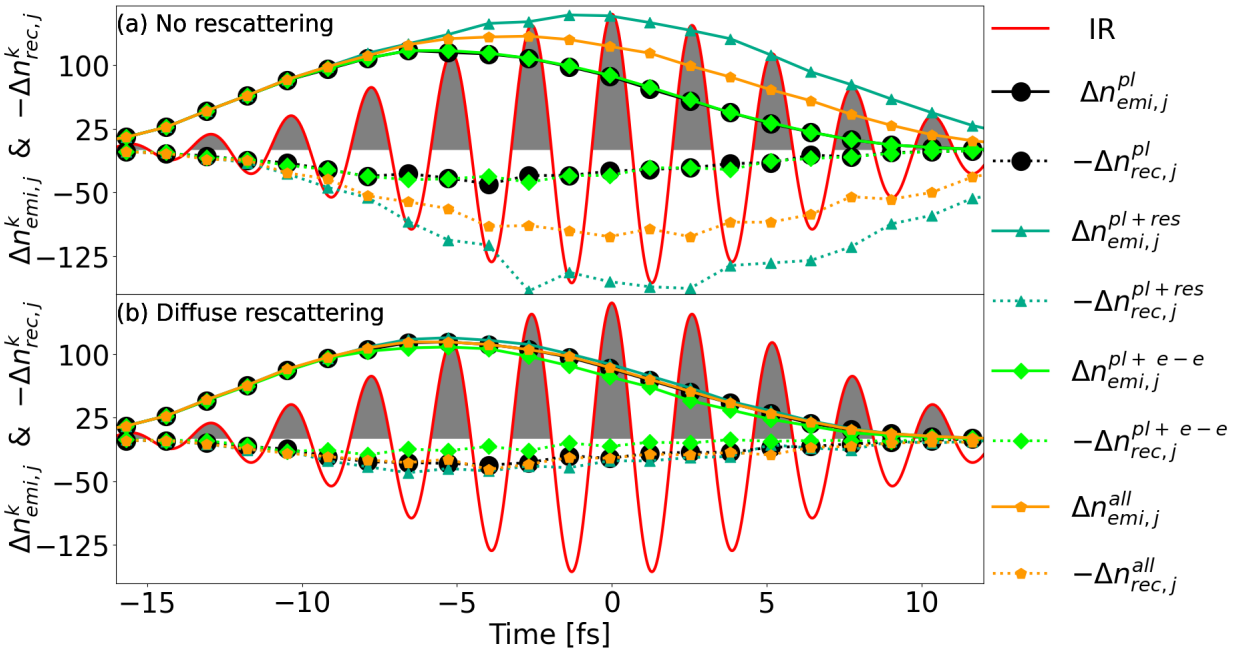

Figure 4.4: *Calculated numbers of emitted, $\Delta n^{\kappa}_{emi,j}$, and recombined, $\Delta n^{\kappa}_{rec,j}$, electrons in each laser half cycle j during the laser - NP interaction for* 30 *nm diameter gold nanospheres, corresponding to the VMI maps in the (a) first and (b) third row of Fig. 4.3. Subscripts refer to emitted and recombined electrons. Supercripts distinguish simulations including only the laser and induced plasmonic electric fields [$\kappa = pl$, corresponding to the VMI map in Figs. 4.3(a) and 4.3(i)] and to simulations adding either PE - residual-charge interactions [$\kappa = res$, cf., Figs. 4.3(b) and 4.3(j)] or PE Coulomb repulsion [$\kappa = e - e$, cf., Figs. 4.3(c) and 4.3(k)]. Numbers of recombined PEs are multiplied by (-1) for clarity. The calculated electron numbers are shown as colored markers that are connected by straight lines to guide the eye. The laser electric field is shown as the red solid line. The laser-pulse length, wavelength, and peak intensity are $\tau = 25$ fs, $\lambda = 780$ nm, and $I_0 = 8.0 \times 10^{12}$ W/cm^2, respectively.*

The PE dynamics is governed by alternating ($\vec{E}_{inc}$ and $\vec{E}_{pl}$), attractive ($\vec{F}_{res}$), and repulsive ($\vec{F}_{e-e}$) electric fields. The influence of the oscillating and repulsive forces on $n_{emi}(t)$, $n_{rec}(t)$, and $n_{pro}(t)$ is small, while the attractive interaction $\vec{F}_{res}$ has a significant impact on them. Residual-charge interactions $\vec{F}_{res}$ tend to increase the number of recombined PEs $n_{rec}(t)$. This increases the net electric field F on the surface by reducing the residual charge and thus increases $n_{emi}(t)$. As expected, this is most clearly displayed in simulations, in which

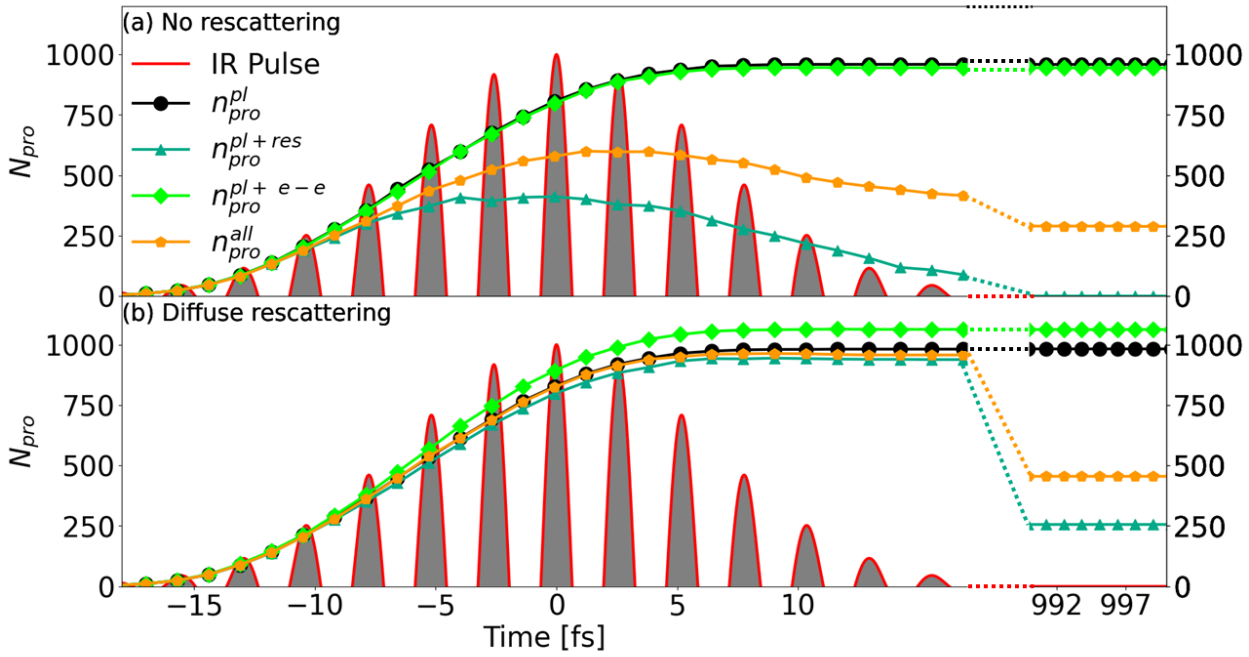

Figure 4.5: *As Fig. 4.4 for the time evolution of the accumulated number of propagated electrons, $n_{pro}(t) = n_{emi}(-20fs, t) - n_{rec}(-20fs, t)$. Final converged electron numbers are shown on the right side.*

otherwise rescattered PEs are assumed to recombine, shown in Figs. 4.4(a) and 4.5(a).

After the laser pulse has passed the NP (i.e., after $\approx \tau = 25$ fs) strong attractive residual-charge interactions prevents a fraction of low-energy PEs to escape the NP. These trapped electrons typically either repeatedly rescatter or orbit the NP. They do not contribute to the detected electron yield. Electrons on "trapped" trajectories screen the positive residual charges and are assumed to recombine. This assumption does not noticeably change the PE motion at large distances, where the PE interaction is dominated by the monopole term of the NP charge distribution. Due to the long-range residual-charge interactions, we carefully monitor the convergence of the trajectory calculations and propagate all PE trajectories for a sufficiently long time, to guarantee converged PEMDs. The right side of Fig. 4.5 shows the numbers of propagated PEs $n_{pro}(t)$ that have converged to the numbers of detected electrons after a propagation time of 1 ps.

4.3.3 Influence of the nanoparticle size and laser intensity

Figure 4.6 shows simulated and experimental PEMDs for gold nanospheres with diameters of with 5, 30, and 70 nm. The first and second rows compare simulated PEMDs to experimental VMI maps for laser peak intensities of $I_0 = 8.0 \times 10^{12}\ W/cm^2$. The third and fourth rows show the same information as the first and second rows but for higher peak intensity $1.5\, I_0$. The PEMDs in Figs. 4.6(a)- 4.6(l) are slightly elongated along the laser-polarization direction, with PE cutoff energies that increase with NP size. As discussed in Sec. 4.3.1 above, isotropic PEMDs are promoted by e-e interactions and diffuse PE rescattering from the surface, while incident laser and induced plasmonic-field interactions tend to imprint a dipolar shape. The simulated VMI maps also reveal the expected increase of the PE cutoff energy with the laser peak intensity. We quantify this laser intensity and NP-size-dependent effect in the following subsection.

4.3.4 Angle-integrated photoelectron yields and cutoff energies

Figure 4.7 shows simulated and experimental integrated yields as a function of the PE kinetic energy corresponding to the PEMDs in Figs. 4.6(a)-4.6(l). Due to the detector saturation at the center of the MCP phosphor detector, the experimental integrated yields for low energy PEs are not accurate. To be able to compare experimental integrated yields to one another and also to the simulated ones, we have removed the low energy part of the integrated yields from both experiment and simulated data.

Integration of the VMI-projected PEMDs $y(v_x, v_z)$ in Figs. 4.6(a)-4.6(l) over the PE detection angles ϕ in the VMI map plane results in the PE yields

$$Y(E_{PE}) = \int d\phi\; y(\sqrt{2E_{PE}}\cos\phi, \sqrt{2E_{PE}}\cos\phi) \tag{4.25}$$

as a function of the PE energy in the VMI map plane, $E_{PE} = (v_x^2 + v_z^2)/2$. The yields $Y(E_{PE})$ shown in Figs. 4.7(a)-4.7(f) are normalized individually to their maxima.

For the experimental PEMDs, the PE cutoff energies are taken from Jeffrey A. Powell's

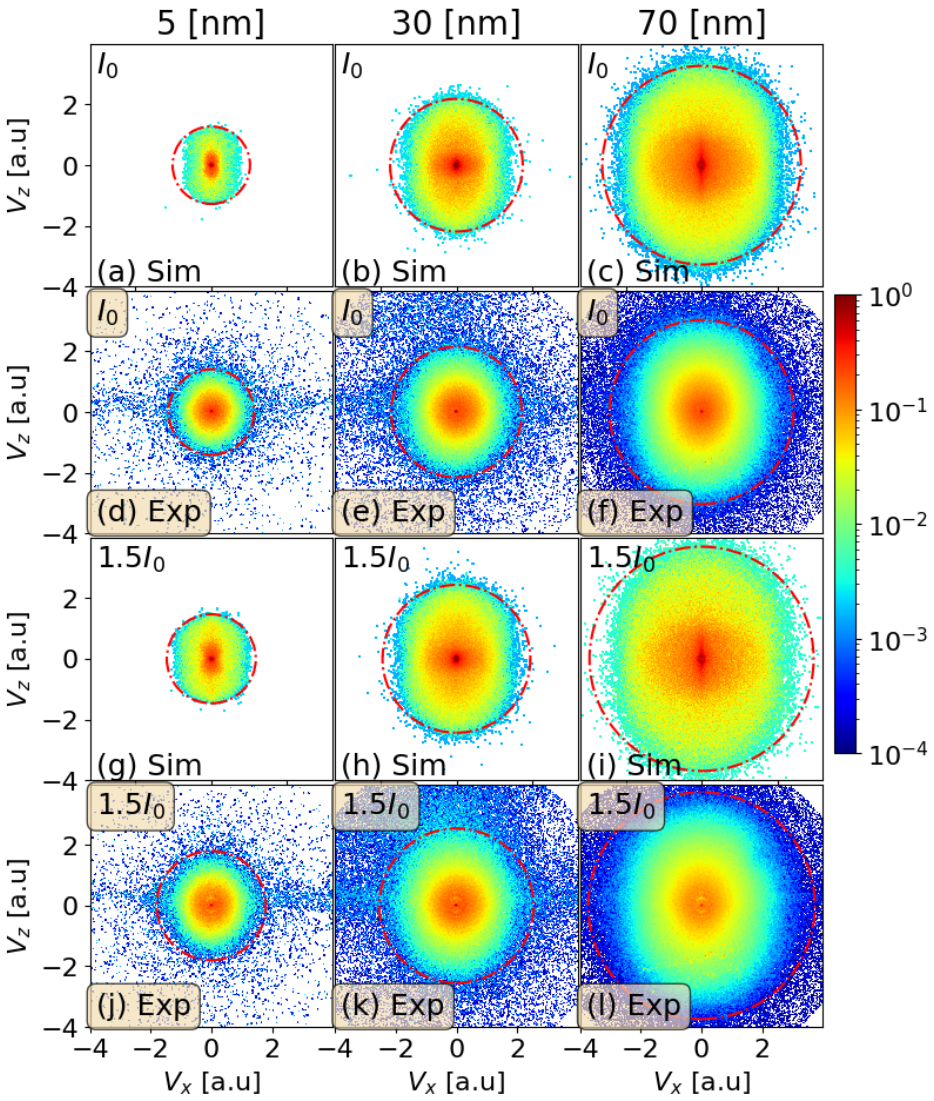

Figure 4.6: *Comparison of simulated (a-c), (g-i) and experimental (d-f), (j-l) VMI maps for gold nanospheres with* 5, 30, *and* 70 *nm diameter and laser peak intensities of (a-f)* $I_0 = 8.0 \times 10^{12}$ *W/cm*^{2} *and (g-l)* $1.5\, I_0$. *The laser-pulse length and wavelength are* 25 *fs and* 780 *nm. Red dashed circles in (a-l) indicate simulated and experimental PE cutoff energies.*

thesis [99]. For the simulated ones, we define the PE cutoff energy E_{cutoff} by integrating over the yield given by Eq. (4.25) as the PE energy up to which 99.5% of the total PE yield has accumulated,

$$\frac{\int_0^{E_{cutoff}} dE_{PE} Y(E_{PE})}{\int_0^{\infty} dE_{PE} Y(E_{PE})} = 99.5\%. \tag{4.26}$$

The PE cutoffs energies are shown as red dashed circles in Fig. 4.6. They increase with the NP size and slightly decrease with the selected peak laser intensities. The red-yellow circles and

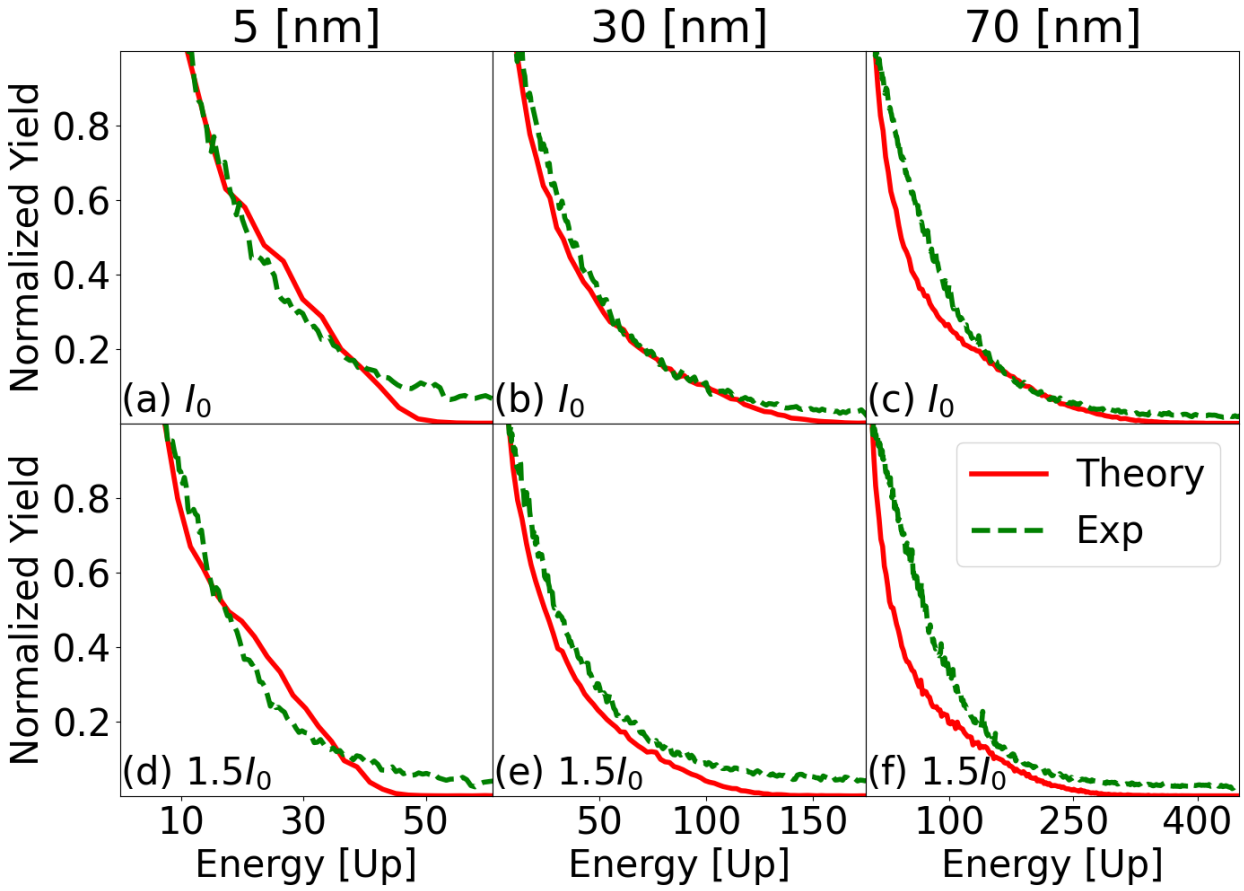

Figure 4.7: *Comparison of simulated and experimental (a-f) integrated PE yields as functions of the PE kinetic energy for gold nanospheres with* 5, 30, *and* 70 *nm diameter and laser peak intensities of (a-c)* $I_0 = 8.0 \times 10^{12}$ *W/cm*^{2} *and (d-f)* $1.5\,I_0$. *The laser-pulse length and wavelength are* 25 *fs and* 780 *nm.*

black-blue solid squares in Fig. 4.8 denote simulated cutoff energies for peak laser intensities of $I_0 = 8.0 \times 10^{12}$ W/cm^2 and $1.5I_0$, in units of the incident laser ponderomotive energies $U_p(I_0)$ and $U_p(1.5I_0)$, respectively. The intensity-dependent change of E_{cutoff} becomes more pronounced for larger NP diameters. To compare our simulation to experiment, we show the calculated and experimental cutoff energies in Fig. 4.9.

Based on the discussion of the different PE interactions and their influence on PEMDs in the preceding subsections, the increase of the PE yield and cutoff energy with NP size can be related to two independent causes. First, as the NP size increases, a larger surface becomes available from where more electrons are emitted. This suggests both a larger PE yield and due to the net increase of the Coulomb energy in the set of released electrons, an

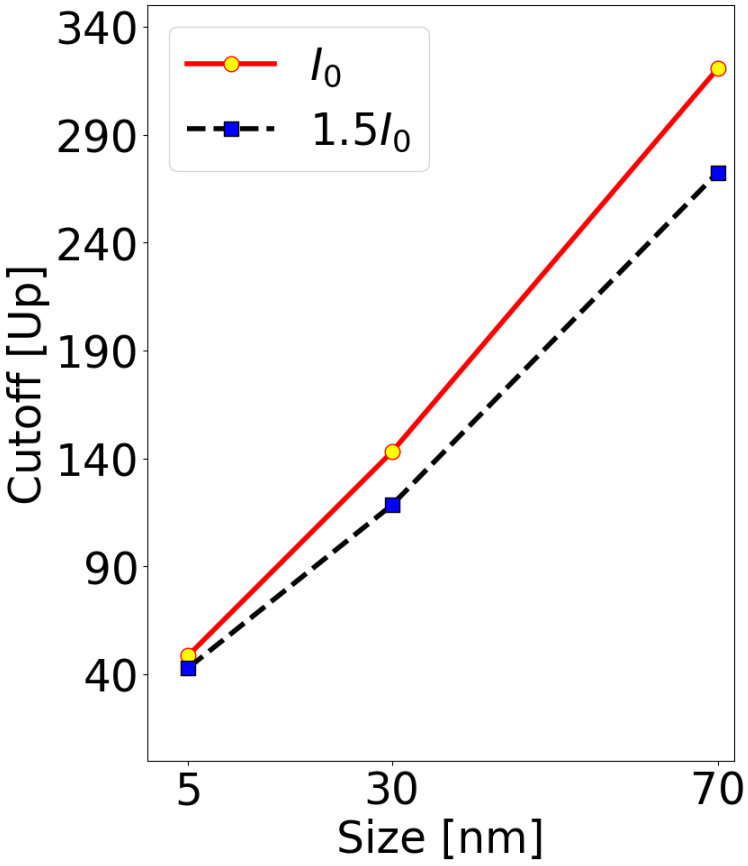

Figure 4.8: *Comparison of simulated PE cutoff energies scaled by incident-laser ponderomotive energy U_p for 5, 30, and 70 nm diameter gold nanospheres and laser peak intensities of $I_0 = 8.0 \times 10^{12}$ W/cm^2 and $1.5\,I_0$. The laser laser-pulse length and wavelength are the same as in Fig. 4.7.*

increase in E_{cutoff}. Second, due to the increase of the nanoplasmonic field enhancement with NP size (Fig. 2.3), the surface-potential barrier narrows for increasing NP size, promoting strong-field tunneling ionization. This tends to augment the measured PE yield, and, due to the larger PE-Coulomb-correlation energy, leads to a higher cutoff energy.

For gaseous atomic targets, the cutoff energy is proportional to the ponderomotive energy U_p [50–53]. In contrast, our results for metal NPs in Fig. (4.8) start to increasingly deviate from the linear scaling in U_p as the NP size increases. Although at the higher intensity, $1.5\,I_0$, the induced plasmonic field and PE Coulomb repulsion are stronger, our numerically calculated VMI maps indicate that the increasing accumulation of residual charges on the NP becomes the determining factor. This reduces the scaled cutoff energy at the larger

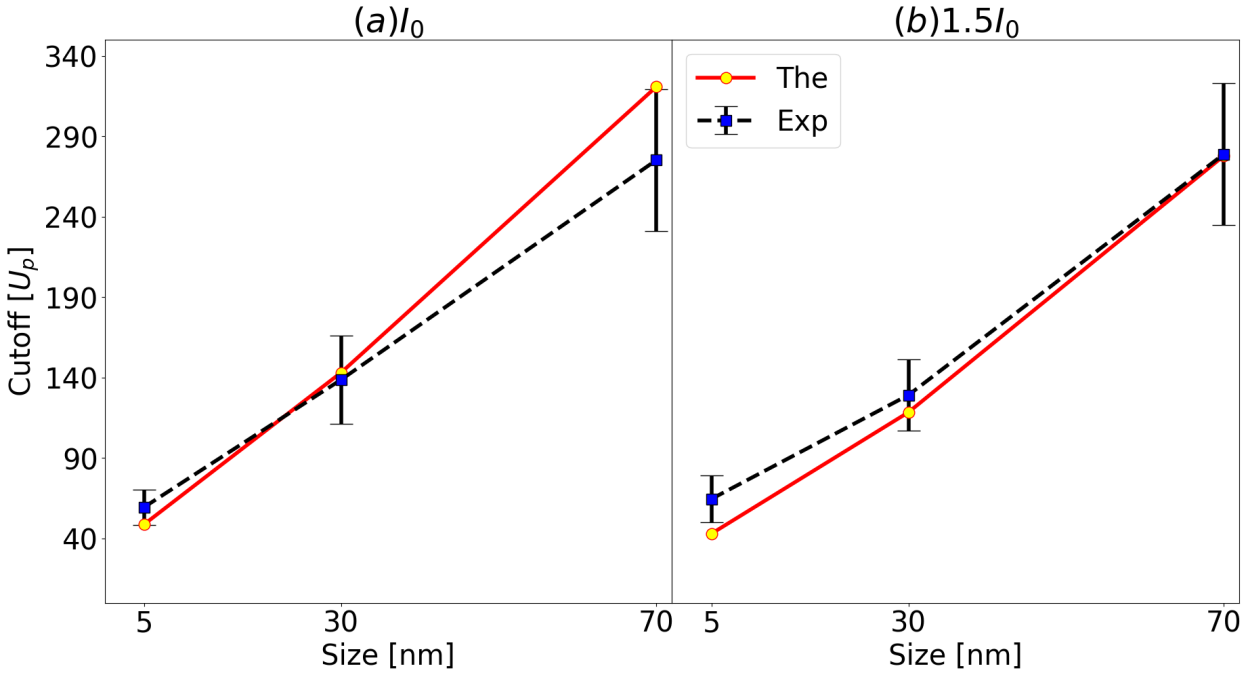

Figure 4.9: *Comparison of simulated and experimental PE cutoff energies scaled by incident-laser ponderomotive energy U_p for* 5, 30, *and* 70 *nm diameter gold nanospheres and laser peak intensities of $I_0 = 8.0 \times 10^{12}$ W/cm^2 and* $1.5\, I_0$. *The laser-pulse length and wavelength are the same as in Fig. 4.7.*

considered intensity. This reduction is more pronounced for larger NPs, due to stronger plasmonic field enhancement.

4.4 Summary and conclusions

We modeled strong-field ionization from metal NPs and numerically simulated PEMDs as experimentally accessible by VMI spectrometry. Our simulations scrutinize a complex dynamical interplay of PE emission, propagation, recombination, and rescattering. Augmented by strong plasmonic field enhancement, a large number of PEs tunnel ionize from metal NPs and result in high PE yields and cutoff energies. We analyzed the size and laser-intensity dependence of PE angular distributions in light of competing contributions from various PE interactions.

In particular, we found that the dipolar shape, imprinted on PEMDs by the incident laser and induced plasmonic fields, is mostly erased by e-e interactions and diffusive PE

rescattering at the NP surface to yield almost isotropical VMI maps. While for gaseous atomic targets directly emitted PEs acquire no more than about 20% of the cutoff energy for rescattered PEs [$10\,U_p(I_0)$], we have shown that direct photoemission from 30 nm metal NPs results in cutoff energies of $100\,U_p(I_0)$ and further increases for larger NPs, reaching about 75% of the cutoff energy for rescattered PEs. In addition, due to laser-intensity-dependent PE emission, the effects of residual charges and e-e interactions are highly intensity dependent. This leads to a nonlinear intensity dependence of the PE yield and cutoff energy scaling with $U_p(I_0)$, contrary to the known linear intensity scaling for gaseous atomic targets.

Chapter 5

Conclusion and outlook

In this chapter, we summarize the main results and conclusions of this dissertation and present a brief outlook and future works.

5.1 Attosecond streaking spectroscopy from plasmonic nanoparticles

We developed a classical model to study attosecond streaking spectroscopy from metallic nanospheres, extending a previous classical model by sampling over the entire conduction band and including transport and surface effects. Our numerical results show that these extensions noticeably impact streaking spectra. By varying the radius of the nanosphere, the wavelength of the streaking pulse, and adding or relaxing restrictions to emission from the Fermi level only and from the surface of the NP only, we scrutinized streaked photoemission spectra. In particular, we addressed (i) the influence of the NP's dielectric response on streaked photoemission and (ii) the fidelity with which streaked spectra allow the imaging of the temporal and spatial distribution of the NP's induced plasmonic near-field. The developed classical model is basic and versatile. It can be transferred to different geometries, such as surfaces, nanowires, nanotips, and metal and semiconductor nanostructures.

5.2 Imaging the plasmonic near-field from plasmonic nanoparticles

Based on the previously developed quantum-mechanical model, we propose a (with current technology) practicable spectroscopic scheme based on attosecond streaking spectroscopy which, by scanning the relative linear polarization directions of the XUV and streaking pulses, allows the imaging of plasmonic electric-field distributions on the surface of spherical NPs with nm spatial and sub-fs temporal resolution. The implementation of this method requires the extension of conventional streaking measurements from NPs by allowing for the controlled rotation of the relative linear polarization direction between the XUV and the IR pulses. The suggested imaging scheme has the potential to be generalized to non-spherical NPs by enabling the rotation of the electron detector or by adding multiple detectors at different directions. For full spatial resolution of the electric near-field distribution, the extension to non-spherical particles may require alignment of the NPs. Further improvements of the suggested imaging scheme may result in a powerful method for the scrutiny of nanoscopic plasmonically enhanced electric-field distributions and electronic dynamics on functional NPs and nanostructured surfaces.

5.3 Strong-field ionization of plasmonic nanoparticles

We modeled strong-field ionization of metal NPs by generalizing the three-step semi-classical model to simulate the PEMDs taken from the VMI spectrometer. Our experimental and numerical results show that the PE emission, propagation, recombination and rescattering processes are significantly more complex due to the bulk properties of NP, e-e interactions, plasmon excitation, trapped PEs, and residual charges. We account for and distinguish in PE momentum distributions the effects of e-e interactions, PE - residual-charge interactions, and transient laser-induced plasmonic fields. Our numerical results for 5, 30, and 70 nm diameter gold nanospheres and peak laser-pulse intensities of 8.0×10^{12} and 1.2×10^{12} W/cm^2 show how PE velocity-map-images are distinctly shaped by PE Coulomb repulsion, residual-charge

accumulations, and plasmonic near fields.

In particular, we found that the dipolar shape, imprinted on PEMDs by the incident laser and induced plasmonic fields, is mostly erased by e-e interactions and diffusive PE rescattering at the NP surface to yield almost isotropical VMI maps. While for gaseous atomic targets directly emitted PEs acquire no more than about 20% of the cutoff energy for rescattered PEs [$10\,U_p(I_0)$], we have shown that direct photoemission from 30 nm metal NPs results in cutoff energies of $100\,U_p(I_0)$ with further increases for larger NPs, reaching about 75% of the cutoff energy for rescattered PEs. In addition, due to laser-intensity-dependent PE emission, the effects of residual charges and e-e interactions are highly intensity dependent. This leads to a nonlinear intensity dependence of the PE yield and cutoff energy scaling with $U_p(I_0)$, contrary to the known linear intensity scaling for gaseous atomic targets.

This model can be applied to different geometries, such as surfaces, ellipsoids, nanowires, and nanotips. By using different tunneling ionization rate models, it can solve more complicated problems and be applied to different composites such as dielectric and semiconductor nanostructures.

Publications

1. J. Li, **E. Saydanzad**, and U. Thumm, *Retrieving plasmonic near-field information: A quantum-mechanical model for streaking photoelectron spectroscopy of gold nanospheres*, Phys. Rev. A **94**, 051401(R) (2016), URL: http://link.aps.org/doi/10.1103/PhysRevA.94.051401

2. J. Li, **E. Saydanzad**, and U. Thumm, *Attosecond time-resolved streaked photoelectron spectroscopy of transition-metal nanospheres*, Phys. Rev. A **95**, 043423 (2017), URL: https://link.aps.org/doi/10.1103/PhysRevA.95.043423

3. **E. Saydanzad**, J. Li, and U. Thumm, *Characterization of induced nanoplasmonic fields in time-resolved photoemission: A classical trajectory approach applied to gold nanospheres*, Phys. Rev. A **95**, 053406 (2017), URL: https://link.aps.org/doi/10.1103/PhysRevA.95.053406

4. **E. Saydanzad**, J. Li, and U. Thumm, *Spatiotemporal imaging of plasmonic fields near nanoparticles below the diffraction limit*, Phys. Rev. A **98**, 063422 (2018), URL: https://link.aps.org/doi/10.1103/PhysRevA.98.063422

5. J. Li, **E. Saydanzad**, and U. Thumm, *Imaging Plasmonic Fields with Atomic Spatiotemporal Resolution*, Phys. Rev. Lett. **120**, 223903 (2018), URL: https://link.aps.org/doi/10.1103/PhysRevLett.120.223903

6. J. A. Powell, J. Li, A. Summers, S. J. Robatjazi, M. Davino, P. Rupp, **E. Saydanzad**, C. M. Sorensen, D. Rolles, M. F. Kling, C. Trallero-Herrero, U. Thumm, A. Rudenko *Strong-field control of plasmonic properties in core-shell nanoparticles*, Submitted to Optica, URL: https://arxiv.org/abs/2108.06872

7. **E. Saydanzad**, J. Li and U. Thumm, *Strong-field ionization of plasmonic nanoparticles*, Submitted to Phys. Rev. A (2021)

8. **E. Saydanzad**, J. A. Powell, J. Li, S. J. Robatjazi, A. Summers, C. Trallero-Herrero, A. Rudenko, and U. Thumm, *Photoelectron momentum distributions and cutoff energies for strong-field ionization of plasmonic nanoparticles*, (In preparation)

Bibliography

[1] K. L. Kelly, E. Coronado, L. L. Zhao, and G. C. Schatz, *The optical properties of metal nanoparticles: the influence of size, shape, and dielectric environment*, J. Phys. Chem. B **107**, 668 (2003), URL https://doi.org/10.1021/jp026731y.

[2] L. Wang, M. Hasanzadeh Kafshgari, and M. Meunier, *Optical properties and applications of plasmonic-metal nanoparticles*, Adv. Funct. Mater. **30**, 2005400 (2020), URL https://onlinelibrary.wiley.com/doi/abs/10.1002/adfm.202005400.

[3] J. A. Powell, J. Li, A. Summers, S. J. Robatjazi, M. Davino, P. Rupp, E. Saydanzad, C. M. Sorensen, D. Rolles, M. F. Kling, et al., *Strong-field control of plasmonic properties in core-shell nanoparticles*, https://arxiv.org/abs/2108.06872 (2021), URL https://arxiv.org/abs/2108.06872.

[4] M. I. Stockman, M. F. Kling, U. Kleineberg, and F. Krausz, *Attosecond nanoplasmonic-field microscope*, Nat. Photonics **1**, 539 (2007), URL https://www.nature.com/articles/nphoton.2007.169.

[5] A. Kinkhabwala, Z. Yu, S. Fan, Y. Avlasevich, K. Müllen, and W. Moerner, *Large single-molecule fluorescence enhancements produced by a bowtie nanoantenna*, Nat. Photonics **3**, 654 (2009), URL https://www.nature.com/articles/nphoton.2009.187.

[6] S. L. Stebbings, F. Süßmann, Y. Y. Yang, A. Scrinzi, M. Durach, A. Rusina, M. I. Stockman, and M. F. Kling, *Generation of isolated attosecond extreme ultraviolet pulses employing nanoplasmonic field enhancement: optimization of coupled ellipsoids*, New J. Phys. **13**, 073010 (2011), URL https://iopscience.iop.org/article/10.1088/1367-2630/13/7/073010/meta.

[7] E. Skopalová, D. Lei, T. Witting, C. Arrell, F. Frank, Y. Sonnefraud, S. Maier, J. Tisch, and J. Marangos, *Numerical simulation of attosecond nanoplasmonic streaking*, New J. Phys. **13**, 083003 (2011), URL https://iopscience.iop.org/article/10.1088/1367-2630/13/8/083003/meta.

[8] M. Becker, W. C.-W. Huang, H. Batelaan, E. J. Smythe, and F. Capasso, *Measurement of the ultrafast temporal response of a plasmonic antenna*, Ann. Phys. (Berlin) **525**, L6 (2013), URL https://onlinelibrary.wiley.com/doi/full/10.1002/andp.201200206.

[9] P. Dombi, A. Horl, P. Racz, I. Marton, A. Trugler, J. R. Krenn, and U. Hohenester, *Ultrafast strong-field photoemission from plasmonic nanoparticles*, Nano Lett. **13**, 674 (2013), URL https://pubs.acs.org/doi/abs/10.1021/nl304365e.

[10] S. Zherebtsov, T. Fennel, J. Plenge, E. Antonsson, I. Znakovskaya, A. Wirth, O. Herrwerth, F. Süßmann, C. Peltz, I. Ahmad, et al., *Controlled near-field enhanced electron acceleration from dielectric nanospheres with intense few-cycle laser fields*, Nat. Phys. **7**, 656 (2011), URL https://www.nature.com/articles/nphys1983.

[11] J. Li, E. Saydanzad, and U. Thumm, *Retrieving plasmonic near-field information: A quantum-mechanical model for streaking photoelectron spectroscopy of gold nanospheres*, Phys. Rev. A **94**, 051401 (2016), URL https://journals.aps.org/pra/abstract/10.1103/PhysRevA.94.051401.

[12] M. I. Stockman, *Nanoplasmonics: The physics behind the applications*, Phys. Today **64**, 39 (2011), URL http://physics.gsu.edu/stockman/data/Stockman_Phys_Today_2011_Physics_behind_Applications.pdf.

[13] J. Li, E. Saydanzad, and U. Thumm, *Attosecond time-resolved streaked photoelectron spectroscopy of transition-metal nanospheres*, Phys. Rev. A **95**, 043423 (2017), URL https://journals.aps.org/pra/abstract/10.1103/PhysRevA.95.043423.

[14] S. Link and M. A. El-Sayed, *Size and temperature dependence of the plasmon absorption of colloidal gold nanoparticles*, J. Phys. Chem. B **103**, 4212 (1999), URL https://pubs.acs.org/doi/abs/10.1021/jp984796o.

[15] P. K. Jain, X. Huang, I. H. El-Sayed, and M. A. El-Sayed, *Review of some interesting surface plasmon resonance-enhanced properties of noble metal nanoparticles and their applications to biosystems*, Plasmonics **2**, 107 (2007), URL https://link.springer.com/article/10.1007/s11468-007-9031-1.

[16] E. Le Ru and P. Etchegoin, *Principles of Surface-Enhanced Raman Spectroscopy: And Related Plasmonic Effects* (Elsevier, Oxford, 2008).

[17] M. Müller, V. Kravtsov, A. Paarmann, M. B. Raschke, and R. Ernstorfer, *Nanofocused plasmon-driven sub-10 fs electron point source*, ACS Photonics **3**, 611 (2016), https://doi.org/10.1021/acsphotonics.5b00710, URL https://doi.org/10.1021/acsphotonics.5b00710.

[18] E. Saydanzad, J. Li, and U. Thumm, *Characterization of induced nanoplasmonic fields in time-resolved photoemission: a classical trajectory approach applied to gold nanospheres*, Phys. Rev. A **95**, 053406 (2017), URL https://journals.aps.org/pra/abstract/10.1103/PhysRevA.95.053406.

[19] A. Kabashin, P. Evans, S. Pastkovsky, W. Hendren, G. Wurtz, R. Atkinson, R. Pollard, V. Podolskiy, and A. Zayats, *Plasmonic nanorod metamaterials for biosensing*, Nat. Mater. **8**, 867 (2009), URL https://www.nature.com/articles/nmat2546.

[20] K. A. Willets and R. P. Van Duyne, *Localized surface plasmon resonance spectroscopy and sensing*, Annu. Rev. Phys. Chem. **58**, 267 (2007), URL https://www.annualreviews.org/doi/abs/10.1146/annurev.physchem.58.032806.104607.

[21] L. Wang, C. Darviot, J. Zapata-Farfan, S. Patskovsky, D. Trudel, and M. Meunier, *Designable nanoplasmonic biomarkers for direct microscopy cytopathology diagnostics*,

J. Biophotonics **12**, e201900166 (2019), URL https://onlinelibrary.wiley.com/doi/abs/10.1002/jbio.201900166.

[22] A. M. Wilson, J. Mazzaferri, E. Bergeron, S. Patskovsky, P. Marcoux-Valiquette, S. Costantino, P. Sapieha, and M. Meunier, *In vivo laser-mediated retinal ganglion cell optoporation using kv1. 1 conjugated gold nanoparticles*, Nano. Lett. **18**, 6981 (2018), URL https://doi.org/10.1021/acs.nanolett.8b02896.

[23] T. Chen and B. M. Reinhard, *Assembling color on the nanoscale: multichromatic switchable pixels from plasmonic atoms and molecules*, Adv. Mater. **28**, 3522 (2016), URL https://onlinelibrary.wiley.com/doi/abs/10.1002/adma.201506179.

[24] A. E. Schlather, A. Manjavacas, A. Lauchner, V. S. Marangoni, C. J. DeSantis, P. Nordlander, and N. J. Halas, *Hot hole photoelectrochemistry on au@ sio2@ au nanoparticles*, J. Phys. Chem. Lett. **8**, 2060 (2017), URL https://pubs.acs.org/doi/abs/10.1021/acs.jpclett.7b00563.

[25] M. T. Sheldon, J. Van de Groep, A. M. Brown, A. Polman, and H. A. Atwater, *Plasmoelectric potentials in metal nanostructures*, Science **346**, 828 (2014), URL https://www.science.org/doi/full/10.1126/science.1258405.

[26] S. Liu, R. Jiang, P. You, X. Zhu, J. Wang, and F. Yan, *Au/ag coreshell nanocuboids for high-efficiency organic solar cells with broadband plasmonic enhancement*, Energy Environ. Sci. **9**, 898 (2016), URL http://dx.doi.org/10.1039/C5EE03779D.

[27] A. M. Gobin, M. H. Lee, N. J. Halas, W. D. James, R. A. Drezek, and J. L. West, *Near-infrared resonant nanoshells for combined optical imaging and photothermal cancer therapy*, Nano Lett. **7**, 1929 (2007), URL https://pubs.acs.org/doi/abs/10.1021/nl070610y.

[28] C. Ayala-Orozco, C. Urban, M. W. Knight, A. S. Urban, O. Neumann, S. W. Bishnoi, S. Mukherjee, A. M. Goodman, H. Charron, T. Mitchell, et al., *Au nanomatryoshkas as efficient near-infrared photothermal transducers for cancer treatment: benchmarking*

against nanoshells, ACS Nano **8**, 6372 (2014), URL https://pubs.acs.org/doi/abs/10.1021/nn501871d.

[29] F. Krausz and M. I. Stockman, *Attosecond metrology: from electron capture to future signal processing*, Nat. Photonics **8**, 205 (2014), URL https://www.nature.com/articles/nphoton.2014.28.

[30] G. Baffou and R. Quidant, *Thermo-plasmonics: using metallic nanostructures as nano-sources of heat*, Laser Photonics Rev. **7**, 171 (2013), URL https://onlinelibrary.wiley.com/doi/abs/10.1002/lpor.201200003.

[31] E. Saydanzad, J. Li, and U. Thumm, *Spatiotemporal imaging of plasmonic fields near nanoparticles below the diffraction limit*, Phys. Rev. A **98**, 063422 (2018), URL https://link.aps.org/doi/10.1103/PhysRevA.98.063422.

[32] J. Li, E. Saydanzad, and U. Thumm, *Imaging plasmonic fields with atomic spatiotemporal resolution*, Phys. Rev. Lett. **120**, 223903 (2018), URL https://link.aps.org/doi/10.1103/PhysRevLett.120.223903.

[33] E. Goulielmakis, M. Uiberacker, R. Kienberger, A. Baltuska, V. Yakovlev, A. Scrinzi, T. Westerwalbesloh, U. Kleineberg, U. Heinzmann, M. Drescher, et al., *Direct measurement of light waves*, Science **305**, 1267 (2004), URL https://www.science.org/doi/full/10.1126/science.1100866.

[34] F. Krausz and M. Ivanov, *Attosecond physics*, Rev. Mod. Phys. **81**, 163 (2009), URL https://link.aps.org/doi/10.1103/RevModPhys.81.163.

[35] R. Kienberger, E. Goulielmakis, M. Uiberacker, A. Baltuska, V. Yakovlev, F. Bammer, A. Scrinzi, T. Westerwalbesloh, U. Kleineberg, U. Heinzmann, et al., *Atomic transient recorder*, Nature **427**, 817 (2004), URL https://www.nature.com/articles/nature02277.

[36] U. Thumm, Q. Liao, E. M. Bothschafter, F. Süßmann, M. F. Kling, and R. Kienberger, *Fundamentals of photonics and physics*, vol. 1 (Wiley, New York, 2015).

[37] S. R. Leone, C. W. McCurdy, J. Burgdörfer, L. S. Cederbaum, Z. Chang, N. Dudovich, J. Feist, C. H. Greene, M. Ivanov, R. Kienberger, et al., *What will it take to observe processes in real time?*, Nat. Photonics **8**, 162 (2014), URL https://www.nature.com/articles/nphoton.2014.48.

[38] E. Hutter and J. H. Fendler, *Exploitation of localized surface plasmon resonance*, Adv. Mater. **16**, 1685 (2004), URL https://onlinelibrary.wiley.com/doi/abs/10.1002/adma.200400271.

[39] F. Süßmann and M. F. Kling, *Attosecond nanoplasmonic streaking of localized fields near metal nanospheres*, Phys. Rev. B **84**, 121406 (2011), URL https://link.aps.org/doi/10.1103/PhysRevB.84.121406.

[40] B. Förg, J. Schötz, F. Süßmann, M. Foerster, M. Krueger, B. Ahn, W. Okell, K. Wintersperger, S. Zherebtsov, A. Guggenmos, et al., *Attosecond nanoscale near-field sampling*, Nat. Commun. **7**, 11717 (2016), URL https://www.nature.com/articles/ncomms11717.

[41] J. Schötz, B. Förg, M. Förster, W. A. Okell, M. I. Stockman, F. Krausz, P. Hommelhoff, and M. F. Kling, *Reconstruction of nanoscale near fields by attosecond streaking*, IEEE J. Sel. Top. Quantum Electron. **23**, 8700111 (2017), URL https://ieeexplore.ieee.org/abstract/document/7738457.

[42] C. Lemell, B. Solleder, K. Tőkési, and J. Burgdörfer, *Simulation of attosecond streaking of electrons emitted from a tungsten surface*, Phys. Rev. A **79**, 062901 (2009), URL https://journals.aps.org/pra/abstract/10.1103/PhysRevA.79.062901.

[43] Q. Liao and U. Thumm, *Attosecond time-resolved photoelectron dispersion and photoemission time delays*, Phys. Rev. Lett. **112**, 023602 (2014), URL https://journals.aps.org/prl/abstract/10.1103/PhysRevLett.112.023602.

[44] C.-H. Zhang and U. Thumm, *Effect of wave-function localization on the time de-*

lay in photoemission from surfaces, Phys. Rev. A **84**, 065403 (2011), URL https://journals.aps.org/pra/abstract/10.1103/PhysRevA.84.065403.

[45] F. Kelkensberg, A. Koenderink, and M. Vrakking, *Attosecond streaking in a nanoplasmonic field*, New J. Phys. **14**, 093034 (2012), URL https://iopscience.iop.org/article/10.1088/1367-2630/14/9/093034/meta.

[46] A. G. Borisov, P. M. Echenique, and A. Kazansky, *Attostreaking with metallic nano-objects*, New J. Phys. **14**, 023036 (2012), URL https://iopscience.iop.org/article/10.1088/1367-2630/14/2/023036/meta.

[47] J. S. Prell, L. J. Borja, D. M. Neumark, and S. R. Leone, *Simulation of attosecond-resolved imaging of the plasmon electric field in metallic nanoparticles*, Ann. Phys. (Berlin) **525**, 151 (2013), URL https://onlinelibrary.wiley.com/doi/full/10.1002/andp.201200201.

[48] L. Keldysh, *Ionization in the field of a strong electromagnetic wave*, Sov. Phys. JETP **20**, 1307 (1965).

[49] L. Gallmann, I. Jordan, H. J. Wrner, L. Castiglioni, M. Hengsberger, J. Osterwalder, C. A. Arrell, M. Chergui, E. Liberatore, U. Rothlisberger, et al., *Photoemission and photoionization time delays and rates*, Struct. Dyn **4**, 061502 (2017), URL https://doi.org/10.1063/1.4997175.

[50] G. G. Paulus, W. Becker, W. Nicklich, and H. Walther, *Rescattering effects in above-threshold ionization: a classical model*, J. Phys. B: At., Mol. Opt. Phys. **27**, L703 (1994), URL https://doi.org/10.1088/0953-4075/27/21/003.

[51] B. Walker, B. Sheehy, K. C. Kulander, and L. F. DiMauro, *Elastic rescattering in the strong field tunneling limit*, Phys. Rev. Lett. **77**, 5031 (1996), URL https://link.aps.org/doi/10.1103/PhysRevLett.77.5031.

[52] W. Becker, F. Grasbon, R. Kopold, D. Milošević, G. Paulus, and H. Walther, *Above-threshold ionization: From classical features to quantum effects*, Adv. At. Mol. Opt.

Phys. **48**, 35 (2002), URL https://www.sciencedirect.com/science/article/pii/S1049250X02800064.

[53] W. Becker, S. P. Goreslavski, D. B. Milošević, and G. G. Paulus, *The plateau in above-threshold ionization: the keystone of rescattering physics*, J PHYS B-AT MOL OPT **51**, 162002 (2018), URL https://doi.org/10.1088/1361-6455/aad150.

[54] S. Ghimire, A. D. DiChiara, E. Sistrunk, P. Agostini, L. F. DiMauro, and D. A. Reis, *Observation of high-order harmonic generation in a bulk crystal*, Nat. Phys. **7**, 138 (2011), URL https://www.nature.com/articles/nphys1847.

[55] M. J. Ambrosio and U. Thumm, *Energy-resolved attosecond interferometric photoemission from ag(111) and au(111) surfaces*, Phys. Rev. A **97**, 043431 (2018), URL https://link.aps.org/doi/10.1103/PhysRevA.97.043431.

[56] M. J. Ambrosio and U. Thumm, *Spatiotemporal analysis of a final-state shape resonance in interferometric photoemission from cu(111) surfaces*, Phys. Rev. A **100**, 043412 (2019), URL https://link.aps.org/doi/10.1103/PhysRevA.100.043412.

[57] F. Navarrete and U. Thumm, *Two-color-driven enhanced high-order harmonic generation in solids*, Phys. Rev. A **102**, 063123 (2020), URL https://link.aps.org/doi/10.1103/PhysRevA.102.063123.

[58] V. E. Nefedova, S. Frhlich, F. Navarrete, N. Tancogne-Dejean, D. Franz, A. Hamdou, S. Kaassamani, D. Gauthier, R. Nicolas, G. Jargot, et al., *Enhanced extreme ultraviolet high-harmonic generation from chromium-doped magnesium oxide*, Appl. Phys. Lett. **118**, 201103 (2021), URL https://doi.org/10.1063/5.0047421.

[59] L. Xue, S. Liu, Y. Hang, A. M. Summers, D. J. Wilson, X. Wang, P. Chen, T. G. Folland, J. A. Hachtel, H. Shi, et al., *Unraveling ultrafast photoionization in hexagonal boron nitride*, arXiv preprint arXiv:2101.10429 (2021), URL https://arxiv.org/abs/2101.10429.

[60] F. Navarrete, M. F. Ciappina, and U. Thumm, *Crystal-momentum-resolved contributions to high-order harmonic generation in solids*, Phys. Rev. A **100**, 033405 (2019), URL https://link.aps.org/doi/10.1103/PhysRevA.100.033405.

[61] T. Ditmire, J. Zweiback, V. Yanovsky, T. Cowan, G. Hays, and K. Wharton, *Nuclear fusion from explosions of femtosecond laser-heated deuterium clusters*, Nature **398**, 489 (1999), URL https://www.nature.com/articles/19037.

[62] J. Passig, R. Irsig, N. X. Truong, T. Fennel, J. Tiggesbäumker, and K. H. Meiwes-Broer, *Nanoplasmonic electron acceleration in silver clusters studied by angular-resolved electron spectroscopy*, New J. Phys. **14**, 085020 (2012), URL https://doi.org/10.1088/1367-2630/14/8/085020.

[63] C. Varin, C. Peltz, T. Brabec, and T. Fennel, *Light wave driven electron dynamics in clusters*, Ann. Phys. (Berlin) **526**, 135 (2014), URL https://onlinelibrary.wiley.com/doi/full/10.1002/andp.201490001.

[64] T. Lünskens, P. Heister, M. Thämer, C. A. Walenta, A. Kartouzian, and U. Heiz, *Plasmons in supported size-selected silver nanoclusters*, Phys. Chem. Chem. Phys **17**, 17541 (2015), URL http://dx.doi.org/10.1039/C5CP01582K.

[65] Z. Wang, A. Camacho Garibay, H. Park, U. Saalmann, P. Agostini, J. M. Rost, and L. F. DiMauro, *Universal high-energy photoelectron emission from nanoclusters beyond the atomic limit*, Phys. Rev. Lett. **124**, 173201 (2020), URL https://link.aps.org/doi/10.1103/PhysRevLett.124.173201.

[66] G. Herink, D. R. Solli, M. Gulde, and C. Ropers, *Field-driven photoemission from nanostructures quenches the quiver motion*, Nature **483**, 190 (2012), URL https://www.nature.com/articles/nature10878.

[67] M. Krüger, M. Schenk, and P. Hommelhoff, *Attosecond control of electrons emitted from a nanoscale metal tip*, Nature **475**, 78 (2011), URL https://www.nature.com/articles/nature10196.

[68] L. Seiffert, Q. Liu, S. Zherebtsov, A. Trabattoni, P. Rupp, M. Castrovilli, M. Galli, F. Süßmann, K. Wintersperger, J. Stierle, et al., *Attosecond chronoscopy of electron scattering in dielectric nanoparticles*, Nat. Phys. **13**, 766 (2017), URL https://www.nature.com/articles/nphys4129.

[69] P. B. Corkum, *Plasma perspective on strong field multiphoton ionization*, Phys. Rev. Lett. **71**, 1994 (1993), URL https://link.aps.org/doi/10.1103/PhysRevLett.71.1994.

[70] G. Mie, *Beiträge zur optik trüber medien, speziell kolloidaler metallösungen*, Ann. Phys. (Berlin) **330**, 377 (1908), URL https://onlinelibrary.wiley.com/doi/abs/10.1002/andp.19083300302.

[71] J. A. Stratton, *Electromagnetic theory* (John Wiley & Sons, 2007).

[72] F. Süßmann, L. Seiffert, S. Zherebtsov, V. Mondes, J. Stierle, M. Arbeiter, J. Plenge, P. Rupp, C. Peltz, A. Kessel, et al., *Field propagation-induced directionality of carrier-envelope phase-controlled photoemission from nanospheres*, Nat. Commun. **6**, 7944 (2015), URL https://www.nature.com/articles/ncomms8944.

[73] Q. Liu, L. Seiffert, F. Sümann, S. Zherebtsov, J. Passig, A. Kessel, S. A. Trushin, N. G. Kling, I. Ben-Itzhak, V. Mondes, et al., *Ionization-induced subcycle metallization of nanoparticles in few-cycle pulses*, ACS Photonics **7**, 3207 (2020), URL https://doi.org/10.1021/acsphotonics.0c01282.

[74] M. V. Ammosov, *Tunnel ionization of complex atoms and of atomic ions in an altemating electromagnetic field*, Sov. Phys. JETP **64**, 1191 (1987).

[75] J. A. Powell, A. M. Summers, Q. Liu, S. J. Robatjazi, P. Rupp, J. Stierle, C. Trallero-Herrero, M. F. Kling, and A. Rudenko, *Interplay of pulse duration, peak intensity, and particle size in laser-driven electron emission from silica nanospheres*, Opt. Express **27**, 27124 (2019), URL http://www.opticsexpress.org/abstract.cfm?URI=oe-27-19-27124.

[76] E. Merzbacher, *Quantum mechanics* (Wiley, New York, 1998).

[77] N. Ashcroft and N. Mermin, *Solid state physics* (Saunders College, Philadelphia, 1976).

[78] W. M. Haynes, *CRC handbook of chemistry and physics* (CRC press, Boca Raton, 2014).

[79] J. D. Jackson, *Classical electrodynamics, 3rd ed.* (Wiley, New York, 1999).

[80] S. W. Verbruggen, M. Keulemans, J. A. Martens, and S. Lenaerts, *Predicting the surface plasmon resonance wavelength of goldsilver alloy nanoparticles*, J. Phys. Chem. C **117**, 19142 (2013), URL https://doi.org/10.1021/jp4070856.

[81] H. Kuwata, H. Tamaru, K. Esumi, and K. Miyano, *Resonant light scattering from metal nanoparticles: Practical analysis beyond rayleigh approximation*, Appl. Phys. Lett. **83**, 4625 (2003), URL https://aip.scitation.org/doi/abs/10.1063/1.1630351.

[82] P. G. Etchegoin, E. Le Ru, and M. Meyer, *An analytic model for the optical properties of gold*, J. Chem. Phys. **125**, 164705 (2006), URL https://aip.scitation.org/doi/full/10.1063/1.2360270.

[83] A. Vial, T. Laroche, M. Dridi, and L. Le Cunff, *A new model of dispersion for metals leading to a more accurate modeling of plasmonic structures using the fdtd method*, Appl. Phys. A **103**, 849 (2011), URL https://link.springer.com/article/10.1007/s00339-010-6224-9.

[84] S. A. Maier, *Plasmonics: fundamentals and applications* (Springer, New York, 2007).

[85] P. B. Johnson and R.-W. Christy, *Optical constants of the noble metals*, Phys. Rev. B **6**, 4370 (1972), URL https://journals.aps.org/prb/abstract/10.1103/PhysRevB.6.4370.

[86] S. Tanuma, C. Powell, and D. Penn, *Calculations of electron inelastic mean free paths. ix. data for 41 elemental solids over the 50 ev to 30 kev range*, Surface

and Interface Analysis **43**, 689 (2011), URL https://analyticalsciencejournals.onlinelibrary.wiley.com/doi/full/10.1002/sia.3522.

[87] M. H. Kalos and P. A. Whitlock, *Monte-Carlo methods* (John Wiley & Sons, Weinheim, 2008).

[88] C. Kittel, *Introduction to solid state physics* (Wiley, Hoboken, 2004), ISBN 9780471415268.

[89] Q. Liao and U. Thumm, *Initial-state, mean-free-path, and skin-depth dependence of attosecond time-resolved ir-streaked xuv photoemission from single-crystalline magnesium*, Phys. Rev. A **89**, 033849 (2014), URL https://journals.aps.org/pra/abstract/10.1103/PhysRevA.89.033849.

[90] S. Neppl, R. Ernstorfer, A. Cavalieri, C. Lemell, G. Wachter, E. Magerl, E. Bothschafter, M. Jobst, M. Hofstetter, U. Kleineberg, et al., *Direct observation of electron propagation and dielectric screening on the atomic length scale*, Nature **517**, 342 (2015), URL https://www.nature.com/articles/nature14094.

[91] W. Okell, T. Witting, D. Fabris, C. Arrell, J. Hengster, S. Ibrahimkutty, A. Seiler, M. Barthelmess, S. Stankov, D. Lei, et al., *Temporal broadening of attosecond photoelectron wavepackets from solid surfaces*, Optica **2**, 383 (2015), URL https://www.osapublishing.org/optica/fulltext.cfm?uri=optica-2-4-383&id=315348.

[92] C. Rewitz, T. Keitzl, P. Tuchscherer, J.-S. Huang, P. Geisler, G. Razinskas, B. Hecht, and T. Brixner, *Ultrafast plasmon propagation in nanowires characterized by far-field spectral interferometry*, Nano Lett. **12**, 45 (2011), URL https://pubs.acs.org/doi/abs/10.1021/nl202864n.

[93] M. Schultze, K. Ramasesha, C. Pemmaraju, S. Sato, D. Whitmore, A. Gandman, J. S. Prell, L. Borja, D. Prendergast, K. Yabana, et al., *Attosecond band-gap dynamics in silicon*, Science **346**, 1348 (2014), URL https://www.science.org/doi/full/10.1126/science.1260311.

[94] J. L. Ellis, D. D. Hickstein, W. Xiong, F. Dollar, B. B. Palm, K. E. Keister, K. M. Dorney, C. Ding, T. Fan, M. B. Wilker, et al., *Materials properties and solvated electron dynamics of isolated nanoparticles and nanodroplets probed with ultrafast extreme ultraviolet beams*, J. Phys. Chem. Lett. **7**, 609 (2016), URL https://pubs.acs.org/doi/abs/10.1021/acs.jpclett.5b02772.

[95] A. M. Summers, A. S. Ramm, G. Paneru, M. F. Kling, B. N. Flanders, and C. A. Trallero-Herrero, *Optical damage threshold of au nanowires in strong femtosecond laser fields*, Opt. Express **22**, 4235 (2014), URL http://www.osapublishing.org/oe/abstract.cfm?URI=oe-22-4-4235.

[96] R. H. Fowler and L. Nordheim, *Electron emission in intense electric fields*, Proceedings of the Royal Society of London. Series A, Containing Papers of a Mathematical and Physical Character **119**, 173 (1928), URL https://royalsocietypublishing.org/doi/abs/10.1098/rspa.1928.0091.

[97] J. H. B. Deane and R. G. Forbes, *The formal derivation of an exact series expansion for the principal schottky–nordheim barrier functionv, using the gauss hypergeometric differential equation*, J. Phys. A Math **41**, 395301 (2008), URL https://doi.org/10.1088/1751-8113/41/39/395301.

[98] S. Anisimov, B. Kapeliovich, and T. Perelman, *Electron emission from metal surfaces exposed to ultrashort laser pulses*, Zh. Eksp. Teor. Fiz **66**, 375 (1974), URL http://www.jetp.ras.ru/cgi-bin/dn/e_039_02_0375.pdf.

[99] J. A. Powell, Ph.D. thesis, Kansas State University (2017), URL https://krex.k-state.edu/dspace/handle/2097/38262.

[100] C. S. Kumarasinghe, M. Premaratne, Q. Bao, and G. P. Agrawal, *Theoretical analysis of hot electron dynamics in nanorods*, Sci. Rep. **5**, 12140 (2015), URL https://www.nature.com/articles/srep12140.

[101] P. Narang, R. Sundararaman, and H. A. Atwater, *Plasmonic hot carrier dynamics in solid-state and chemical systems for energy conversion*, Nanophotonics **5**, 96 (2016), URL https://doi.org/10.1515/nanoph-2016-0007.

[102] E. L. Murphy and R. Good Jr, *Thermionic emission, field emission, and the transition region*, Phys. Rev. **102**, 1464 (1956), URL https://journals.aps.org/pr/abstract/10.1103/PhysRev.102.1464.

[103] R. G. Forbes, *Simple good approximations for the special elliptic functions in standard fowler-nordheim tunneling theory for a schottky-nordheim barrier*, Appl. Phys. Lett. **89**, 113122 (2006), URL https://aip.scitation.org/doi/full/10.1063/1.2354582.

[104] S. C. Singh, H. Zeng, C. Guo, and W. Cai, *Nanomaterials: processing and characterization with lasers* (John Wiley & Sons, 2012).

[105] L. L. Dasallas and W. O. Garcia, *Numerical simulation of femtosecond pulsed laser ablation of copper for oblique angle of incidence through two-temperature model*, Mater. Res. Express **5**, 016518 (2018), URL https://doi.org/10.1088/2053-1591/aaa4e8.

[106] C. F. Bohren and D. R. Huffman, *Absorption and scattering of light by small particles* (John Wiley & Sons, 2008).

[107] C. Voisin, N. Del Fatti, D. Christofilos, and F. Valle, *Ultrafast electron dynamics and optical nonlinearities in metal nanoparticles*, J. Phys. Chem. B **105**, 2264 (2001), URL https://doi.org/10.1021/jp0038153.